POLITECNICO DI TORINO

MASTER'S DEGREE THESIS IN NANOTECHNOLOGIES FOR ICTS

Mimicking visual memory in stimuli-responsive material

Candidate: Gabriele Carbone

Supervisors: Prof. Francesca Frascella
Dott. Angelo Angelini

Academic Year 2024/25

Abstract

Recent advances in materials science and unconventional computing have enhanced a growing interest in the development of "intelligent matter", materials that integrate sensing, memory, and adaptive response within their physical structure.
These systems aim to implement computational functions directly at the matter level, enabling distributed, low-power information processing without relying on external control or digital architectures.
Within this emerging paradigm, light-responsive materials, especially azobenzene-based polymers, have shown great promise due to their intrinsic light-triggered molecular dynamics.

This thesis investigates the azopolymer PAZO as a candidate for implementing elementary visual functionalities directly in matter.
Through optical stimulation, PAZO films exhibit light-induced birefringence with tunable dynamics, governed by molecular reorientation and relaxation processes.
Exploiting this behavior, two biologically inspired tasks are explored: luminance adaptation and color recognition.

First, the influence of film thickness on birefringence response is studied to emulate photopic and scotopic adaptation mechanisms, analogous to cone and rod cell dynamics.
Results show that thickness strongly modulates the amplitude and temporal persistence of the birefringent response, offering a physical basis for light-level adaptation.

Second, the material's relaxation dynamics are studied under stimulation with distinct wavelengths to evaluate its spectral sensitivity.
A temporal signature associated with each wavelength suggests the potential for color discrimination based purely on birefringence decay profiles.

These results set PAZO as a compelling platform for light-driven adaptive behavior, offering a combination of structural tunability, analog and reconfigurable optical responses, and localized spatial addressability enabled by microstructuring techniques.

Contents

List of Figures

List of Tables

1 | Introduction

1.1 Intelligent Matter concept

The 21st century is marked by an unprecedented acceleration in the development of artificial intelligence (AI), a field profoundly inspired by the computational power and energy efficiency of the human brain.
Traditional computing, built upon the von Neumann architecture, has been the bedrock of the digital revolution.
However, it faces a fundamental limitation: the physical separation of memory and processing units.
The constant shuffling of data between these components creates a bottleneck that not only limits computational speed but also consumes substantial power, a challenge that becomes ever more acute in computationally intensive AI applications.
This has spurred a paradigm shift in scientific thinking, moving away from centralized processing towards decentralized, brain-inspired computational models[1].

This shift gives rise to a revolutionary concept: intelligent matter.
The term describes a new class of synthetic material that transcends its traditionally passive role, becoming an active participant in computation.
Intelligence, in this context, is understood as the ability to perceive information from the external world, retain that information as knowledge, and apply it to enact adaptive behaviors within a dynamic environment[2].
While so far found almost exclusively in living organisms, intense research efforts are aimed at building synthetic systems with these very skills of learning and adaptation.
The ultimate vision is to create a continuous "computing tissue", where information processing is not confined to a central unit but is distributed throughout the structure of the material itself.

To realize such a material, a hierarchical approach to complexity is required, integrating

---

[1] Dennis V Christensen et al. , **2**: 022501, 2022.

[2] C. Kaspar et al. , **594**: 345–355, 2021.

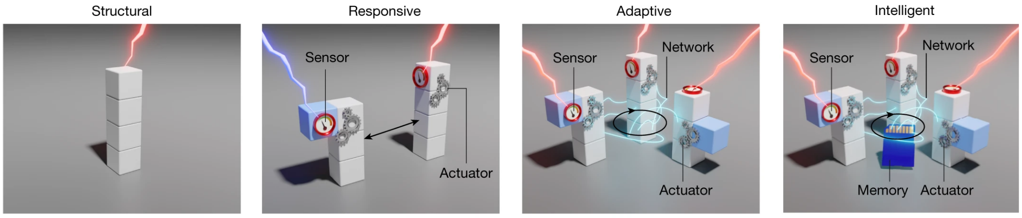

Figure 1.1: Illustration of the four key functional elements of intelligent matter (From [2])

four key functional elements that work together:

- **Sensors**: These are the material's interface with the world, responsible for receiving external inputs (like light, heat, or force) and feedback signals. This sensing process is typically an energy transformation, converting the input signal into a form that the material can process internally, such as converting light absorbance into a change in molecular structure.

- **Actuators**: In response to a stimulus detected by the sensors, actuators provide an output to the environment by modifying the material's intrinsic properties, such as its shape, color, or conductivity.

- **A Communication Network**: To enable complex, adaptive behavior, the material requires internal pathways for communication. This network interconnects the sensors, actuators, and memory, allowing for the crucial processing of feedback that distinguishes merely responsive materials from truly adaptive ones.

- **Memory**: The capacity to learn depends on the ability to store information. An inherent memory capability is necessary to retain received information over the long term, which can then be recalled as knowledge to inform future actions and decisions.

By systematically combining these elements, matter can be classified into advancing levels of functionality: from structural matter, which is static after synthesis, to responsive matter, which can change its properties in response to a stimulus, to adaptive matter, which incorporates a feedback network to regulate its response, and finally, to intelligent matter, which integrates all four elements to achieve learning.
Inspiration for this endeavor comes directly from nature, where sophisticated macroscopic functions emerge from the elegant bottom-up assembly of molecular and nanoscale building blocks.
This thesis follows this nature-inspired path, exploring a light-responsive organic material as a step toward the realization of intelligent matter with embedded, brain-like functionalities.

1.2 Neuromorphic Photonics

As we seek to build intelligent systems, light has emerged as a particularly attractive medium for information processing. Neuromorphic photonics, a field dedicated to creating optical systems that emulate the brain's computational efficiency, exploits the intrinsic advantages of light as an information carrier: unparalleled speed, vast bandwidth, and the potential for highly parallel processing [1,3]. In recent years, researchers have explored various material platforms to build these brain-inspired optical devices.

One prominent platform is optical phase-change materials (**PCMs**). These materials offer excellent stability, can store information in non-volatile states, and are compatible with existing CMOS fabrication technology, making them suitable for creating integrated photonic circuits with memory capabilities [4]. However, their key strength (i.e. non-volatility), is also a limitation. Many brain-like computational tasks, especially those involving the processing of temporal sequences, require a volatile or "fading" memory, a characteristic not intrinsically present in PCMs [5]. Furthermore, PCMs often require high-energy inputs to induce phase transitions, which poses significant operational challenges for energy-efficient computing [6].

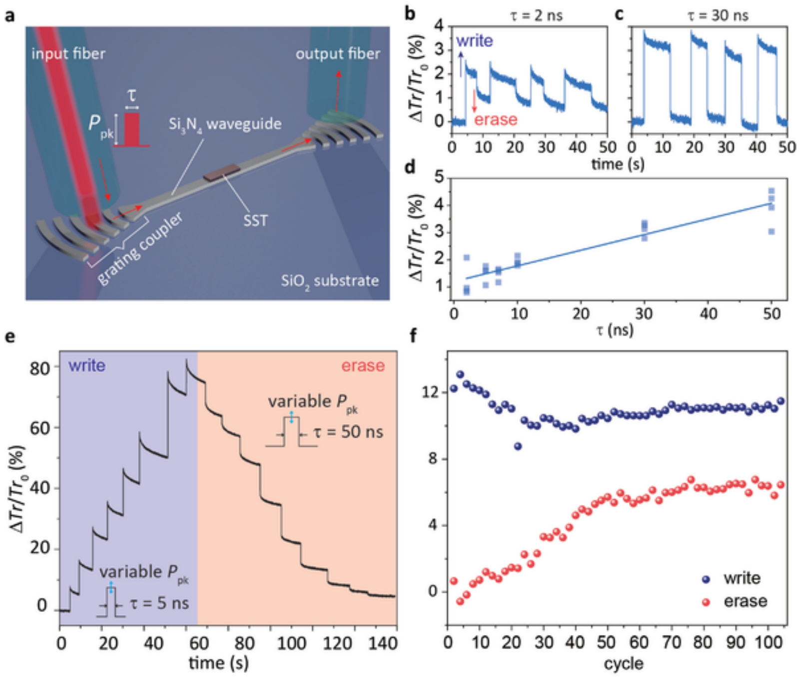

Figure 1.2: Non-volatile photonic memory based on an SST thin film (From [4])

Another advanced approach utilizes Van der Waals (**VdW**) heterostructures, which are

---

[3] Bhavin J. Shastri et al. , **15**: 102–114, 2021.
[4] Xiaozhang Chen et al. , **35**: , 2022.
[5] M. Wuttig, H. Bhaskaran, and T. Taubner. , **11**: 465–476, 2017.
[6] Rui Chen et al. , **9**: 3181–3195, 2022.

created by stacking atomically thin, two-dimensional materials.
These novel structures have been successfully used to create "in-sensor computing" devices, where sensing and processing occur in the same location, mimicking the efficiency of biological sensory systems [7].

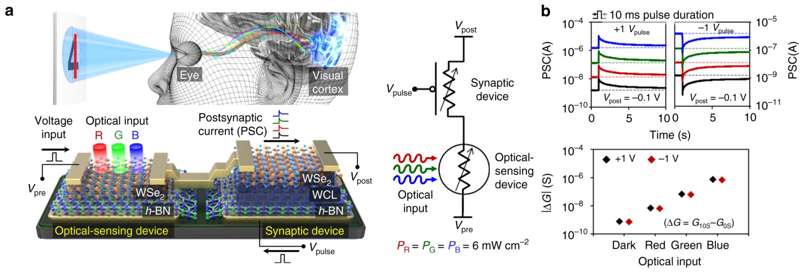

Figure 1.3: Van der Waals heterostructure (h-BN/WSe_2) optic-neural synaptic device (From [7])

VdW systems can exhibit both volatile short-term effects and non-volatile long-term effects, making them highly suitable for emulating the synaptic plasticity found in the brain[8]. Despite their promise, these materials are currently hampered by significant challenges related to material stability, reproducibility, and high sensitivity to defects, which hinder their path toward practical, large-scale applications[8].

In this landscape, light-responsive organic materials, and azopolymers in particular, present a compelling and highly versatile alternative.
Their key advantage lies in a unique dual capability: they can function as both a seamless, continuous medium and a highly engineerable structured platform, allowing for a variety of applications that are difficult to achieve with other systems.

When used as a continuous, uniform film, an azopolymer offers an ideal substrate for processing spatiotemporal information: unlike systems constructed from arrays of discrete, top-down fabricated optoelectronic devices, a continuous film has no inherent "dead space" between pixels, making it perfectly suited for tasks requiring seamless spatial detectability, such as tracking the trajectory of a moving object.

Simultaneously, this same material is exceptionally well-suited for advanced microfabrication.
As will be a central theme in this thesis, techniques such as grayscale and soft lithography can be used to impose a precise, custom-designed structure onto the polymer film.
This ability to engineer the material at the micro-scale allows for the creation of "pixe-

---

[7] Seunghwan Seo et al. , **9**: , 2018.
[8] Hang Xu et al. , **4**: , 2024.

lated surfaces" where local properties, such as film thickness, can be controlled. By doing so, each engineered "pixel" or pillar can be equipped with a unique and specific response characteristic.

It is precisely this engineering capability that enables the advanced bio-mimetic goals of this thesis, where arrays of pillars with varying heights will be used to emulate the sophisticated adaptive mechanisms of the human eye.

1.3 Light-Driven Dynamics of PAZO

The material central to this research is poly[1-[4-(3-carboxy-4-hydroxyphenyl-azo) benzene sulfonamido]-1,2-ethanediyl, sodium salt], commonly known as PAZO.

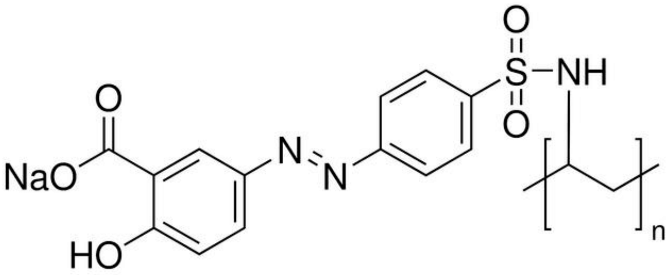

Figure 1.4: Chemical structure of the PAZO polymer (From [9])

It is a commercially available azopolymer, part of a class of materials that incorporate photo-sensitive azobenzene chromophores into their polymer backbone or side chains (Figure 1.4).

These azobenzene units are well-known for their ability to undergo reversible light-induced *trans–cis–trans* isomerization upon exposure to suitable illumination (Figure 1.5). In particular, when stimulated by a linearly polarized laser beam within its absorption band, the azobenzene molecules undergo successive isomerization cycles that gradually lead to molecular reorientation. This process, triggered by light in the UV–visible range, results in a preferential alignment of the molecules.

According to a simplified statistical model, the photoinduced isomerization alters the spatial distribution of molecular orientations. Molecules can reorient either along the electric field direction of the incident light or perpendicularly to it[11].

However, those that adopt an orientation perpendicular to the optical electric field cease to undergo further photoisomerization, while those aligned with the field continue to cycle.

As a consequence, over time, a net molecular alignment perpendicular to the light's polarization axis is established.

---

[11] Carla Madruga et al. , **519**: 8191–8196, 2011.

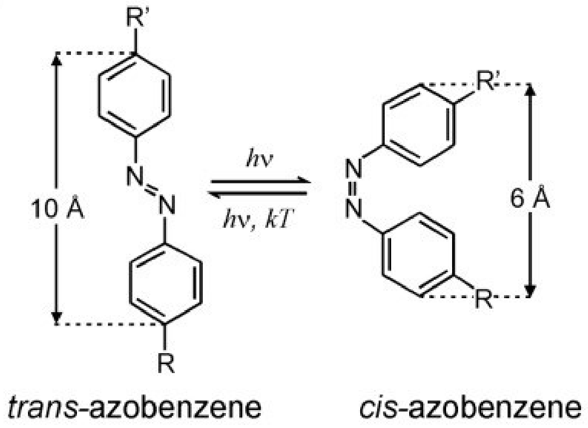

Figure 1.5: Trans-cis isomerization of azobenzene (From [10])

This collective reorientation breaks the initial isotropy of the material and gives rise to birefringence, a condition in which the refractive index becomes dependent on the polarization direction of transmitted light.
From an optical point of view, this corresponds to a gradual transition from a low transmittance state (**LTS**), characteristic of the pristine isotropic condition, to a high transmittance state (**HTS**), where birefringence rotates the polarization of a probing white light beam and enables partial transmission through crossed polarizers. This physical change allows information to be encoded directly into the material's internal state.

To observe this change, a cross-polarized white light imaging system has been employed. In its initial, relaxed state, the PAZO film is isotropic, and no light passes through the crossed polarizers.
However, once stimulated, the induced birefringence alters the polarization state of the probing white light, allowing a portion of it to pass through the second polarizer and be captured as a measurable intensity signal by a CCD camera (Figure 1.6).

The response of the system is inherently dynamic and governed by two competing processes.
The light-driven potentiation is associated with fast photoisomerization kinetics, while the spontaneous relaxation is governed by slower, thermally activated reorientational motion that tends to restore the initial random orientation.
As a result, the buildup and decay of birefringence both follow double-exponential dynamics, as widely reported in the literature [11].

The final state reached after stimulation depends not only on the polarization and wave-

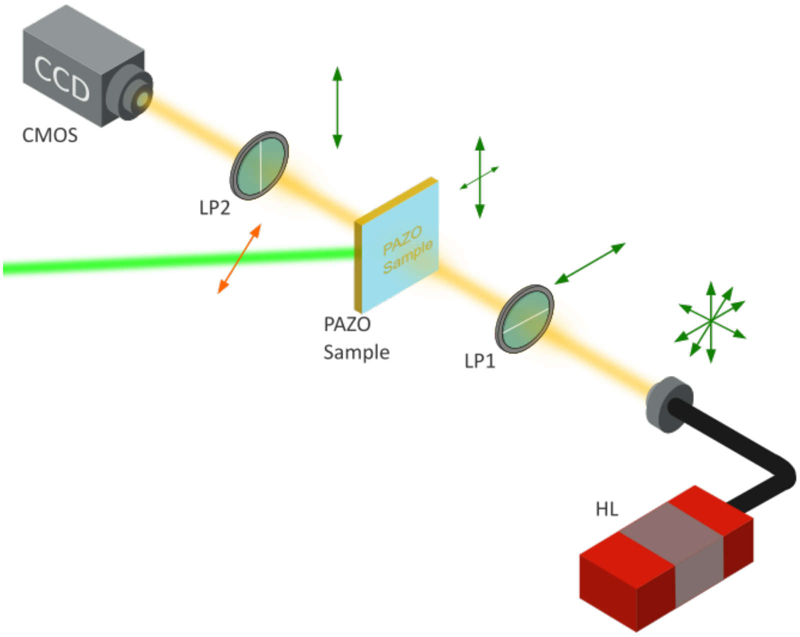

Figure 1.6: Illustration of the cross-polarized white light imaging system

length of the incident light but also on the duration and intensity of the stimulus. Prolonged or intense stimulation can lead to persistent anisotropy that remains for extended periods, while moderate exposures result in gradual spontaneous fading back to the **LTS**. Moreover, by switching from linearly to circularly polarized light, the average molecular orientation can be randomized, effectively returning the system to its pristine isotropic state.

The nonlinear interplay between the two competing mechanisms, a fast light-driven potentiation and a slower thermally activated relaxation, is what gives to the material the ability to not just store information, but to process it dynamically.
The state of the material at any given moment is a direct reflection of its recent history of stimulation.

1.4 Thesis Objectives

Building upon this established foundation of light-driven dynamics and memory emulation, this thesis aims to investigate and develop two novel functionalities for the PAZO material.
The research tries to push its bio-mimetic capabilities into new domains, focusing on tasks of direct relevance to artificial sensory systems.
The main objectives are as follows:

- **Emulate scotopic and photopic vision through microstructuring:** A key challenge for any artificial visual system is adapting to the vast range of light intensities encountered in the real world. The human visual system solves this by using two types of photoreceptors: highly sensitive rod cells for low-light (scotopic) vision and less sensitive cone cells for bright-light (photopic) vision.

This research will explore whether a similar adaptive sensitivity can be engineered into the PAZO platform.

By fabricating microstructured samples containing regions of varying film thickness, I will investigate how thickness modulates the material's optical response.

The central hypothesis is that thicker regions, by absorbing more light, will exhibit a stronger response at low intensities (acting as artificial "rods"), while thinner regions will require higher intensities to trigger a significant response (acting as artificial "cones"). On the other hand, at high intensities the thicker regions will saturate faster because of the stronger response, while the thinner ones will still be measurable.

The successful demonstration of this principle would represent a significant step toward creating adaptive optical sensors that can automatically adjust their dynamic range to different lighting conditions.

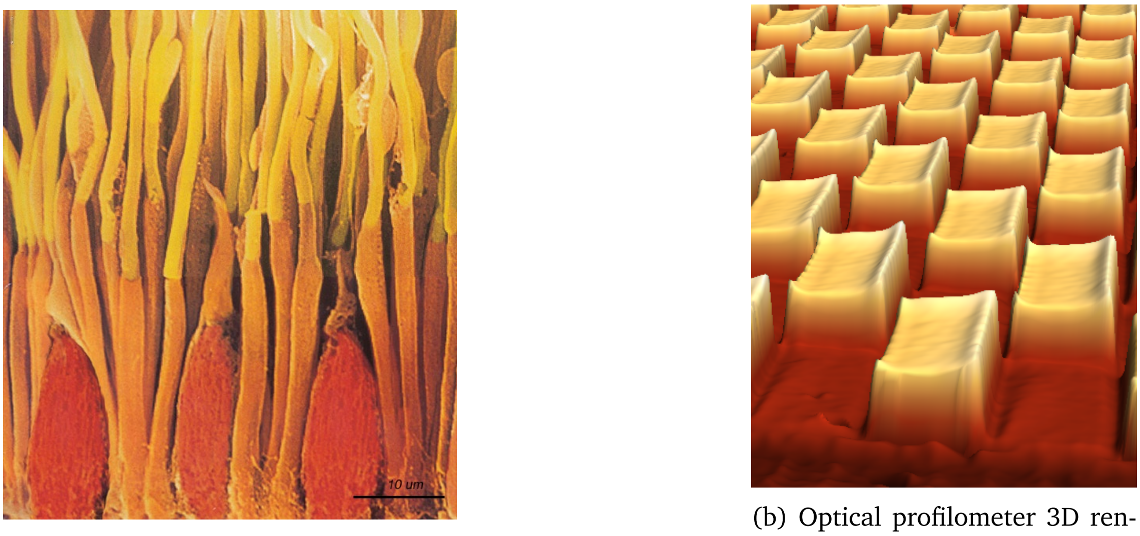

(a) Scanning Electron micrograph of cones and rods of a primate retina

(b) Optical profilometer 3D rendering detail of a microstructured sample

Figure 1.7: Comparison between the structure of the rods and cones in the retina (From [12]) and the structure of the PAZO microstructured pillars trying to emulate their behavior

- **Investigate Wavelength-Selective Response for Color Recognition:**
  The ability to perceive and distinguish color is a fundamental aspect of vision.
  It is known that the dynamic response of azopolymers is dependent on the wavelength of the stimulating light.
  This research will conduct a quantitative investigation of this phenomenon.
  The objective is to characterize the material's unique potentiation and relaxation

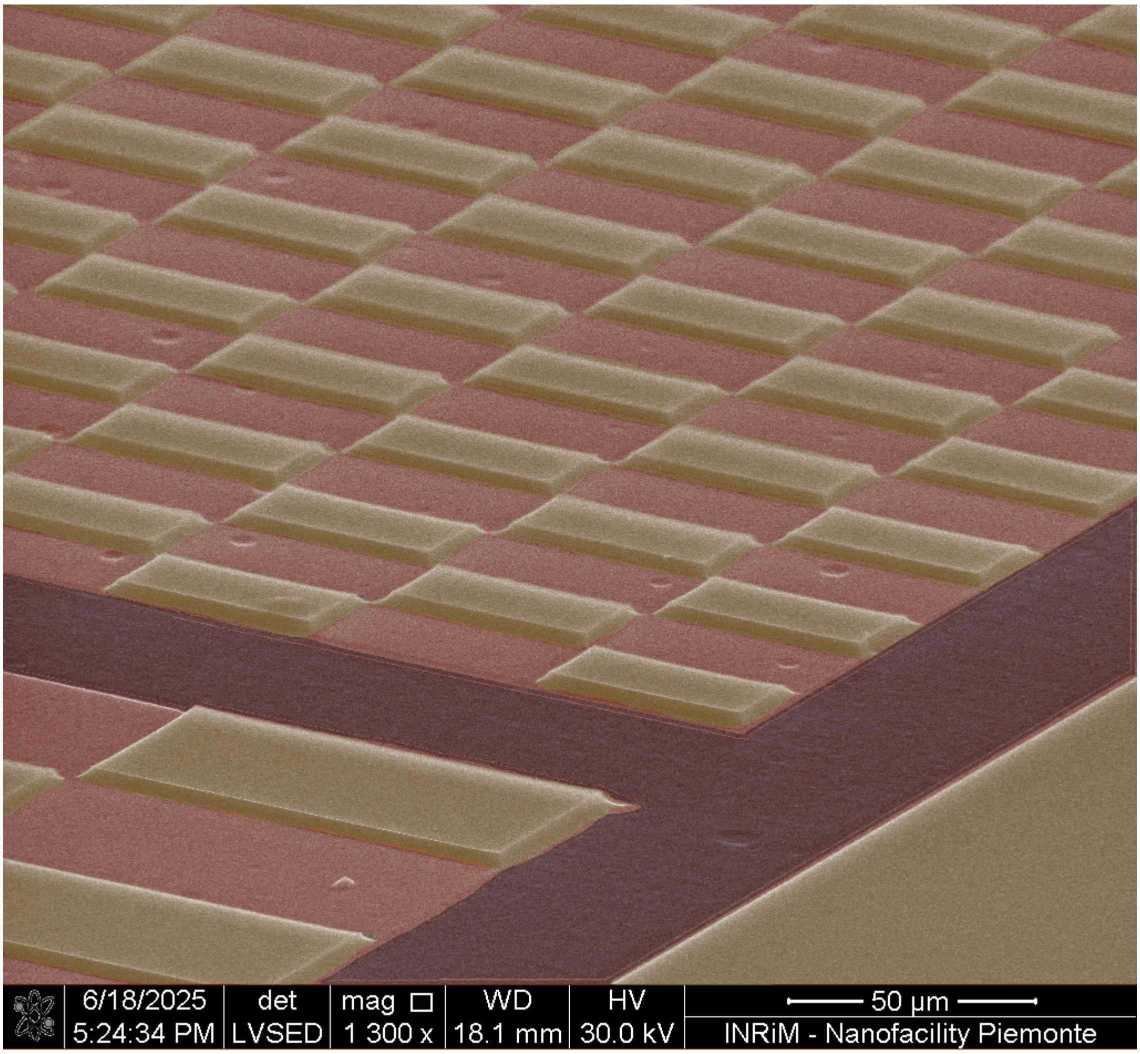

Figure 1.8: Colorized SEM image of the final microstructured PAZO sample

profiles when stimulated by distinct wavelengths of light (violet and green) across a range of optical powers and pulse durations. The core hypothesis is that each color will produce a distinct temporal "fingerprint" in the material's relaxation curve. Capturing these unique signatures would be a first step in the realization of an in-matter color recognition system, able to reliably classify the color of an unknown light stimulus.

2 | Theoretical Background

2.1 Lithography

2.1.1 Optical Lithography

Optical lithography (or Photolithography) is the most widespread micro/nanofabrication method that allows the transfer of a desired pattern on a substrate through the selective exposure of a photosensitive material, called photoresist.

The Photolithographic process can be divided into several steps, here I present the main ones, but many variations or intermediate steps can be applied, depending on the specific application [13]:

- **Substrate Cleaning**: Remove particles on the surface as well as any traces of organic, ionic, and metallic impurities to promote adhesion, surface homogeneity and reproducibility in the subsequent resist deposition step.
- **Photoresist Deposition and Spin Coating**: The photoresist is dispensed onto the substrate which is held by a vacuum chuck and then put in rotation with a certain spin speed and for a certain time. The combination of spin speed, time selected, solution's concentration and molecular weight, will generally define the final film thickness.
- **Soft Bake (or Pre-Bake)**: After the previous step, the resist still contains a portion of solvent, so it is necessary to soft bake the substrate, to remove it and and to promote adhesion of the resist layer to the substrate.
- **Exposure**: The resist-coated substrate are transferred to an illumination or exposure system where they are aligned with the features on a mask, that is a flat glass or quartz plate with an absorber pattern metal, the former material being transparent to the wavelength of the exposure source, the latter shadowing the underlying regions preventing their exposition.

  The standard exposure source in near UV exploits the g-line ($435\ nm$) or i-line

---

[13] Marc Madou and Chunlei Wang. In: *Photolithography*. Bharat Bhushan, ed. 2051–2060. Dordrecht: Springer Netherlands, 2012. DOI: `10.1007/978-90-481-9751-4_342`

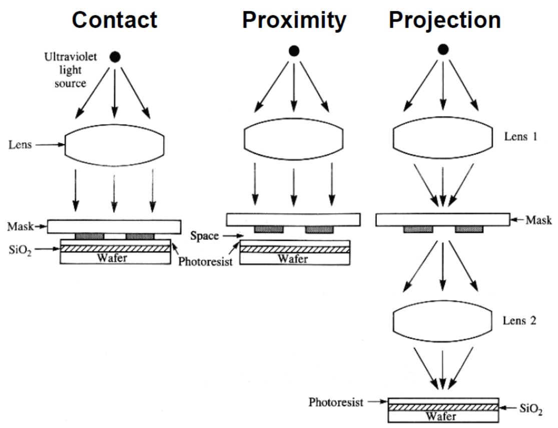

Figure 2.1: Exposure systems schematic illustration

(365 nm) of a mercury lamp that pass through a system of lenses to focus it over the mask that can be directly in contact with the substrate (*Contact*), short distance away from it (*Proximity*), or with an optical system interposed between itself and the substrate surface, to forms a scaled-down image of the mask onto the resist surface (*Projection*) (Figure 2.1).

- **Development**: It consists of the selective dissolution of a portion of the photoresist, allowing the desired pattern to finally appear on the substrate, thanks to a chemical solution called developer. The selective dissolution depends on the nature of the photoresist.

Photoresists are light-sensitive materials composed by a mixture of chemical components, each playing a distinct role in defining the resist's performance and properties, the most important beings:

- **Inactive polymer resin**: A binder that provides mechanical/chemical properties such as adhesion, chemical resistance, rigidity and thermal stability.
- **Solvent**: Control the viscosity of the base keeping it in liquid state allowing the photoresist to be spun and to form thin layers over the substrate surface.
- **Photo-Sensitive Component**: A light-responsive chemical that undergoes a photochemical reaction upon exposure, altering the solubility of the photoresist.

Photoresists can be divided into two major classes based on the nature and mechanism of this last component:

- **Positive Resists**: This class of resists generally consists of a polymer structure sensitized by a so-called Photo-Active Compound (PAC). Most commercially available g-line (436 nm) to i-line (365 nm) resists use a Novolac polymer structure sensitized by a DiazoNaftoQuinone(DNQ) derivative.
  Adding DNQ to the Novolac polymer inhibits the dissolution in areas where the resist

is unexposed, while the exposure reaction increases the dissolution rates by 2-3 orders of magnitude in the exposed regions (Figure 2.2) this dissolution rate increase is caused by photons that break the polymer chains, making them more soluble in the developing solution.

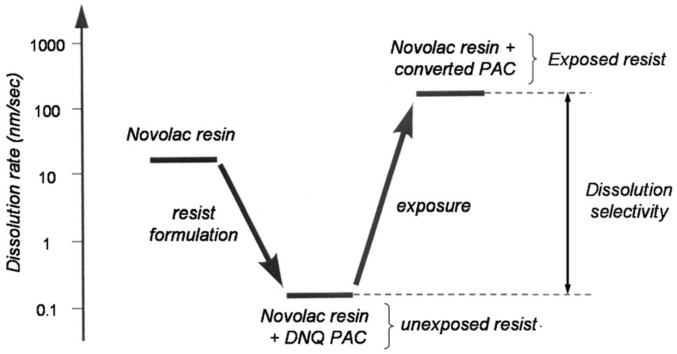

Figure 2.2: Typical positive resist dissolution rate evolution (From [14])

- **Negative Resists**: This class of resists contains a polymer structure combined with a photo-sensitive component, typically a photoinitiator or a photoacid generator (PAG). Upon exposure to light, this component generates reactive species that trigger polymer cross-linking. Unlike positive resists, where exposure increases solubility, negative resists become more resistant to dissolution upon exposure, defining the final pattern [15].

In Figure 2.3, the different behavior of negative and positive photoresist upon illumination is illustrated.

Of the three exposure systems presented above, the projection one is nowadays the most used over the other two for different reasons:

- **No mask contamination**: In contact exposure, the mask is in direct contact with the substrate, increasing the probability of contamination of the mask that would require periodic cleaning to avoid repeating defects on subsequent substrates.

- **De-magnification**: In contact and proximity exposure the mask should be the same size of the wafer to expose and the desired features sizes on it have to be already realized onto the mask. Instead in exposure systems, the mask could be realized with larger features that then are de-magnified thanks to the combined use of diffraction and objective lens (see later).

- **Greater resolution**: In exposure systems only a small portion of the mask is imaged.

---

[15] Wayne M. Moreau. In: *Negative Photoresists*. 157–210. Boston, MA: Springer US, 1988. DOI: `10.1007/978-1-4613-0885-0_4`

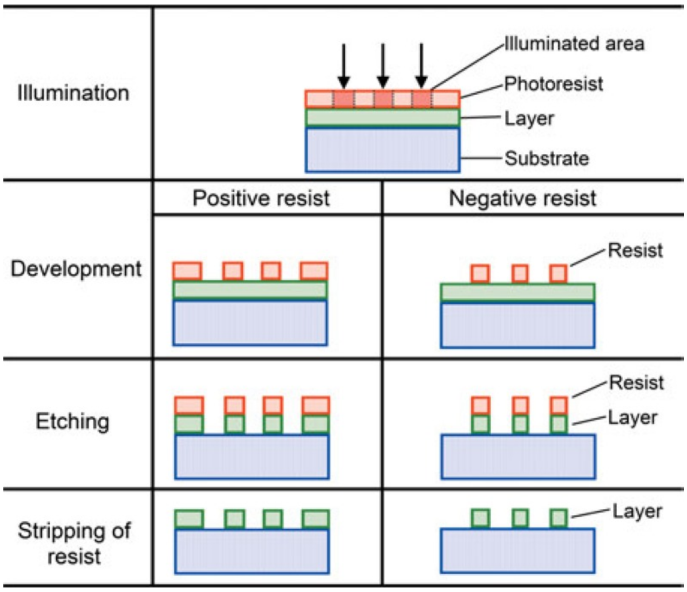

Figure 2.3: Typical Lithographical steps with positive and negative photoresist (From [16])

2.1.2 Maskless Lithography and Grayscale Lithography

Photolithography is a fast and efficient fabrication technique, but it has strong limitations in terms of cost and flexibility, in particular in the exposure step.

Photomask production has become more and more complex and expensive with the reduction of the technological node and so of the critical dimension (CD) (the size of a feature printed in the photoresist) in the microelectronic industry[17]: in fact time consuming optical proximity effect corrections (OPCs) and resolution enhancement techniques (RETs) are necessary to meet the requirements over smaller CDs, together with precise alignment steps between the substrate and the exposure system. This makes rapid prototyping and low-volume production impractical, as any modification in the design requires the creation of a new mask, that is expensive other than time consuming.

To overcome these problems, a sustainable alternative is Maskless lithography (MPL), which consists in exposing a pattern directly onto the substrate surface using a 'dynamic' photomask. There are generally two distinct exposure modes (Figure 2.4):

- **Raster Scan Mode**: the pattern is exposed directly onto the substrate surface using a spatial light modulator (SLM), which acts as a "dynamic photomask".
  The exposure light passes through the SLM that is a digital micro-mirror device with its individual mirrors that are switched in order to represent an area of the design, and are timed in order to yield the desired exposure dose.
  The image is projected onto the substrate through a lens system and the spacimen stage is stepped precisely in order to expose the entire design on the sample.

---

[17] P.Gabella C.Weber N.Berglund. Mask Cost and Profitability in Photomask Manufacturing: An Empirical Analysis. *Semiconductor Manufacturing, IEEE Transactions on*, **19**: 465 –474, 2006. DOI: `10.1109/TSM.2006.883577`

- **Vector Scan Mode**: the light source, typically a laser, is focused on the substrate through a lens system. By moving the stage at a constant velocity while switching the laser on and off, the pattern represented in the design is exposed in the resist. The dose given by the light source is modulated digitally by the design data in order to replicate the desired pattern.

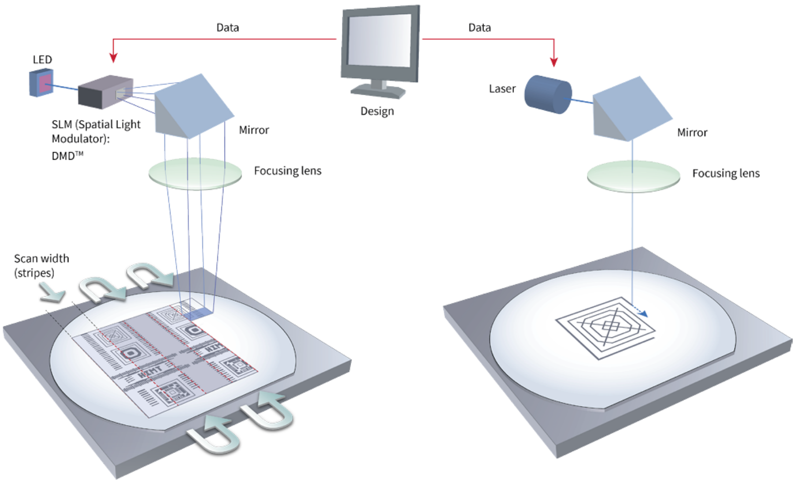

Figure 2.4: Raster (left) and Vector (right) scan mode comparison (From [18])

In particular, for this work, I have used the Heidelberg Instruments Micro Pattern Generator μPG 101 that offers both exposure modes, together with the additional feature called Grayscale Mode.

As previously mentioned, standard photolithography typically relies on binary exposure masks, which define well-defined regions that are either fully exposed or completely unexposed. This approach allows the creation of structures with uniform heights, limited by the thickness of the resist, but it lacks the capability to produce continuous topographies with variable heights in a single exposure step
In recent years a solution to overcome this deficiency has been the development of Grayscale Lithography, a technique that enables the fabrication of three-dimensional microstructures modulating the exposure dose given to the photoresist. Instead of using a binary mask, grayscale lithography employs gradual variations in light intensity to induce controlled partial exposure of the resist, allowing for height differentiation within a single lithographic step[19].

This technique has gained increasing attention in applications where continuous topographies are essential, such as microlens arrays, microfluidic channels, diffractive optical

---

[19] Svetlana N. Khonina, Nikolay L. Kazanskiy, and Muhammad A. Butt. Grayscale Lithography and a Brief Introduction to Other Widely Used Lithographic Methods: A State-of-the-Art Review. *Micromachines*, **15**: 2024. DOI: `10.3390/mi15111321`

elements, and MEMS components [20–23].
By precisely controlling the exposure dose, it is possible to achieve complex profiles that would otherwise require multiple patterning and etching steps in standard photolithography.

Among the various approaches to grayscale lithography, Maskless Lithography Systems have emerged as a particularly flexible and efficient solution[24].
This approach combine the advantages of grayscake and maskless lithography described above: traditional mask-based grayscale require the fabrication of costly grayscale masks while maskless systems exploit dynamically and digitally controlled exposure sources, such as Digital Micromirror Devices (DMDs) or laser scanning systems, to directly modulate light intensity at each point of the substrate.

2.2 Soft Lithography

Soft lithography refers to a set of microfabrication techniques that rely on the use of elastomeric materials, typically *poly(dimethylsiloxane)* (**PDMS**), to replicate, transfer, or mold micro and nanoscale features onto a target substrate.
Unlike traditional photolithography, which requires rigid masks, high-energy radiation, and cleanroom infrastructure, soft lithography provides a low-cost, versatile, and accessible alternative for patterning surfaces with micrometric precision[25].

The core principle of soft lithography is the use of a flexible stamp or mold, often replicated from a master structure, which is brought into contact with the target substrate under controlled conditions of pressure, temperature, or chemical environment.
The elastomeric nature of PDMS allows for conformal contact over large areas, even on slightly nonplanar surfaces, making it particularly suitable for applications in soft materials, organic electronics, optics, and microfluidics.

PDMS is widely employed due to its favorable properties: it is optically transparent, biocompatible, chemically inert, and mechanically stable over a range of operating conditions. Its ability to replicate features with sub-$100\ nm$ resolution and its easy processing make it the standard material for soft lithographic tools[27].

---

[20] Sergio Aristizabal et al. , **52**: 125101, 2013.
[21] Mohamed Adel et al. , **14**: 1370, 2023.
[22] Angelos Bouchouri et al. , **15**: , 2024.
[23] Yong Zhou et al. *Laser speckle grayscale lithography: a new tool for fabricating highly sensitive flexible capacitive pressure sensors* 2024 DOI: `10.37188/lam.2024.016`
[24] Anya Grushina. Direct-write grayscale lithography. *Advanced Optical Technologies*, **8**: 163–169, 2019. DOI: `doi:10.1515/aot-2019-0024`
[25] Younan Xia and George M. Whitesides. , **37**: 550–575, 1998.
[27] Aline Cerf and Christophe Vieu. , **342**: 136–140, 2009.

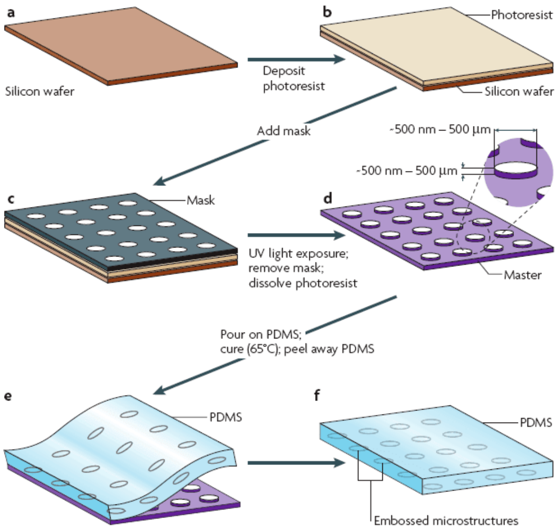

Figure 2.5: Typical processing scheme in soft lithography (From [26]

The fabrication of the PDMS stamp typically begins with a rigid master, which contains the desired micro or nanostructured relief pattern. This master is commonly fabricated using photolithography on a silicon or glass substrate.
The PDMS prepolymer is prepared by mixing the base and curing agent—typically in a 10:1 weight ratio—followed by degassing under vacuum to remove air bubbles. The liquid mixture is then poured over the master and allowed to cure at elevated temperature (commonly $60\breve{}80^{\circ}C$ for $1-2$ hours). Once fully cured, the PDMS layer is gently peeled off from the master, yielding a negative replica of the original structure (Figure 2.5).

The resulting PDMS mold or stamp can be used multiple times, and its surface features faithfully reproduce the topography of the master with high fidelity. Depending on the intended soft lithography technique, the stamp may be used as a passive mold for casting materials, or as an active element for transferring material onto a target surface.

Within this framework, several soft lithography techniques have been developed, each tailored to specific applications and material requirements. In the present work, three distinct soft lithographic approaches have been employed:

- Micro-transfer molding (μTM),
- Solvent-assisted microcontact molding (SAMIM),
- Soft molding (SM).

Each of these techniques relies on the use of a PDMS replica of a master structure, but differs in the mechanism by which the material is transferred, molded, or patterned.

Micro-transfer Molding (μTM)

Micro-transfer molding (μ**TM**) is a soft lithographic technique designed to replicate and transfer isolated microstructures from a patterned mold to a target substrate.

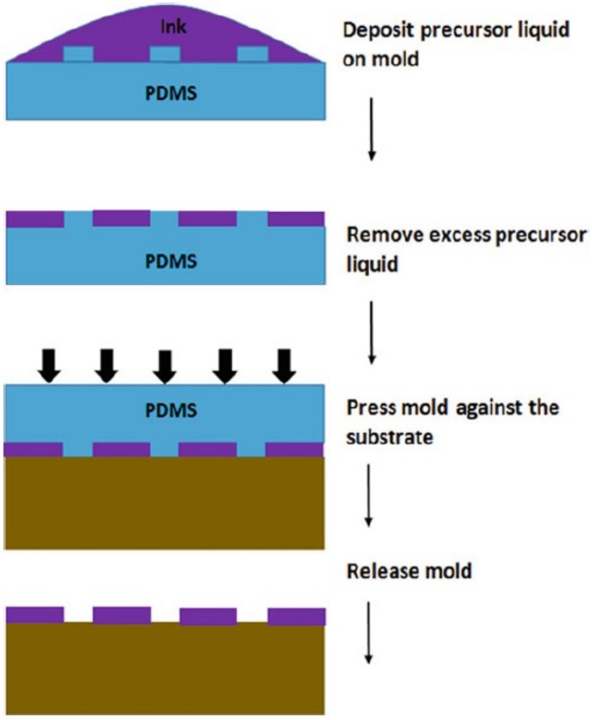

Figure 2.6: Illustrated steps in μTM (From [28])

The process begins with a PDMS mold obtained from a structured master. The recesses of this mold are filled with a polymer precursor, typically a UV-curable or thermally curable resin, while excess material on the raised areas of the mold is carefully removed, for example by scraping or contacting with a flat surface. This ensures that the prepolymer remains confined to the recessed features only.

Next, the PDMS mold is brought into conformal contact with the target substrate, which can be a rigid or flexible material such as silicon, glass, metal oxides, or polymers.
The curing of the prepolymer is then performed, either thermally or via UV exposure, depending on the chemistry of the material. Notably, PDMS is optically transparent down to approximately $280\ nm$, allowing UV curing to be carried out even in contact with opaque substrates like silicon[29].

Once the curing step is complete, the PDMS mold is peeled off, leaving behind the patterned polymeric structures attached to the substrate. This process effectively transfers

---

[29] Byron D. Gates. , **8**: 44–49, 2005.

the replicated features from the mold to the final surface (Figure 2.6).

One of the advantages of μTM is its compatibility with nonplanar or curved surfaces, thanks to the flexibility of the PDMS mold. Additionally, complex three-dimensional structures can be fabricated by repeating the molding and transfer process in a layer-by-layer fashion.

However, μTM also presents certain limitations. A common issue is the formation of a residual thin film of polymer that connects the isolated features. This occurs when a small amount of prepolymer remains on the raised regions of the mold and is transferred along with the desired structures. Such residue can be removed post-process using reactive ion etching (RIE).

Solvent-Assisted Microcontact Molding (SAMIM)

Solvent-Assisted Microcontact Molding (SAMIM) enables the fabrication of three-dimensional microstructures on polymeric surfaces through the combined use of a patterned elastomeric mold and a solvent that softens the substrate.

The SAMIM process begins with a PDMS mold with the desired relief pattern. A solvent capable of dissolving or swelling the polymeric substrate is uniformly applied to the surface of the PDMS mold, ensuring that the solvent wets the recessed regions of the mold. Upon contact with the polymer surface, the solvent partially dissolves or softens a thin surface layer of the substrate, forming a transient gel-like phase that conforms to the topography of the mold.

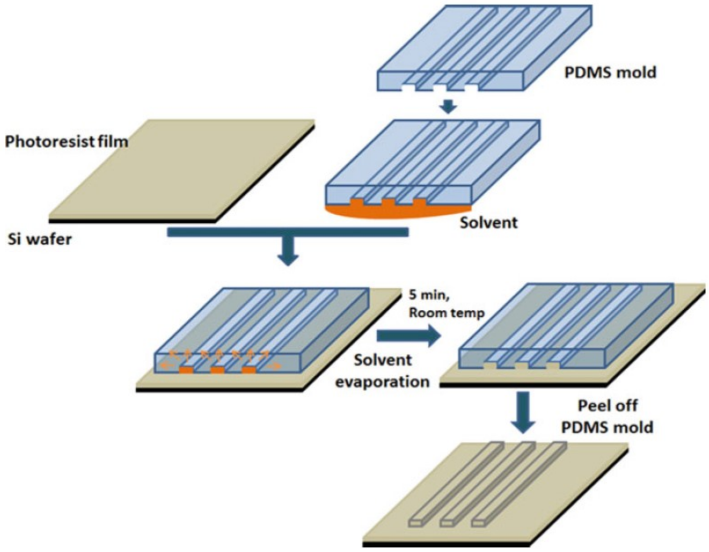

Figure 2.7: Illustrated steps in SAMIM (From [28])

As the solvent evaporates, the polymer re-solidifies, locking in the negative relief of the PDMS mold. The mold is then peeled off, revealing a patterned microstructure on the polymeric surface that faithfully reproduces the original features.
This process occurs without the need for applied pressure or elevated temperatures, relying instead on spontaneous conformal contact between the PDMS and the softened substrate (Figure 2.7).

A critical parameter in SAMIM is the choice of solvent. It must effectively soften the polymer surface without swelling or degrading the PDMS mold. Solvents with high vapor pressure and moderate surface tension, such as ethanol, methanol, and acetone—are typically preferred[30].
Non-polar solvents like hexane and toluene are generally avoided due to their tendency to swell PDMS and compromise the fidelity of the pattern transfer.

A common byproduct of the process is a thin residual film connecting adjacent features, typically below 100 nm in thickness; this can be removed post-process using reactive ion etching (RIE).

SAMIM is compatible with large-area patterning, and unlike techniques such as micromolding in capillaries (**MIMIC**), it is not limited to hydraulically connected structures.

Soft Molding (SM)

Soft molding (**SM**) is a soft lithographic method designed to fabricate three-dimensional microstructures on polymer films addressing several limitations observed in related approaches such as SAMIM and μTM, particularly in terms of structural distortion, surface roughness, and residual stresses.

The process begins with the spin coating of a polymer solution onto a substrate without undergoing a baking step.
Immediately after spin coating, an elastomeric mold (typically PDMS), containing the desired relief structure, is gently placed onto the wet film and pressed lightly (at pressures lower than $1\ N/cm^2$). After this brief contact, the pressure is released and the mold–substrate assembly is left undisturbed for a defined period (typically $10\breve{}15$ minutes) at ambient conditions[31].
During this time, the solvent present in the polymer film diffuses toward the mold–polymer interfaces, where it is absorbed by the PDMS mold and subsequently dissipated through evaporation.
This solvent migration enables the polymer to flow and conform precisely to the features

---

[30] Enoch King et al. , **9**: 651–654, 1997.

[31] Y. S. Kim, K. Y. Suh, and Hong H. Lee. , **79**: 2285–2287, 2001.

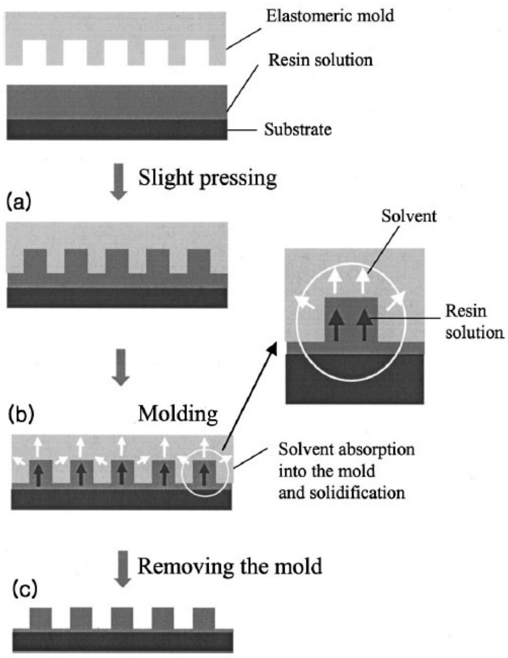

Figure 2.8: Illustrated steps in SM (From [31])

of the mold. Once solvent removal is complete, the polymer solidifies, and the mold is peeled away, leaving behind a well-defined three-dimensional microstructure Figure 2.8.

2.3 Birefringence

Birefringence is an optical property of certain materials whose refractive index depends both on the polarization and on the propagation direction of light. It has been discovered and described at first in optically anisotropic crystals (i.e Calcite crystal) where the crystal structure order and symmetry can determine different velocities of light propagation along different directions.

The classical model to illustrate the phenomena is the electron bound to a set of elastic springs with different stiffnesses, along the three principal axes, such to emulate the oscillation behavior of bound electron in crystals when subjected to an external electric field E. In general the electric susceptibility χ, connecting the electric field E to the polarization P is a tensor

$$\chi = \begin{bmatrix} \chi_{11} & \chi_{12} & \chi_{13} \\ \chi_{21} & \chi_{22} & \chi_{23} \\ \chi_{31} & \chi_{32} & \chi_{33} \end{bmatrix} \tag{2.1}$$

and the relation between P and E can be written as

$$\begin{bmatrix} P_x \\ P_y \\ P_z \end{bmatrix} = \epsilon_0 \begin{bmatrix} \chi_{11} & \chi_{12} & \chi_{13} \\ \chi_{21} & \chi_{22} & \chi_{23} \\ \chi_{31} & \chi_{32} & \chi_{33} \end{bmatrix} \begin{bmatrix} E_x \\ E_y \\ E_z \end{bmatrix} \tag{2.2}$$

that can be abreviated as

$$\mathbf{P} = \epsilon_0 \chi \mathbf{E} \tag{2.3}$$

with the corresponding displacement vector D being

$$\mathbf{D} = \epsilon_0(\mathbf{1} + \chi\mathbf{E}) = \epsilon E \tag{2.4}$$

with

$$\mathbf{1} = \begin{bmatrix} 1 & 0 & 0 \\ 0 & 1 & 0 \\ 0 & 0 & 1 \end{bmatrix} \qquad \epsilon = \epsilon_0(\mathbf{1} + \chi) \tag{2.5}$$

where ϵ is called *dielectric tensor*.

For a non-absorbing crystal, a set of coordinate axes, called *principal axes*, can be chosen such that the susceptibility tensor can assume a diagonal form.

$$\chi = \begin{bmatrix} \chi_{11} & 0 & 0 \\ 0 & \chi_{22} & 0 \\ 0 & 0 & \chi_{33} \end{bmatrix} \tag{2.6}$$

The values on the diagonal are known as *principal susceptibilites* and the corresponding values $K_{11} = 1+\chi_{11}$, $K_{22} = 1+\chi_{22}$, $K_{33} = 1+\chi_{33}$ are called *principal dielectric constants*.

The wave equation for non-magnetic and electrically neutral material

$$\boldsymbol{\nabla} \times (\boldsymbol{\nabla} \times \mathbf{E}) + \frac{1}{c^2}\frac{\partial^2 \mathbf{E}}{\partial t^2} = -\mu_0 \frac{\partial^2 \mathbf{P}}{\partial t^2} - \mu_0 \frac{\partial \mathbf{J}}{\partial t} \tag{2.7}$$

can be rewritten using 2.3 to obtain

$$\boldsymbol{\nabla} \times (\boldsymbol{\nabla} \times \mathbf{E}) + \frac{1}{c^2}\frac{\partial^2 \mathbf{E}}{\partial t^2} = -\frac{1}{c^2}\chi \frac{\partial^2 \mathbf{E}}{\partial t^2} \tag{2.8}$$

This equation can be used to find the conditions for which a monochromatic plane wave ($e^{i(k \cdot r - \omega t)}$), can travel through the material resulting in this equation:

$$\mathbf{k} \times (\mathbf{k} \times \mathbf{E}) + \frac{\omega^2}{c^2}\mathbf{E} = -\frac{\omega^2}{c^2}\chi\mathbf{E} \tag{2.9}$$

that expanded in its component is

$$\begin{aligned}\left(-k_y^2 - k_z^2 + \frac{\omega^2}{c^2}\right) E_x + k_x k_y E_y + k_x k_z E_z &= -\frac{\omega^2}{c^2}\chi_{11} E_x \\ k_y k_x E_x + \left(-k_x^2 - k_z^2 + \frac{\omega^2}{c^2}\right) E_y + k_y k_z E_z &= -\frac{\omega^2}{c^2}\chi_{22} E_y \\ k_z k_x E_x + k_z \mathrm{k}_y E_y + \left(-k_x^2 - k_y^2 + \frac{\omega^2}{c^2}\right) E_z &= -\frac{\omega^2}{c^2}\chi_{33} E_z\end{aligned} \tag{2.10}$$

At this point three *principal index of refrection* can be introduced, associated with the three principal susceptibilities like this

$$\begin{aligned}n_1 &= \sqrt{1+\chi_{11}} = \sqrt{K_{11}} \\ n_2 &= \sqrt{1+\chi_{22}} = \sqrt{K_{22}} \\ n_3 &= \sqrt{1+\chi_{33}} = \sqrt{K_{33}}\end{aligned} \tag{2.11}$$

such that the previous set of equations can be rewritten as

$$\begin{aligned}\left(\left(\frac{n_1\omega}{c}\right)^2 - k_y^2 - k_z^2\right) E_x + k_x k_y E_y + k_x k_z E_z &= 0 \\ k_y k_x E_x + \left(\left(\frac{n_2\omega}{c}\right)^2 - k_x^2 - k_z^2\right) E_y + k_y k_z E_z &= 0 \\ k_z k_x E_x + k_z \mathrm{k}_y E_y + \left(\left(\frac{n_3\omega}{c}\right)^2 - k_x^2 - k_y^2\right) E_z &= 0\end{aligned} \tag{2.12}$$

For this equations to have solutions for E_x,E_y and E_z, it is required that the determinant of the coefficients must be 0

$$\begin{vmatrix} (n_1\omega/c)^2 - {k_y}^2 - {k_z}^2 & k_x k_y & k_x k_z \\ k_y k_x & (n_2\omega/c)^2 - {k_x}^2 - {k_z}^2 & k_y k_z \\ k_z k_x & k_z k_y & (n_3\omega/c)^2 - {k_x}^2 - {k_y}^2 \end{vmatrix} = 0 \tag{2.13}$$

The solution to these calculations can be represented by a three-dimensional surface in k space (Figure 2.9) This 3D surface consists of an inner sheet and an outer sheet, a sphere and an elipsoid, and the intercept of the k surface with each coordinate plane, describes therefore a circle and an ellipse. This means that for each wave vector $\mathbf{k}$ there are two possible values for the wavenumber k, and so two phase velocities: in fact $\frac{\omega}{k}$ represent the wave phase velocity. Moreover, it can be demonstrated that the two resulting waves propagating through the crystal, have two mutually orthogonal polarizations.

The nature of the k surface is such that the inner and outer sheets can touch in two points along an axis or in 4 points along 2 axes, where the values of textit$k$ are equal. An axis where the 2 k-surfaces intercept each others is called optic axis: when a wave propagates in the direction of an optic axis will have the phase velocities of the two resulting orthogonally polarized waves reduce to the same value.

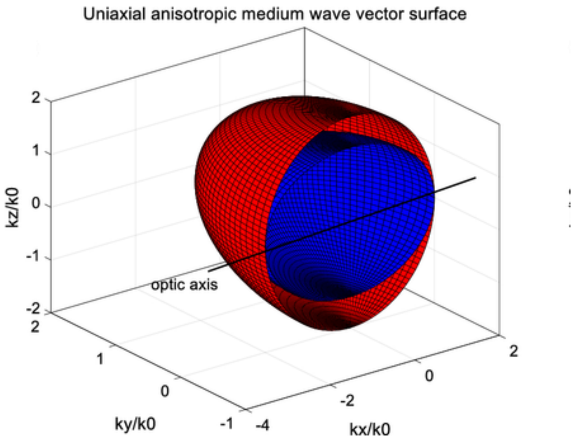

Figure 2.9: k-surface graphical illustration (From [32])

The number of optic axis depends on the nature of the crystal and on its principal indices: when 2 principal indices out of the 3 are equal the crystal is called *uniaxial* meaning there is a single optic axis, while where all 3 principal indices are different the crystal is called *biaxial*, that will have two optic axes.

The two waves corresponding to two different polarization states, resulting from the solution of the wave equation, are generally called the ordinary and extraordinary rays (Figure 2.10).

Ordinary Ray: The ordinary ray is associated with the spherical sheet of the k-surface. It has the following properties:

- Its electric field vector $\mathbf{E}_o$ is always perpendicular to the optic axis.
- It obeys Snell's law of refraction.
- It has a single refractive index, called the ordinary refractive index n_o, which is independent of the direction of propagation.

Extraordinary Ray: The extraordinary ray is associated with the ellipsoidal sheet of the k-surface. It has the following properties:

- Its electric field vector $\mathbf{E}_e$ has a component parallel to the optic axis.
- It does not obey Snell's law in the simple form.
- Its refractive index, called the extraordinary refractive index $n_e(\theta)$, depends on the angle θ between the wave vector $\mathbf{k}$ and the optic axis in this way

$$n_e(\theta) = \frac{n_e n_o}{\sqrt{n_e^2 \cos^2\theta + n_o^2 \sin^2\theta}} \tag{2.14}$$

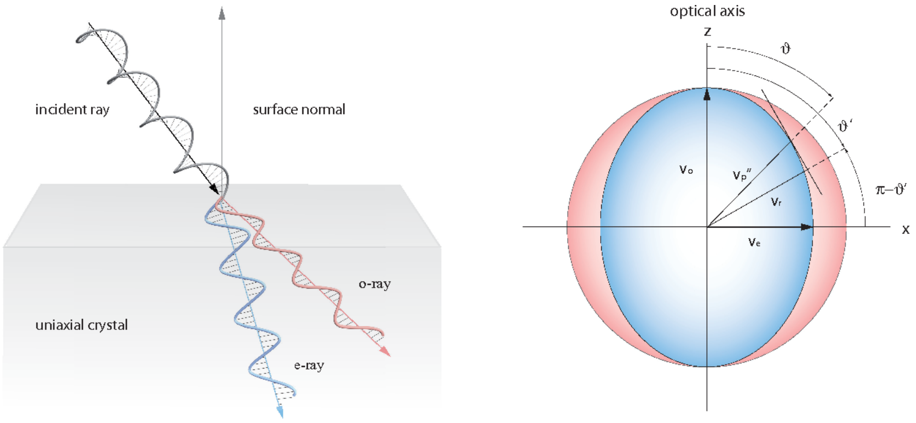

Figure 2.10: Left: Split of an incident ray into an ordinary and an extraordinary ray. Right: Ray-velocity surface for an uniaxial crystal (From [33])

To analyze how the polarization state of light is affected by propagation through a uniaxial crystal, the Jones matrix formalism can be used.
For simplicity let's consider a uniaxial crystal of thickness d, with the optic axis oriented such that the x and y axes coincide with the principal axes of the crystal for the given direction of propagation.
The ordinary and extraordinary rays will accumulate different phases as they propagate through the crystal due to the difference in their refractive indices:

$$\begin{aligned} \phi_x &= \frac{2\pi}{\lambda} n_o d \\ \phi_y &= \frac{2\pi}{\lambda} n_e d \end{aligned} \tag{2.15}$$

where n_o and n_e are respectively the ordinary and extraordinary refractive indexes and λ is the wavelength of the light in vacuum. Therefore the Jones matrix that describes the effect of the uniaxial crystal on the polarization of the transmitted light is:

$$\mathbf{J} = \begin{bmatrix} e^{i\frac{2\pi}{\lambda} n_o d} & 0 \\ 0 & e^{i\frac{2\pi}{\lambda} n_e d} \end{bmatrix} = e^{i\frac{2\pi}{\lambda} n_o d} \begin{bmatrix} 1 & 0 \\ 0 & e^{i\frac{2\pi}{\lambda}(n_e - n_o) d} \end{bmatrix} \tag{2.16}$$

Often, the overall phase factor $e^{-i\frac{2\pi}{\lambda} n_o d}$ is omitted, as it does not affect the polarization state. The simplified Jones matrix is then:

$$\mathbf{J} = \begin{bmatrix} 1 & 0 \\ 0 & e^{-i\Delta\phi} \end{bmatrix} \tag{2.17}$$

where

$$\Delta\phi = \frac{2\pi}{\lambda} d(n_e - n_o) \tag{2.18}$$

is the phase retardation between the 2 rays and in particular

$$\Delta n = n_e - n_o \tag{2.19}$$

is the measure of the material birefringence.

The output Jones vector $\mathbf{E}_{\text{out}}$ is related to the input Jones vector $\mathbf{E}_{\text{in}}$ by:

$$\mathbf{E}_{\text{out}} = \mathbf{J}\,\mathbf{E}_{\text{in}} \tag{2.20}$$

2.4 Neuromorphic Principles in Visual Adaptation

2.4.1 Artificial synapses

The brain's fundamental processing unit is the neuron, a specialized cell that transmits information through electrical and chemical signals.

A typical neuron comprises a cell body (soma), dendrites that receive incoming signals, and an axon that transmits signals to other neurons (Figure 2.11). Communication between neurons occurs at the so called synapses, the points of contact between the axon terminal of a presynaptic neuron and the dendrite (or soma) of a postsynaptic neuron.

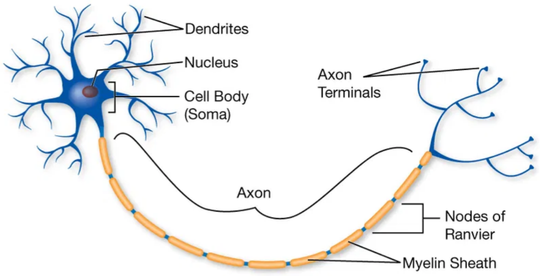

Figure 2.11: Neuron structure

When an electrical signal, known as an action potential or spike, reaches the axon terminal of the presynaptic neuron, it triggers the release of small molecules called neurotransmitters into the synaptic cleft, the narrow gap between the two neurons.

These neurotransmitters bind to receptors on the postsynaptic neuron, generating an electrical signal that can either excite or inhibit the postsynaptic neuron (Figure 2.12).

The strength of this synaptic connection, often referred to as the synaptic weight or strength, is not static but rather a dynamic property that can be modulated by the history and frequency of the incoming stimuli.

This crucial aspect is called synaptic plasticity, the ability of synapses to strengthen (potentiation) or weaken (depression) their connections over time. This flexibility, involving chemical, electrical, and physical changes, is considered the biological basis of learning and memory. Inspired by biological synapses dynamics, researchers have begun devel-

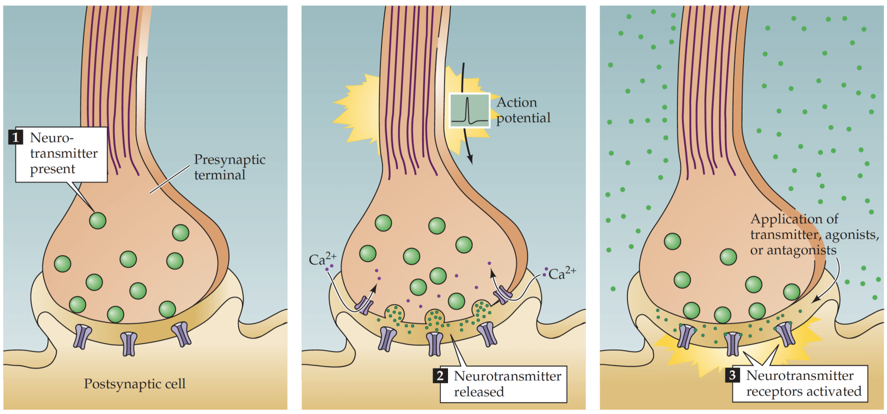

Figure 2.12: Synaptic transmission at synapses (From [34])

oping various electronic devices, including for example memristors[35], resistive switching memories (ReRAM)[36] and ferroelectric materials[37], to create an artificial synapse trying to emulate and exploit synaptic plasticity behavior. These devices exhibit analogue behavior and they have an internal state, like their conductance (or resistance), that can be modulated by the history of applied electrical stimuli, mimicking the plasticity of biological synapses.

To clarify more what in particular artificial synapses are trying to emulate, synaptic plasticity can be generally divided into two two broad classes of plasticity with their particular features: *Short-Term Plasticity* **(STP)** and *Long-Term Plasticity* **(LTP)**.

The two can be distinguished by looking at the change in synaptic weight over time: In LTP the change in the synaptic weight is stable over a time that persists from minutes to hours or longer, while in STP there is a transient change in synaptic strength lasting milliseconds to seconds.

STP main features are generally the three illustrated in Figure 2.13:

- **Paired-Pulse Facilitation (PPF)**: It generally refers to the synaptic weight increase evoked by a pair of stimuli where the response to a second stimulus is enhanced when it closely follows a preceding one with the interval Δt between the two typically ranging from few milliseconds to several seconds.

  In artificial synapses, this mechanism functions as a temporal filter, emphasizing rapid sequences of inputs. By increasing the synaptic efficacy for closely spaced signals, PPF enables the system to prioritize high-frequency information, which is crucial for processing temporal patterns and sequences in data streams.

- **Paired-Pulse Depression (PPD)**: On the contrary of PPF, it is characterized by a reduced response to a second spike when it closely follows the first one. This mechanism serves as a dynamic gain control in artificial synapses, attenuating the influence

---

[35] Woong Huh, Donghun Lee, and Chul-Ho Lee. , **32**: 2002092, 2020.

[36] Jun-Woo Jang et al. “ReRAM-based synaptic device for neuromorphic computing” in: *2014 IEEE International Symposium on Circuits and Systems (ISCAS)*. IEEE 2014. 1054–1057

[37] Le Zhao et al. , **124**: , 2024.

of repetitive or redundant signals. By diminishing the synaptic response to closely spaced inputs, PPD helps prevent overstimulation, ensuring that a new information is not overshadowed by repetitive activity.

- **Post-Tetanic Potentiation (PTP)**: It refers to the transient enhancement ,lasting from 30 s to several minutes, of synaptic strength following a high-frequency train of stimuli, lasting several hundred to thousands of milliseconds (tetanus) [38].
  In artificial systems, PTP acts as a short-term memory mechanism, temporarily boosting the synaptic response to an high-frequency train of inputs.
  This facilitates the reinforcement of patterns that occur in rapid succession, aiding in the consolidation of information and the detection of salient events within a temporal window.

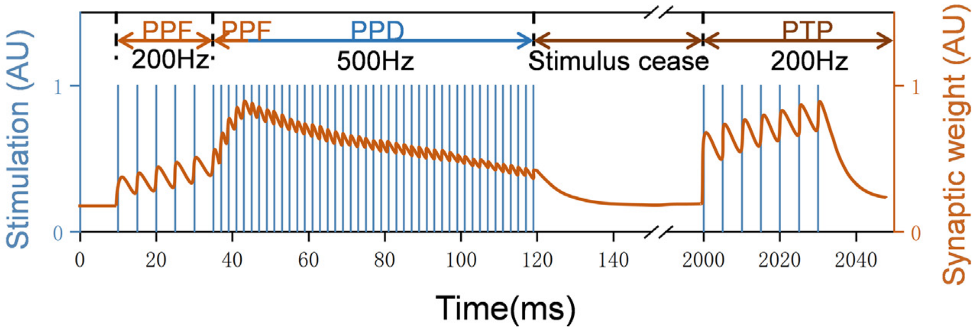

Figure 2.13: Schematic diagram of STP response (From [39])

The typical mechanisms referring to LTP, consisting in a longer and more permanent change in the synaptic weight are:

- **Long-Term Potentiation (LTP)**: It refers to the persistent enhancement of the postsynaptic response to a presynaptic action potential resulting from specific repeated stimulations (Figure 2.14).
  To be considered LTP, the change must persist for at least 1 h following induction[40].
  In the realm of artificial synapses, LTP is fundamental to allow the learning process by solidifying the information coming from an input that frequently spikes. This enduring enhancement enables the system to store information over extended periods, forming the basis for memory and the acquisition of new skills or knowledge.

- **Long-Term Depression (LTD)**: It is characterized by a decrease in postsynaptic strength, typically arising from low-frequency stimulation.
  In addition to being a mechanism for forgetting or preventing synaptic saturation, LTD actively contributes to learning and memory by allowing the retention of specific content details within a spatial representation.

---

[38] Robert S. Zucker and Wade G. Regehr. , **64**: 355–405, 2002.

[40] Eden Anderson and Matthew Hearing. In: *Neural Circuit Plasticity in Addiction*. 35–60. Elsevier, 2019. DOI: 10.1016/b978-0-12-812202-0.00004-x

It plays a critical role in updating spatial information and disambiguating similar memories, supporting pattern separation and preventing generalization.
By weakening or pruning certain synaptic connections, LTD helps to refine neural networks, ensuring they remain adaptable and can precisely encode new informations[41].

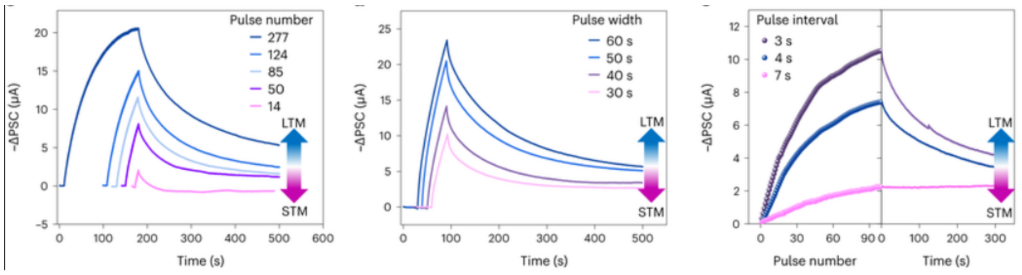

Figure 2.14: STP to LTP transition: there are generally three way in which the transition can happen in such a way to store permanently the information i.e. by increasing pulse number, by prolonging pulse width and by decreasing pulse intervals (From [42])

- **Spike-Timing-Dependent Plasticity (STDP)**: Spike-Timing-Dependent Plasticity is a learning rule where the timing of pre- and postsynaptic spikes determines the direction and magnitude of synaptic changes (Figure 2.15).
  It can partecipate both in potentiation and depression depending on the roles of pre- and post-synaptic spikes that is, if the pre-synpatic pulse come before the post-synaptic one the synaptic strength reduces while on the contrary if the pre- come after the post-synaptic one the synaptic strength is potentiated.
  In artificial synapses, STDP enables the encoding of temporal relationships between events, strengthening connections between the neurons based on temporal spiking. This temporal sensitivity allows the system to learn sequences and predict future inputs based on past activity, enhancing its ability to process temporal patterns.

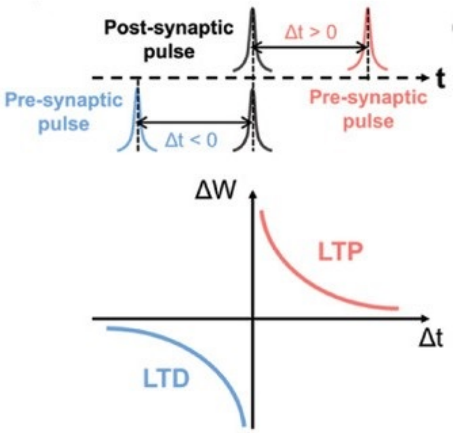

Figure 2.15: Illustration of STDP according to the relative timing of pre-and post-synaptic pulse (From [43])

---

[41] Graham L. Collingridge et al. , **11**: 459–473, 2010.

2.4.2 Human Visual System

The human visual system represents a highly sophisticated biological framework for processing optical information. It transduces incident photons into neural signals and subsequently processes these signals to generate a coherent perceptual representation of the external environment.

The first site of visual signal processing is the retina, the innermost layer of the eye, which is divided into the retinal pigment epithelium and the neural retina.

The former supports photoreceptor function by absorbing scattered light and so reducing image distortion within the eye, while the latter is where the actual phototransduction and initial visual signal processing take place (from now on when I will mention retina I will refer to the neural retina).

The retina is made by five types of neurons organized in multiple layers and they are photoreceptors, bipolar cells, ganglion cells, horizontal cells, and amacrine cells.

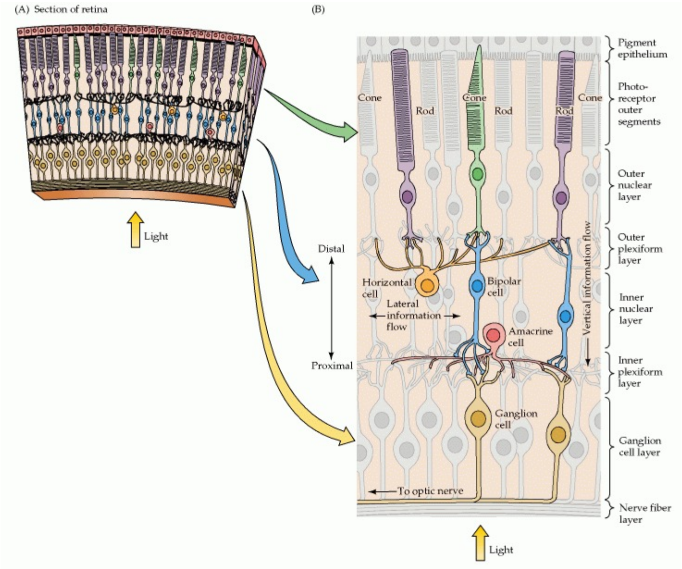

Figure 2.16: Illustration of the retina structure and the five neuron cells which is made of (From [44])

In Figure 2.16 it can be seen how in the human retina the direction of incoming light is opposite to the direction of neural information flow. Light enters the eye and passes through the layers of the neuronal cells mentioned above before reaching the photoreceptors, which are located at the back of the retina.

Once photoreceptors detect light and initiate the phototransduction process, the resulting electrical signals propagate in the opposite direction, from the rear of the retinal structure, through a structured network of interconnected neurons, to the ganglion cells placed at the front, where their larger axons carry the visual information to the rest of the central nervous system.

Each neuronal cell type plays a distinct role in shaping and transmitting visual information, and they interact with each other to realize specific tasks (spatial contrast enhancement, edge detection, motion detection, etc.) making a first "post-processing" of the data already at the eye stage[45].

At the rear part of the retina lie the photoreceptors that are of two types: rods and cones. They are different both structurally and in the photopigments they are made of.

Once photons reach the photoreceptors, the visual system begins its transformation of optical energy into neural information: the photopigment molecules activated by the light lead to a biochemical cascade that ultimately alters the membrane potential of the photoreceptor, modulating its synaptic output.

In darkness, photoreceptors maintain a relatively depolarized resting potential and continuously release the neurotransmitter glutamate at their synaptic terminals.

When exposed to light, the photoreceptor hyperpolarizes, reducing glutamate release in proportion to light intensity[46].

The photoreceptor synaptic terminals are connected to the above mentioned horizontal and bipolar cells that can hyperpolarize or depolarize in response to the glutamate release from the photoreceptor and depending on the specific receptor types. In this way the amount of neurotransmitter released is continuously adjusted based on the light environment, enabling the system to encode a wide range of luminance levels.

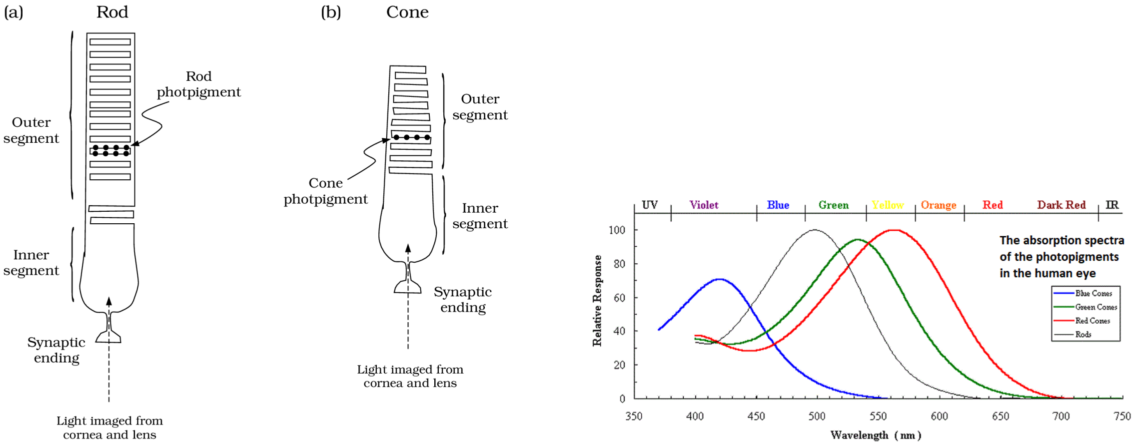

(a) Schematics of rod (a) and cone (b) photoreceptor structure (From [47])

(b) Absorption spectra of rod and the three types of cones

Figure 2.17: Rod and cones

Rods elongated outer segments contain numerous stacked discs, which are densely packed with the photopigment rhodopsin.

Rhodopsin absorbs a broad spectrum of light wavelengths but it gives an achromatic information, since the brain is not capable of distinguish the wavelength of the incoming light based simply on the rod activity.

A key characteristic of rhodopsin is its high photosensitivity; it undergoes photochem-

---

[45] Valentin Dragoi *Visual Processing: Eye and Retina (Section 2, Chapter 14) Neuroscience Online: An electronic textbook for the neurosciences | Department of Neurobiology and Anatomy - The University of Texas Medical School at Houston* URL: `https://nba.uth.tmc.edu/neuroscience/m/s2/chapter14.html`

[46] Ufo Themes *The visual system* en-US May 2019

ical isomerization (bleaching) even at very low photon fluxes. Consequently, rods are exceptionally sensitive to light and are the primary mediators of vision under *scotopic conditions* (low levels of illumination). Their greater abundance of photopigments, due to longer outer segments and more discs, contributes to this enhanced light sensitivity (Figure 2.17a).

Cones, in contrast, typically have shorter, more conical outer segments(Figure 2.17a). They are categorized into three subtypes based on the specific photopigment they contain. Each cone photopigment exhibits peak absorption in different parts of the visible spectrum: short wavelengths (S-cones, typically responding to blue light), medium wavelengths (M-cones, green light), and long wavelengths (L-cones, red light) Figure 2.17b.
The presence of these three spectrally distinct cone types forms the physiological basis for trichromatic color vision.
Cone photopigments are less sensitive to light than rhodopsin, requiring higher illumination levels for activation (Figure 2.18).
Therefore, cones are responsible for controlling vision under *photopic conditions* (high levels of illumination, such as daylight).

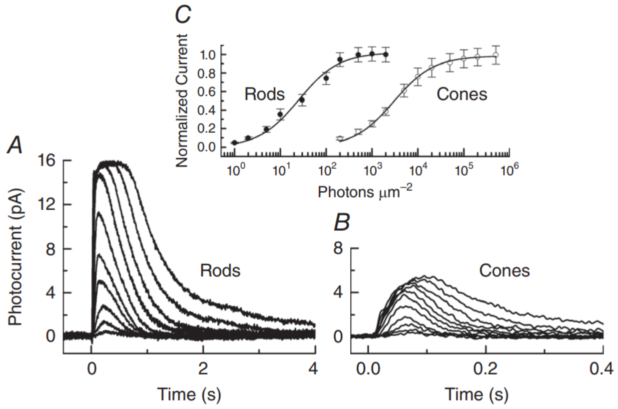

Figure 2.18: Mean peak amplitudes of responses of mouse rods (•) and mouse cones (○) to 20 ms flashes of 500 nm illumination, normalized to maximum response and plotted as a function of flash intensity (From [48])

3 | Synaptic plasticity and visual memory in PAZO

In this chapter, I will first describe the optical setup used for the stimulation of the PAZO samples and the recording of the photoinduced birefringence, explaining how it is built and mathematically modeling how the optical signals are treated in the recording via Jones Matrix formalism.

Then I will present the results stimulating a uniform layer of PAZO on glass with different inputs to show the synaptic plasticity building, as expected in a material trying to mimick a biological synapse. In particular I will show how the PAZO can pass from a short-term to a long-term memory regime changing different parameters (such as the stimulation time or the laser power).

3.1 Characterization of Birefringence in PAZO

3.1.1 Setup Description

To measure the effect of the induced birefringence on the PAZO samples I used an optical setup described in Figure 3.1

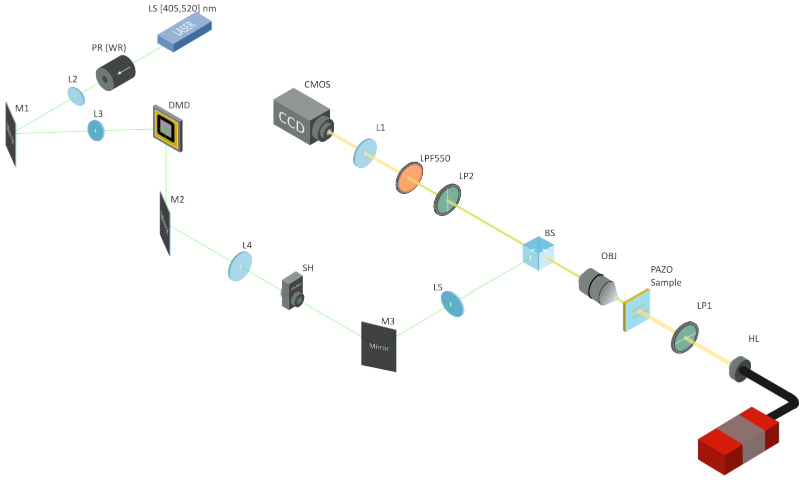

Figure 3.1: Setup illustration

Substantially it is a cross-polarized imaging microscope which uses a broadband halogen light source (**HL**) that is collimated and then filtered by a linear polarizer (**LP1**) before illuminating the PAZO sample.

On the opposite side of the sample, either a 20x or 5x objective lens (**OBJ**) collects the transmitted white light.

This light passes through a 50:50 non-polarizing beam splitter (**BS**) for visible light and is then filtered by a second linear polarizer (**LP2**), oriented perpendicularly to the first, and a long-pass filter with a cut-on wavelength of 550 nm (**LPF550**).

A biconvex lens (**L1**) then forms an image of the sample surface on a CMOS camera (**CMOS**).

During the experiments, the baseline light intensity is determined by subtracting the residual light transmitted through the imaging system and recorded by the camera when the material is in its initial state.

For what concerns stimulation, it is provided by a MatchBox Laser combiners source (**LS**) that emits a linearly polarized Gaussian beam for 4 wavelengths options: $[405, 450, 520, 638]\ nm$.

This beam can pass through a programmable polarization rotator or a programmable wave plate retarder (**PR**) to control its polarization state, including conversion to circular polarization, controlled by a liquid crystal controller.

The beam is then expanded by a beam expander composed of two biconvex lenses (**L2**) before being deviated by a dielectric mirror (**M1**) and shaped by a lens (**L3**), illuminating the display of a Digital Micromirror Device (**DMD**) that allows for arbitrary wavefront shaping. Alternatively, the DMD can be bypassed using a pair of dielectric mirrors to maintain the Gaussian profile of the beam.

The beam shaped by the DMD is then directed along a path by a dielectric mirror (**M2**) where it encounters a lens (**L4**) and a programmable shutter(**SH**) that eventually can block the beam.

Then another dielectric mirror (**M3**) directs the laser beam along a path where a second beam expander (**L5**), adjusts the beam divergence before a beam splitter (**BS**) deflects part of the beam towards the objective lens (**OBJ**), which focuses it onto the sample.

3.1.2 Modellization of the Induced Birefringence in Azopolymers

To describe mathematically what the cross-polarized imaging microscope is measuring, the Jones matrix formalism can be used, as described previously in 2.3.

The goal is to evaluate the changes in polarization state and transmitted intensity as a function of the induced birefringence.

The incident light (**HL**) is modeled as a left-handed circularly polarized wave, represented by the Jones vector

$$\vec{E}_{\text{in}} = \sqrt{I_0} \cdot \frac{1}{\sqrt{2}} \begin{bmatrix} 1 \\ i \end{bmatrix}, \tag{3.1}$$

where I_0 is the input intensity.

This beam first passes through a linear polarizer oriented at $+45^\circ$ with respect to the horizontal axis (**LP1**), described by the Jones matrix

$$\text{Pol}_0 = \frac{1}{2} \begin{bmatrix} 1 & 1 \\ 1 & 1 \end{bmatrix}. \tag{3.2}$$

The polarization-filtered light then enters the PAZO layer, in which a birefringence has been induced by the stimulation apparatus described above.
The optical retardance introduced by the material is given by

$$\delta = \frac{2\pi}{\lambda} \Delta n \cdot d, \tag{3.3}$$

where λ is the wavelength of the light, Δn is the induced birefringence, and d is the thickness of the film.

Assuming the principal optical axis of the birefringent medium is aligned with the x-axis ($\theta = 0$) and there is no in-plane rotation ($\phi = 0$), the Jones matrix of the PAZO layer simplifies to a diagonal form:

$$M_{\text{PAZO}} = \begin{bmatrix} e^{i\delta/2} & 0 \\ 0 & e^{-i\delta/2} \end{bmatrix}. \tag{3.4}$$

Finally, the beam is analyzed with a second polarizer oriented at -45° (**LP2**), whose matrix representation is

$$\text{Pol}_1 = \frac{1}{2} \begin{bmatrix} 1 & -1 \\ -1 & 1 \end{bmatrix}. \tag{3.5}$$

The output electric field after passing through the full system is

$$\vec{E}_{\text{out}} = \text{Pol}_1 \cdot M_{\text{PAZO}} \cdot \text{Pol}_0 \cdot \vec{E}_{\text{in}}. \tag{3.6}$$

The output intensity is then computed as the squared norm of the resulting field:

$$I_{\text{out}} = \left|E_{\text{out},x}\right|^2 + \left|E_{\text{out},y}\right|^2. \tag{3.7}$$

This configuration effectively transforms changes in birefringence Δn into measurable intensity variations. As the retardance δ varies with Δn, the resulting intensity I_{out} exhibits a sinusoidal dependence:

$$I_{\text{out}} = \frac{I_0}{2} \cdot \sin^2\left(\frac{\pi \Delta n d}{\lambda}\right). \tag{3.8}$$

In this way the variations in birefringence can be sensitively detected as modulation of the transmitted intensity, allowing the characterization of the optical anisotropy induced in PAZO by a light source.

3.2 Light-Induced Synaptic Plasticity and Visual Memory

The PAZO polymer exhibits dynamic optical properties that can be effectively exploited to mimic synaptic plasticity mechanisms observed in biological systems.

In particular, its reversible birefringence modulation upon light stimulation, as explained in section 1.3, reproduces the typical features of *short-term memory* (**STM**) and *long-term memory* (**LTM**) effects seen in artificial synapses.

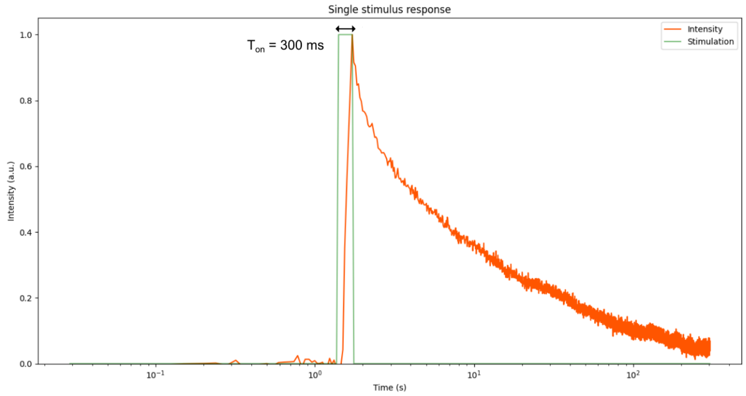

Figure 3.2: Dynamic optical response of a PAZO layer to a single light pulse of duration 300 ms

To illustrate this behavior,Figure 3.2 reports a typical dynamic response of a PAZO layer upon a single light pulse with duration $t_{\text{ON}} = 300\ ms$.

The optical intensity measured in transmission is directly related to the induced birefringence, which serves as an indicator for the molecular ordering in the film.

The response can be divided into three main stages:

1. **Initial State (Disordered Phase):** Prior to stimulation, the PAZO molecules are randomly oriented within the film. In this isotropic state, no macroscopic birefringence is present and the transmitted intensity remains at its baseline level.
2. **Potentiation (Light-Induced Ordering):** Upon activation of the laser pulse, the polarized light interacts with the molecular chains of PAZO, inducing trans–cis isomerization and causing a reorientation of the molecules. This process leads to the

formation of a local anisotropy aligned perpendicularly to the polarization direction of the incident light. As a result, the optical signal increases rapidly, reaching a peak at the end of the stimulation window.

3. **Relaxation (Memory Effect or Full Recovery):** Once the light is turned off, the material undergoes spontaneous relaxation. The birefringence begins to decay as the molecules lose their ordered arrangement. Depending on the energy and duration of the stimulation, the system may:
    - Fully return to the disordered baseline (**STM**);
    - Stabilize in a partially ordered state, retaining a residual anisotropy (**LTM**).

When stimulated with light pulses of sufficient energy, the material shows a progressive increase in optical response (**potentiation**), followed by a spontaneous relaxation toward its initial state once the stimulation ends. The temporal evolution of this behavior depends strongly on stimulation parameters such as power density, pulse duration, number of pulses, and inter-pulse delay.

Effect of Power Density

The intensity of the stimulation light is a crucial factor in determining whether the induced molecular anisotropy will fully relax (**STM**) or partially persist (**LTM**). Figure 3.3 shows the dynamic optical response of PAZO to single light pulses of fixed duration ($t_{\mathrm{ON}} = 200$ ms) but with varying power densities.

At low power densities (e.g. $p = 8.3\ nW/\mu m^2$), the material exhibits a clear STM behavior: after the stimulation ends, the signal decays back to the initial baseline. As the power density increases, the peak intensity rises, and a residual intensity remains even minutes after the pulse, indicating the onset of LTM.
This transition reflects an higher efficiency in photoinduced molecular reorientation and stabilization mechanisms at higher energies.

Effect of Pulse Duration

Another key factor is the duration of the light pulse. In Figure 3.4, we present the dynamic response for different values of t_{ON}, keeping power density constant at $p = 8.3\ nW/\mu m^2$.

Shorter pulses ($t_{\mathrm{ON}} = 100 - 200\ ms$) lead to reversible responses (STM), where the birefringence vanishes completely within a few minutes.
In contrast, longer pulses ($t_{\mathrm{ON}} = 500\ ms - 1\ s$) generate a more stable molecular alignment that persists after the stimulus is removed, resulting in a long-term retention of anisotropy (LTM).

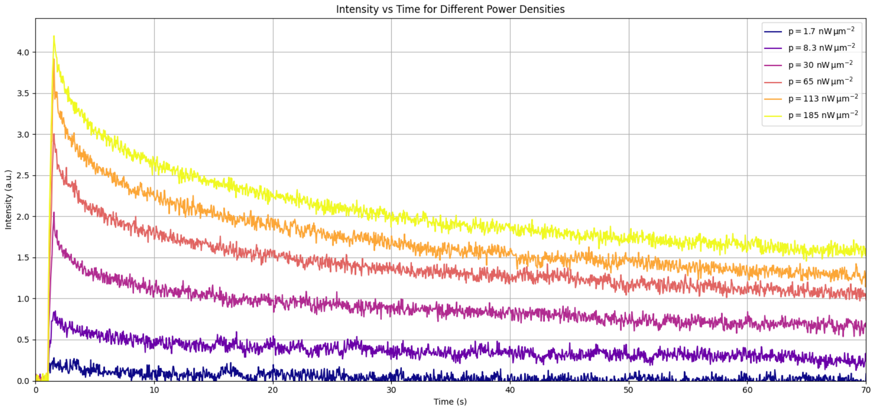

Figure 3.3: Transition from STM to LTM by increasing laser power density during a single pulse of fixed duration ($t_{\mathrm{ON}} = 200\ ms$)

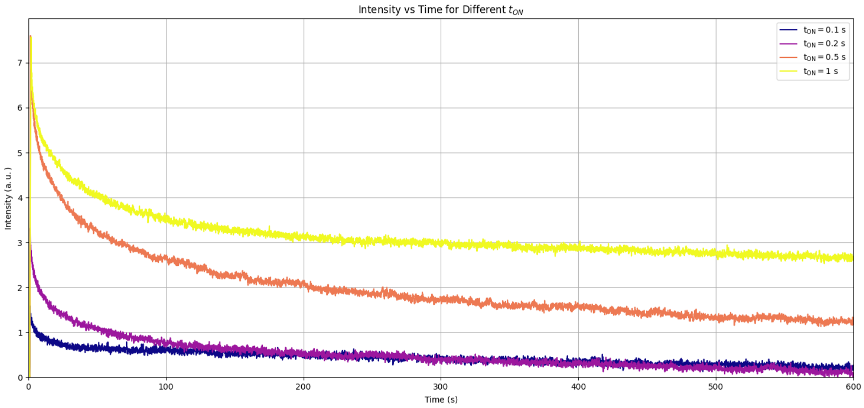

Figure 3.4: Evolution of the optical response as a function of pulse duration.

Effect of the Number of Pulses

The accumulation of multiple identical light pulses can also trigger the STM–LTM transition. Figure 3.5 illustrates the evolution of the optical response when the number of stimulation pulses increases (fixed $p = 8.3\ nW/\mu m^2$, $t_{\text{ON}} = 500\ ms$, $t_{\text{OFF}} = 500\ ms$).

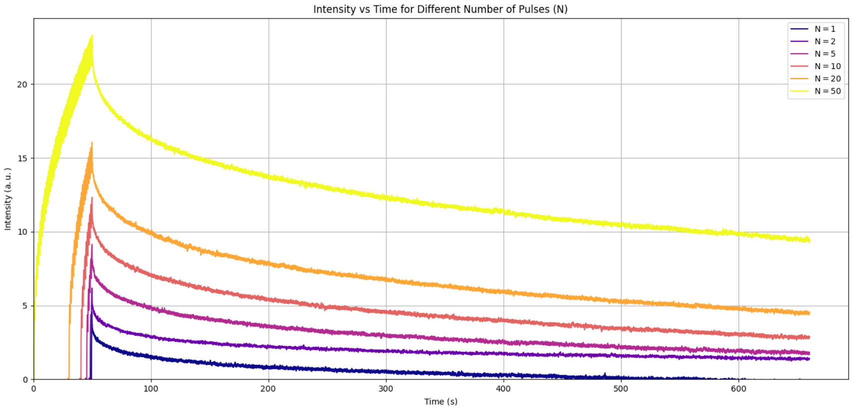

Figure 3.5: Progressive transition from STM to LTM by increasing the number of stimulation pulses

A single pulse results in a transient response (STM), while a sequence of $N = 16$ pulses progressively enhances the optical signal and leads to a residual intensity value, characteristic of LTM.
This effect mimics the cumulative behavior of biological synapses, where repeated stimulation strengthens the synaptic connection.

Effect of Inter-Pulse Delay

The temporal spacing between pulses plays a key role in determining how effectively the stimulus accumulates over time. As shown in Figure 3.6, when the time delay t_{OFF} between pulses is short (e.g. $200\ ms$), the system does not fully relax between successive pulses, allowing the anisotropy to build up and reach LTM.

On the contrary, when t_{OFF} increases (e.g. $10\ s$), the material has enough time to fully relax between each stimulation event, resulting in a reversible STM-like response. This behavior parallels the temporal correlation required in neural systems for efficient memory consolidation.

Temporal Correlation and Short-Term Facilitation

In addition to power and pulse accumulation, the degree of temporal correlation between stimulation pulses has a profound influence on the synaptic-like behavior of the system. In Figure 3.7, the PAZO film is stimulated with a sequence of 10 optical pulses

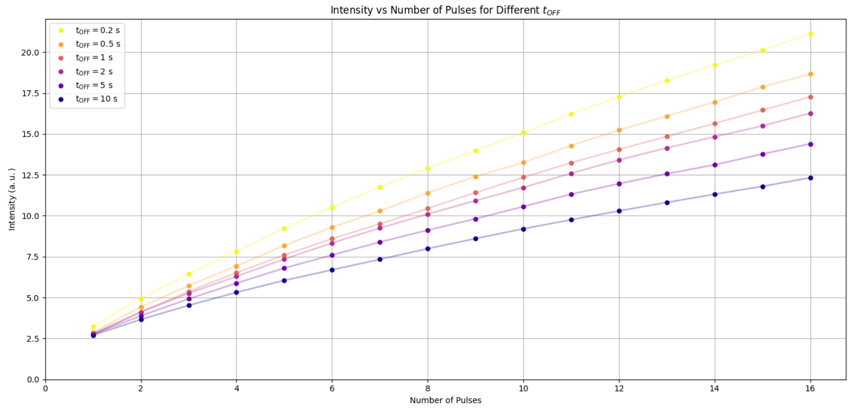

Figure 3.6: Influence of inter-pulse delay t_{OFF} on the potentiation behavior.

($p = 8.3\ nW/\mu m^2$, $t_{\mathrm{ON}} = 500\ ms$, $t_{\mathrm{OFF}} = 10\ s$), and the optical response is monitored over time.

Each stimulation event induces a partial potentiation, while the long delay between pulses allows the system to partially relax.
However, due to the incomplete recovery between closely spaced pulses, a progressive increase in the Post-Synaptic Intensity (PSI) is observed across the sequence. This behavior is a signature of *short-term synaptic facilitation*, where the cumulative effect results from the competition between photoinduced anisotropy and spontaneous relaxation.

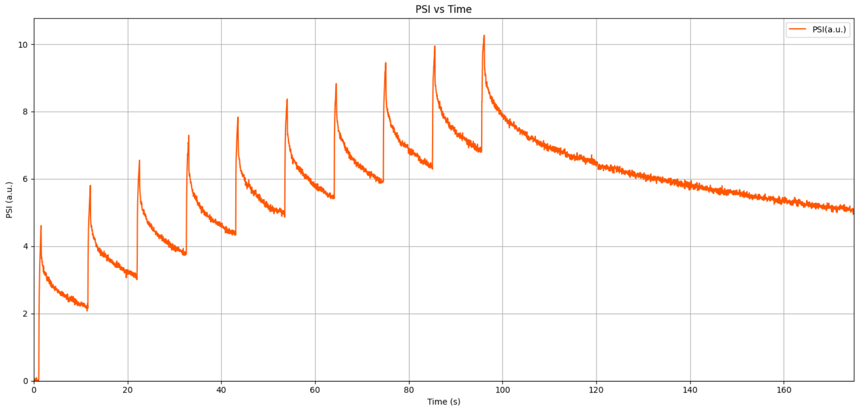

Figure 3.7: Dynamic response of the PAZO film to a train of 10 light pulses with $t_{\mathrm{ON}} = 500$ ms and $t_{\mathrm{OFF}} = 10$ s

To quantify this facilitation effect, we evaluate the *Pair Pulse Facilitation*(**PPF**) as the ratio between the detected peak intensity after the second pulse (A_2) and the first pulse (A_1), ($\mathrm{PPF} = A_2/A_1$).
As shown in Figure 3.8, the PPF index depends strongly on the inter-pulse delay t_{OFF}: for small delays (high temporal correlation), the second pulse builds on a non-relaxed

anisotropic state, leading to a significantly higher response. For longer delays, the system relaxes to its baseline before the second pulse, resulting in a PPF close to unity.

This behavior emulates the activity-dependent plasticity observed in biological systems, where temporally correlated signals lead to stronger synaptic reinforcement.

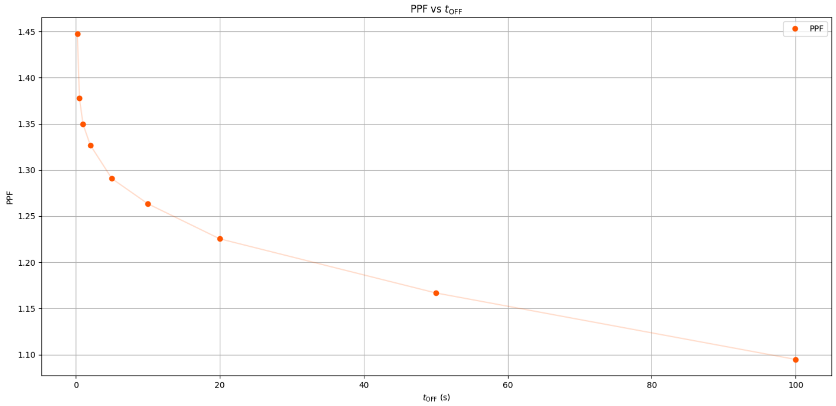

Figure 3.8: Pair Pulse Facilitation (PPF) as a function of the inter-pulse delay t_{OFF}

To visually demonstrate the transition from STM to LTM, I projected the PoliTO app logo (Figure 3.9) onto the PAZO film over a $100\ \mu m \times 100\ \mu m$ area with the **DMD** , using two different stimulation durations: 6 seconds and 30 seconds, with the same power density ($p = 8.7\ nW/\mu m^2$). Figure 3.10 present a time-lapse comparison of the optical response during the potentiation and following relaxation phases.

Figure 3.9: PoliTO app logo projected onto an uniform PAZO layer

In the case of short stimulation, after 5 minutes after the stimulation, the induced anisotropy decays rapidly, indicating a short-term retention of the pattern.
In contrast, prolonged stimulation results in a persistent birefringence that retains the projected image for a significantly longer time, consistent with long-term memory effects.

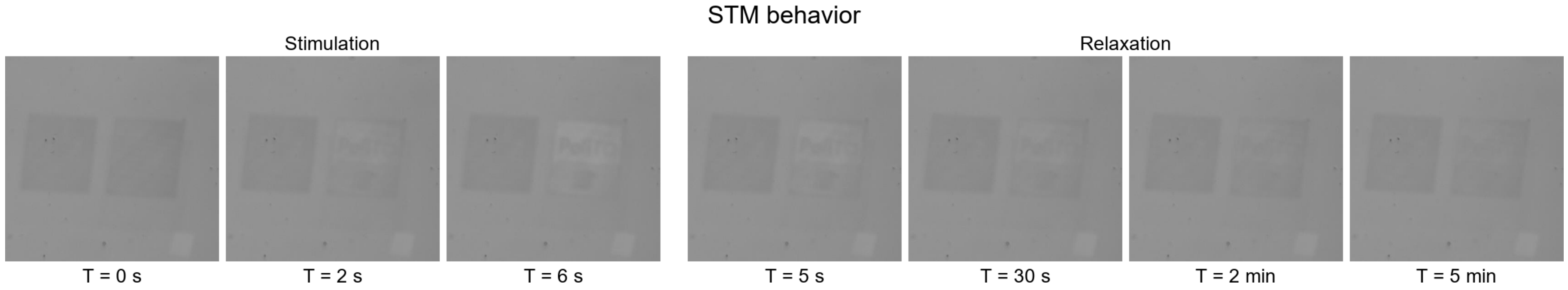

(a) **STM (**$30\ s$ **stimulation)**

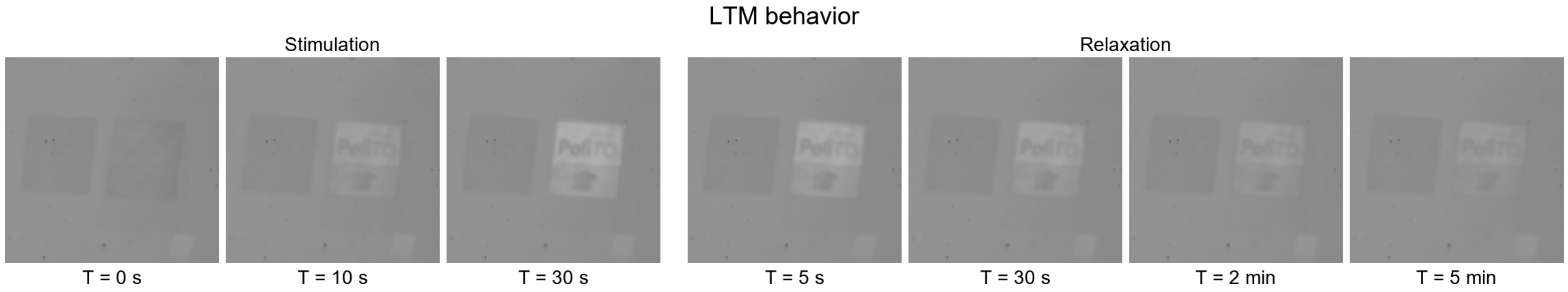

(b) **LTM (**$2\ min$ **stimulation)**

Figure 3.10: Comparison of image persistence in PAZO films after stimulation with different durations.

4 | Color Recognition

The aim of this chapter is to investigate whether the wavelength of the writing beam leaves a detectable signature in the relaxation dynamics of birefringence in a PAZO film.

The analysis focuses on the possibility that the decay of birefringence may retain a spectral dependency, potentially indicating a form of wavelength-specific memory effect in the material.

4.1 Laser Calibration and Experimental Design

To explore this effect, 2 modes of the MatchBox Laser were employed, emitting at $405\ nm$ (**violet**) and $520\ nm$ (**green**).

These two wavelengths were selected to probe different regions of the PAZO absorption spectrum, that are shown in Figure 4.1.

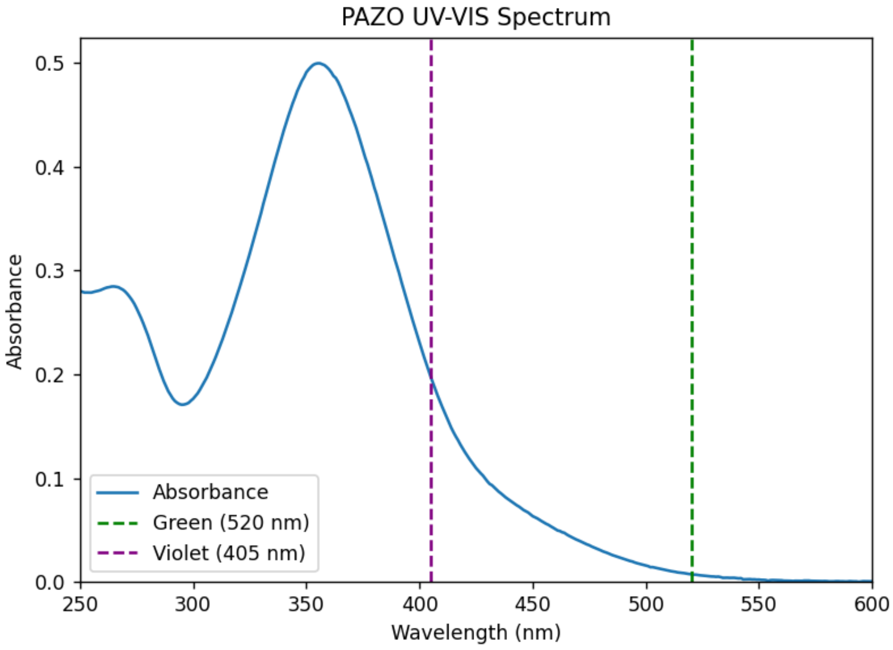

Figure 4.1: UV–vis absorption spectrum of PAZO

Before the optical stimulation tests, a full calibration of the laser output was performed. Since the device is controlled by a current driver, the power delivered at the sample surface is not directly known and must be determined experimentally.
For each wavelength, the optical power as a function of driving current was measured using a power meter right after the objective.
The resulting power–current (P–I) calibration curves provided the necessary reference for selecting stimulation levels with matched optical power (Figure 4.2).

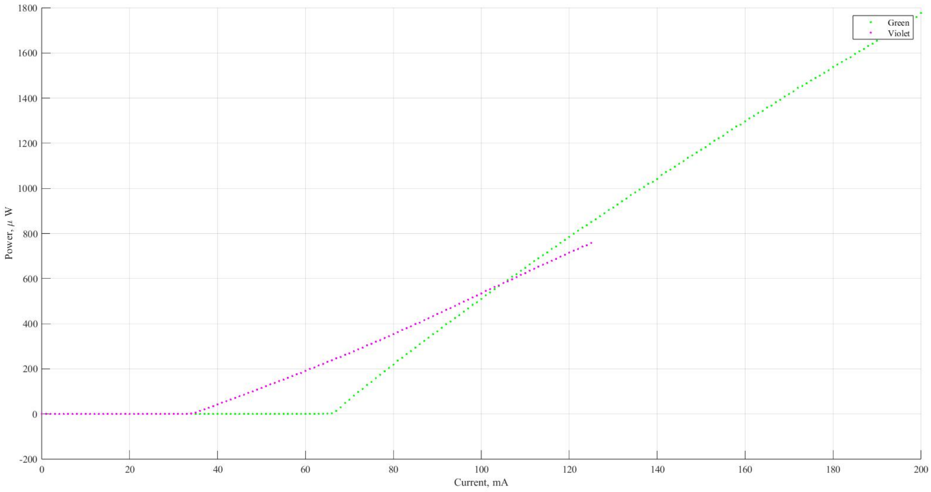

Figure 4.2: Power-Current laser calibration plot

In order to define a consistent set of stimulation parameters for both wavelengths, the following procedure was adopted: A minimum and maximum stimulation duration were fixed at $t_{\text{on}} = 0.5\ s$ and $t_{\text{on}} = 2\ s$ respectively.
For each wavelength, the maximum usable power (P_{max}) was determined as the highest power value just below the threshold for permanent migration under the longest stimulation time.
The minimum usable power (P_{min}) was chosen as the lowest power that produced a signal clearly above the noise floor for the shortest stimulation time.

To ensure a uniform and meaningful comparison between the two colors, a common dynamic range was established. The upper bound for power was defined as the minimum between the two P_{max} values, and the lower bound as the maximum between the two P_{min} values:

$$P_{\text{upper}} = \min(P_{\text{max}}^{\text{green}}, P_{\text{max}}^{\text{violet}}), \qquad P_{\text{lower}} = \max(P_{\text{min}}^{\text{green}}, P_{\text{min}}^{\text{violet}})$$

Within this common range, four power levels were selected using a uniform linear spacing that can be seen in Figure 4.3. The same approach was applied to the stimulation durations, resulting in four values for t_{on}: $0.5\ s$, $1.0\ s$, $1.5\ s$ and $2.0\ s$.

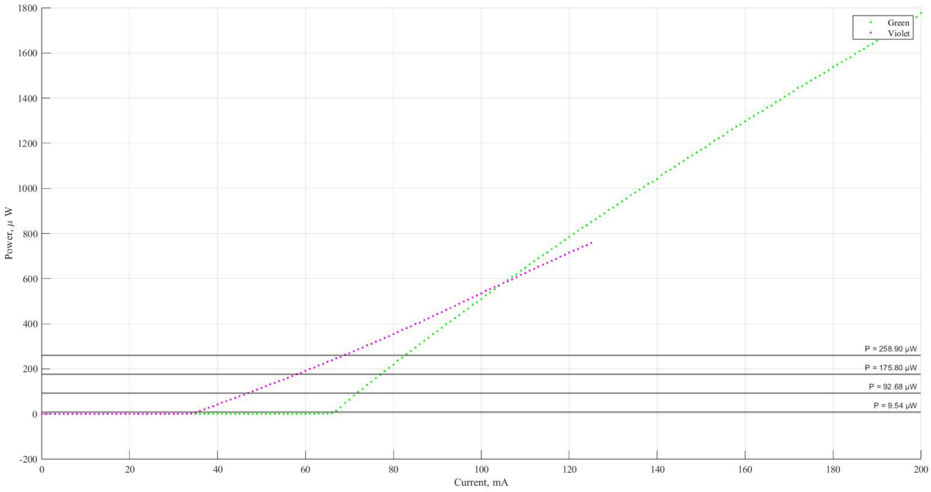

Figure 4.3: Calibration plot with the four equally spaced powers

Due to the discrete nature of the laser current control, the exact power values corresponding to the uniformly spaced levels could not always be achieved.
Therefore, for each selected target power, the closest available value for both green and violet lasers was chosen, ensuring approximate matching between the two colors.

The final set of power levels used in the experiments is reported in Table 4.1, along with the common set of stimulation durations.

Stimulation Level	**Violet Power [μW]**	**Green Power [μW]**	**Violet Power Density [nW/μm^2]**	**Green Power Density [nW/μm^2]**
1	13.8	14.19	8.04	8.26
2	93.6	97.0	54.49	56.47
3	176.0	174.0	102.48	101.32
4	263.0	266.0	153.22	154.89

Table 4.1: Optical powers and corresponding power densities for green and violet laser sources at each stimulation level. The illuminated area is $1.7174 \times 10^3\ \mu\text{m}^2$.

Stimulation Duration [t_{on}] (s)
0.5
1.0
1.5
2.0

Table 4.2: Stimulation durations used for both green and violet laser experiments.

The temporal dynamics of light-induced birefringence in azobenzene-containing PAZO films can be effectively modeled using a bi-exponential approach. This choice is supported by experimental evidence that both the induction and the relaxation of birefringence involve two distinct processes: a fast response associated with the reorientation of azobenzene groups, and a slower response related to polymer chain interactions and structural constraints[11].

To quantitatively describe these dynamics and extract significant markers from them, a phenomenological model has been used in which the recorded light intensity signals $I(t)$ from the colored stimulations are fitted using a double exponential function for both the potentiation (Equation 4.1) and relaxation(Equation 4.2) regimes.

$$I(t) = I_{\text{sat}} \left(1 - Ae^{-t/\tau_a} - Be^{-t/\tau_b}\right) \tag{4.1}$$

$$I(t) = Ce^{-t/\tau_c} + De^{-t/\tau_d} \tag{4.2}$$

In Equation 4.1, I_{sat} is the saturation intensity, while A and B are weighting factors associated with the fast (τ_a) and slow (τ_b) activation processes.
In Equation 4.2, the constants C and D represent the contributions of two independent relaxation mechanisms, governed by the respective time constants τ_c and τ_d.

4.2 Analysis of Spectral Dependency in Relaxation Dynamics

To assess whether the relaxation dynamics of birefringence in PAZO films depends on the wavelength of the writing light, a set of measurements was acquired for both the green ($520\ nm$) and violet ($405\ nm$) mode, across the full grid of stimulation conditions defined in the previous section.

For each stimulation condition, the transmitted intensity was recorded for a duration sufficient to fully capture both the build-up and the decay of the photoinduced birefringence ($t_{\text{relax}} = 5\ min$).
The resulting temporal profiles exhibit a characteristic growth followed by a slower relaxation, which were analyzed using the bi-exponential model described in equations (4.1) and (4.2).

The experimental curves, along with their corresponding fits, are shown in a set of composite figures (Figure 4.4, Figure 4.5, Figure 4.6, Figure 4.7).
Each of the four main figures corresponds to one of the selected stimulation power levels and includes four subplots representing the different exposure times (t_{on}).
Within each subplot, the measured relaxation signals and fitted curves are presented for

---

[11] Carla Madruga et al. , **519**: 8191–8196, 2011.

both green and violet stimulation under identical conditions.

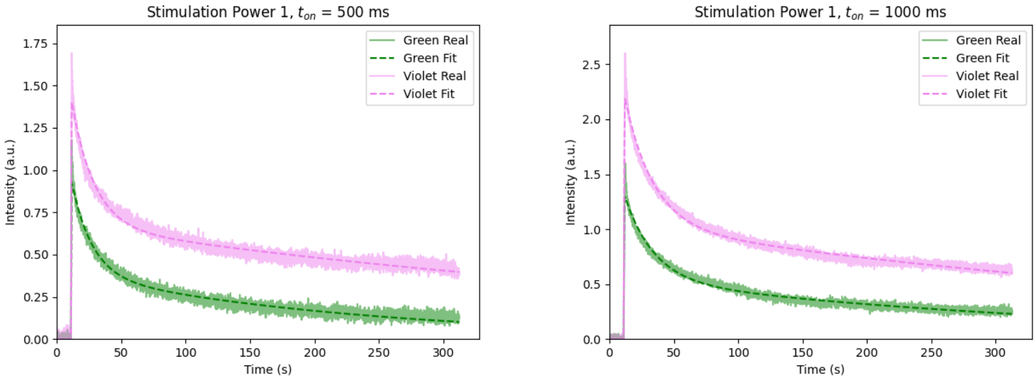

(a) $t_{\text{on}} = 0.5$ s

(b) $t_{\text{on}} = 1.0$ s

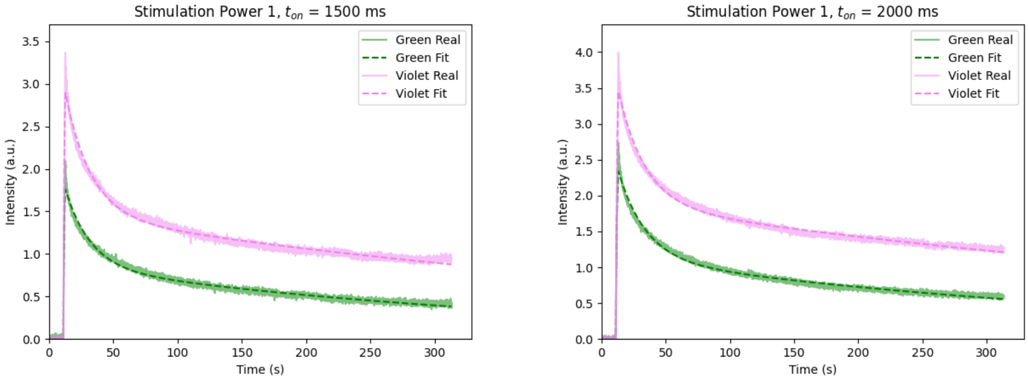

(c) $t_{\text{on}} = 1.5$ s

(d) $t_{\text{on}} = 2.0$ s

Figure 4.4: Relaxation curves and corresponding fits for green and violet stimulation at power level 1, shown across the four stimulation times t_{on}

A qualitative inspection of the relaxation curves reveals a consistent trend: under equivalent stimulation conditions (i.e. fixed power and exposure time), the signals obtained from violet light stimulation exhibit a greater amplitude than those induced by green light. This behavior is in agreement with the optical absorption spectrum of PAZO, which shows a stronger absorbance at $405\ nm$ compared to $520\ nm$.

Regarding the fitted models, the bi-exponential relaxation function generally provides a good representation of the overall decay dynamics. However, some limitations are observed in regions where the signal undergoes rapid changes, particularly immediately after the stimulus is turned on or off.
In these transient regions, the recorded experimental data may change more quickly than the temporal resolution of the acquisition allows. Since the sampling interval is fixed at $50\ ms$, this imposes a constraint on the model's ability to capture fast transitions with high

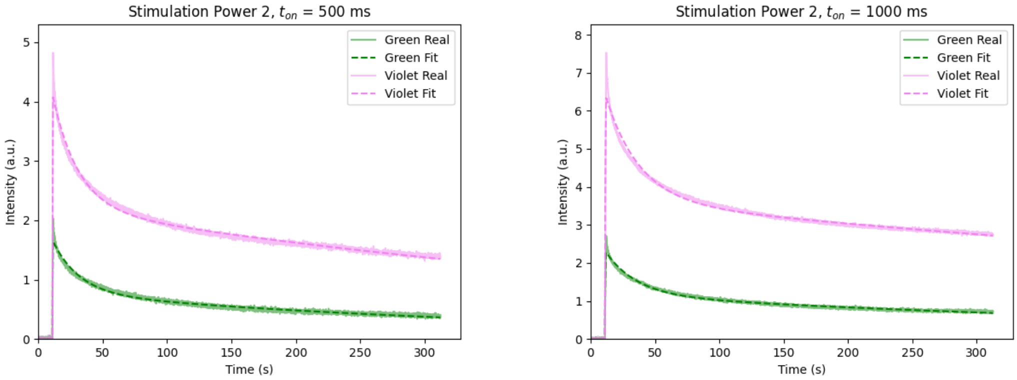

(a) $t_{\text{on}} = 0.5$ s (b) $t_{\text{on}} = 1.0$ s

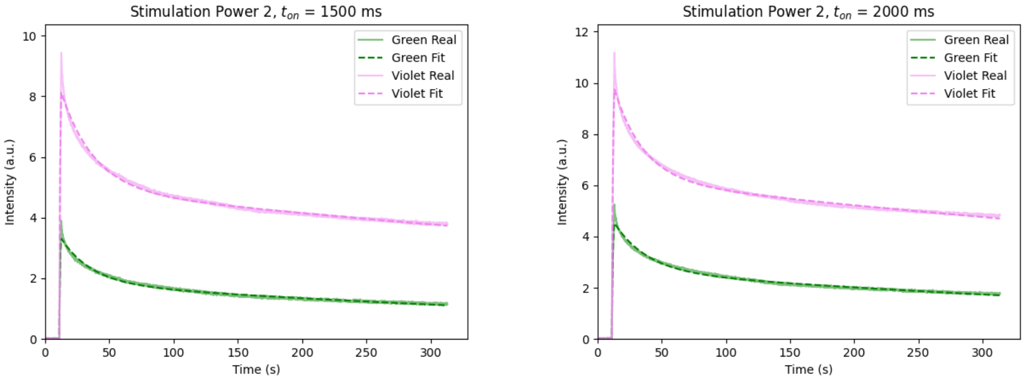

(c) $t_{\text{on}} = 1.5$ s (d) $t_{\text{on}} = 2.0$ s

Figure 4.5: Relaxation curves and corresponding fits at power level 2. Each subplot shows both green and violet responses for a fixed exposure time.

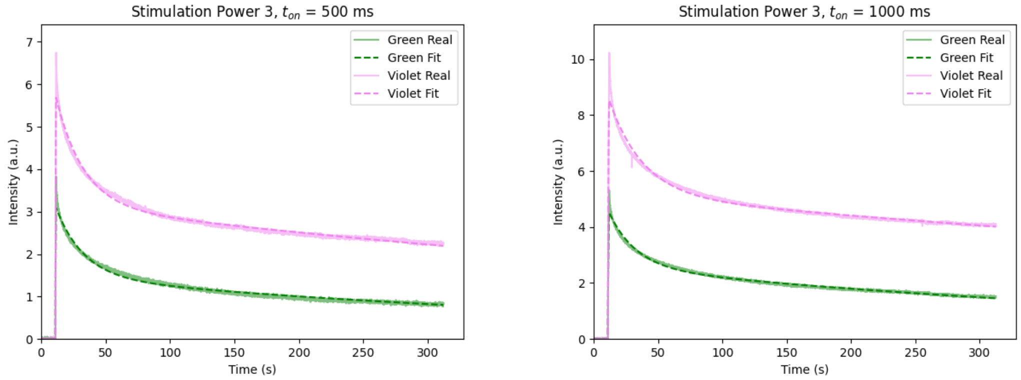

(a) $t_{\mathrm{on}} = 0.5$ s

(b) $t_{\mathrm{on}} = 1.0$ s

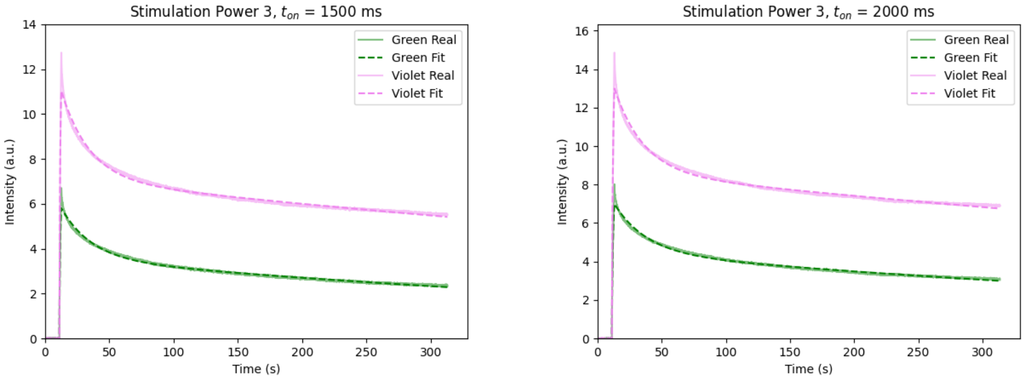

(c) $t_{\mathrm{on}} = 1.5$ s

(d) $t_{\mathrm{on}} = 2.0$ s

Figure 4.6: Relaxation dynamics for power level 3, shown across the four stimulation times t_{on}

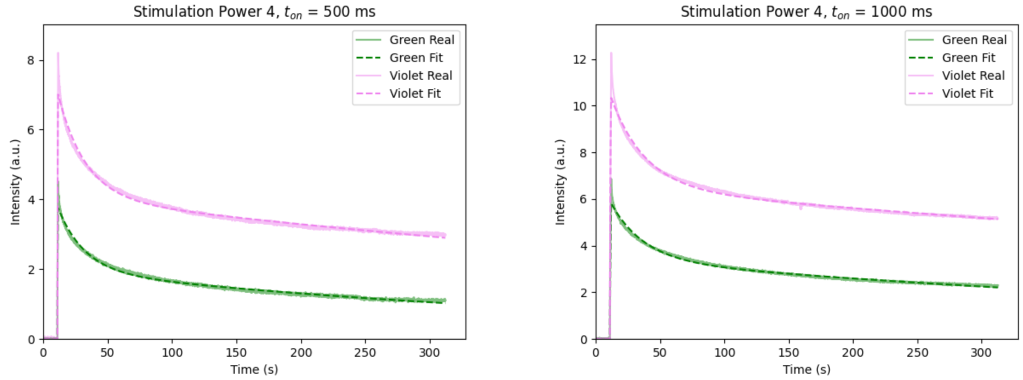

(a) $t_{\mathrm{on}} = 0.5$ s (b) $t_{\mathrm{on}} = 1.0$ s

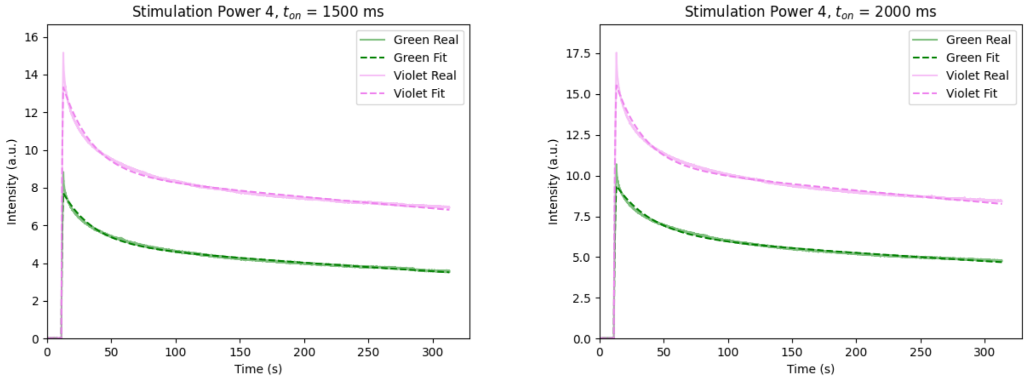

(c) $t_{\mathrm{on}} = 1.5$ s (d) $t_{\mathrm{on}} = 2.0$ s

Figure 4.7: Fitted and experimental relaxation curves at power level 4, shown across the four stimulation times t_{on}

accuracy.

Analysis of the fitted parameters revealed that the short relaxation constant τ_c does not exhibit consistent separation between the two wavelengths: across all combinations of P and t_{on}, the values of τ_c for green and violet overlap significantly, suggesting that this timescale is not strongly wavelength-dependent.

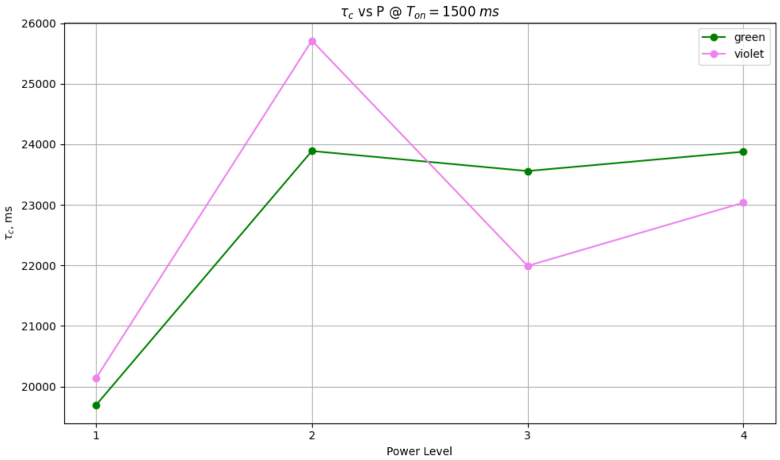

Figure 4.8: Example of the fitted τ_c values at the four power levels for $t_{on} = 1500\ ms$

The long relaxation time constants τ_d are shown in Figure 4.9 and Figure 4.10 in two complementary ways. In the first representation (Figure 4.9), τ_d is shown as a function of stimulation power for each fixed stimulation time. In the second representation (Figure 4.10), τ_d is plotted as a function of stimulation time for each fixed power level.

Looking at both the representations, it seems that τ_d displays a more robust spectral dependency than τ_c. For a subset of stimulation conditions, the fitted values of τ_d for violet stimulation consistently exceeded the corresponding values for green. This observation suggests the existence of a spectral memory effect that manifests on the slow relaxation timescale.

To better investigate its behavior τ_d was plotted across the entire $(P,\ t_{\text{on}})$ parameter space for both wavelengths.
In Figure 4.11, the fitted values of τ_d are shown in the z axis as a function of power and exposure time.

To explore the conditions under which τ_d can be always differentiated between the two wavelengths, a comparison threshold was introduced:

$$\tau_d^{\text{violet}} > \max\left(\tau_d^{\text{green}}\right)$$

This condition was evaluated point-by-point across the entire $(P,\ t_{\text{on}})$ parameter space.

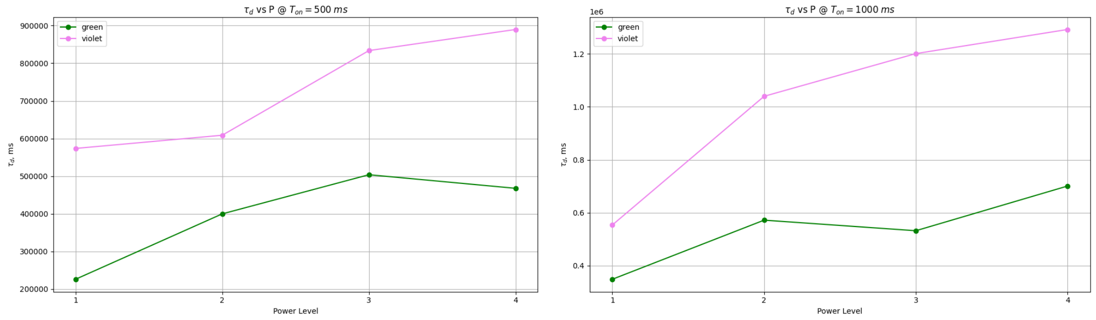

(a) $t_{\text{on}} = 0.5$ s (b) $t_{\text{on}} = 1.0$ s

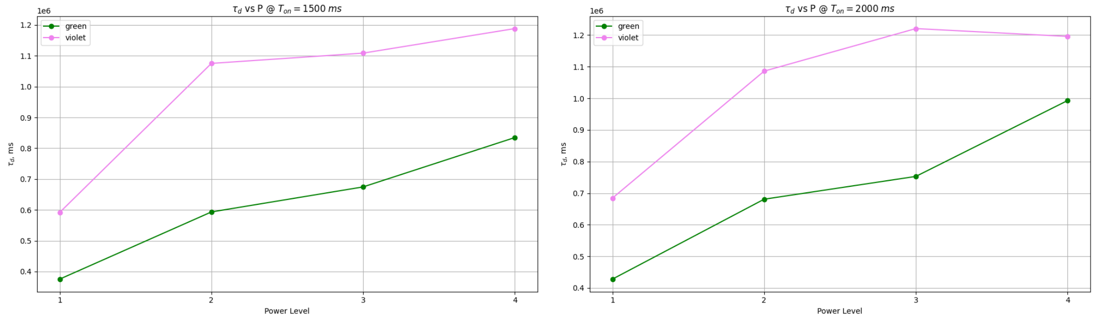

(c) $t_{\text{on}} = 1.5$ s (d) $t_{\text{on}} = 2.0$ s

Figure 4.9: Fitted τ_d values for green and violet stimulation at the four power levels, for a fixed stimulation time t_{on}

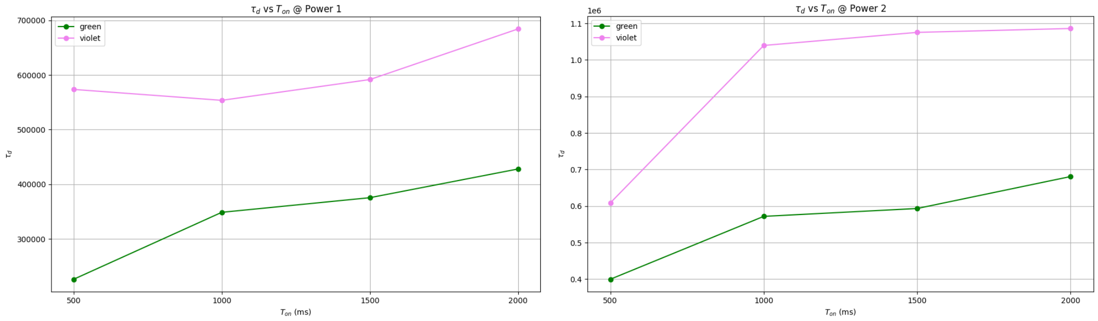

(a) Power level 1 (b) Power level 2

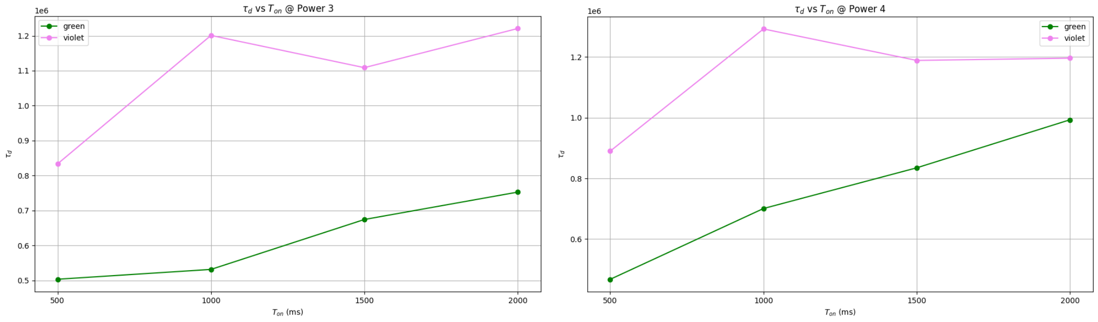

(c) Power level 3 (d) Power level 4

Figure 4.10: Fitted τ_d values for green and violet stimulation at the four stimulation time, for a fixed power level

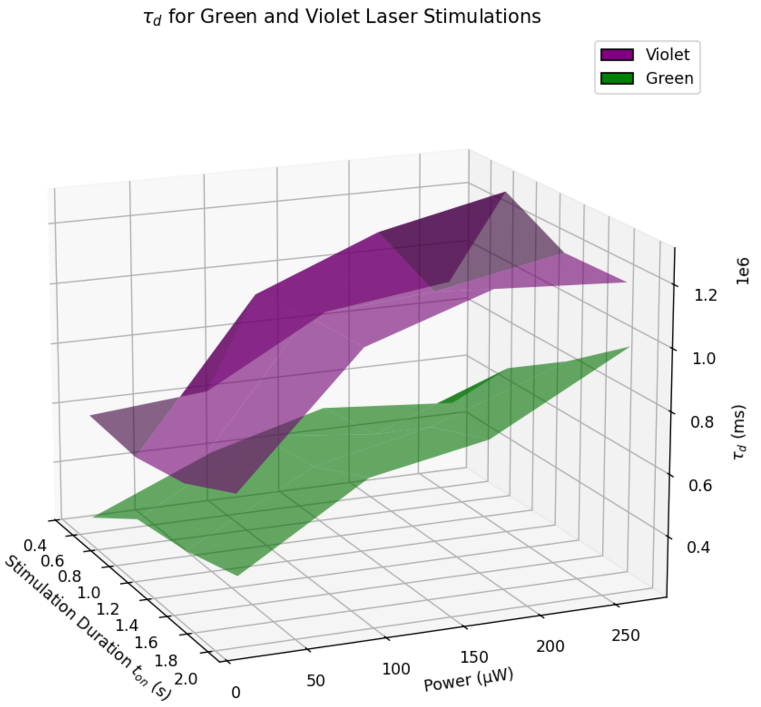

Figure 4.11: Fitted τ_d values for violet and green stimulation, shown across the $(P,\ t_{\text{on}})$ parameter space. Surfaces indicate interpolated values for each color

In Figure 4.12, the two fitted τ_d surfaces, corresponding to green and violet illumination, are shown along with a horizontal plane representing $\max\left(\tau_d^{\text{green}}\right)$. This visualization allows direct identification of the portion of the violet surface that lies entirely above the threshold plane, thus satisfying the condition for spectral separation.

To better interpret this result, the violet surface was projected onto a two-dimensional map in the $(t_{\text{on}},\ P)$ plane.
In Figure 4.13, each stimulation condition is represented by a cross at its corresponding coordinates. The color of the background indicates whether the spectral separation condition is satisfied.

From this representation, a well-defined region emerges: for stimulation durations $t_{\text{on}} \geq 1.0\ \text{s}$ and $P \geq 93\ \mu W$ (corresponding to a power density $p \geq 54.5\ nW/\mu m^2$), all the violet τ_d values lie above the maximum τ_d obtained from green stimulation. This suggests that in this upper region of the stimulation space, τ_d becomes independent of the specific stimulation conditions and exhibits a specific spectral signature.

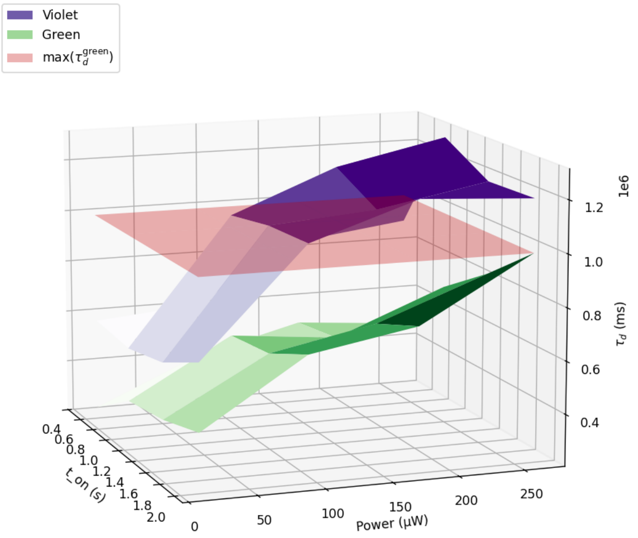

Figure 4.12: 3D plot showing τ_d surfaces for green and violet light, along with a horizontal plane at $\max(\tau_d^{\text{green}})$. Regions of the violet surface that intersect or rise above this plane satisfy the spectral discrimination condition

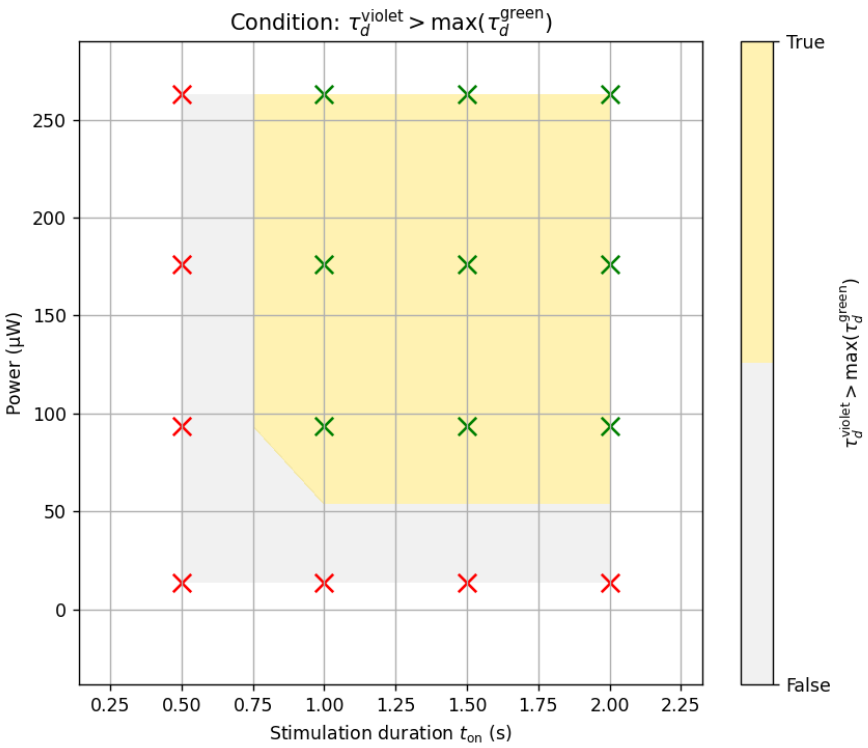

Figure 4.13: 2D projection of the violet τ_d surface with superimposed stimulation grid. Crosses indicate tested combinations of t_{on} and P

5 | Luminance Adaptation

5.1 Preliminar study on uniform PAZO layers

From the previously found equation 3.8 of the transmitted intensity through a fixed layer of PAZO it can be seen that the layer thickness d plays a role in determining the intensity variation.

Other than this, the thickness d is also nested in the birefrigence term Δn.

The works from Nedelchev et al. [9,49] explore the relations between the build-up of the birefringence and the layer thickness d.

Their conclusions are that there is a saturation value Δn_{max} for the birefringence that is reached for sufficiently long stimulations that however does not depend significantly on the thickness, but this latter influences the response time τ defined in [49] as the recording time needed to reach 80% of the maximal birefringence.

This influence allows to think that the thickness can be controlled and adjusted to obtain different dynamical responses from this material.

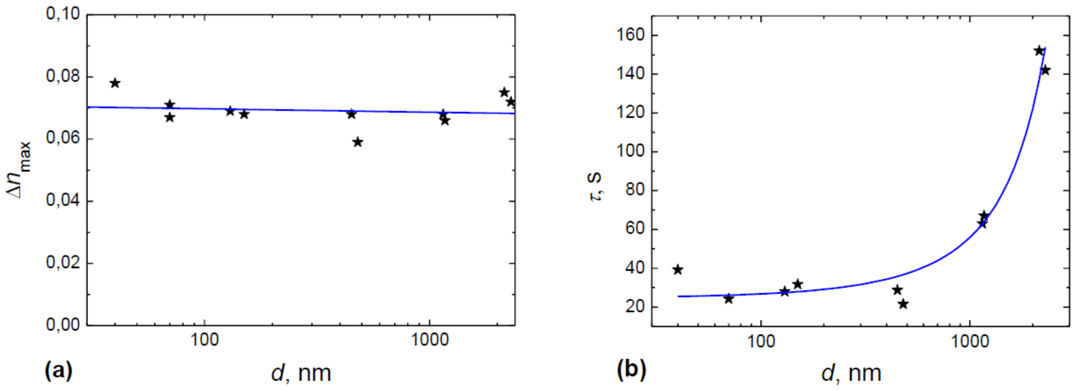

Figure 5.1: Influence of the film thickness d on a) the maximal value of birefrigence Δn_{max} and b) the time response τ (From [9])

To understand experimentally how the thickness plays a role in changing the dynamic

---

[9] Lian Nedelchev et al. “Birefringence induced in azopolymer (PAZO) films with different thickness” in: *18th International School on Quantum Electronics: Laser Physics and Applications*. ed. by Tanja Dreischuh, Sanka Gateva, and Alexandros Serafetinides vol. 9447 SPIE, Jan. 2015. 94471I DOI: `10.1117/12.2176158`

[49] Lian Nedelchev et al. , **376**: 1–6, 2019.

response of our system, I started by fabricating samples of different thicknesses to then record their responses.

5.1.1 Fabrication

To realize these samples two solutions of PAZO were prepared by dissolving the solid polymer in methanol at concentrations of $50\ mg/mL$ and $100\ mg/mL$ respectively.
To get sure that the polymer was well dissolved into the solution mechanical stirring and sonication at $60°C$ were performed for 90 minutes.
Prior to deposition, all glass substrates were treated with oxygen plasma (10 minutes, 130 W) to promote adhesion and improve surface wettability.
The $50\ mg/mL$ PAZO solution was deposited via spin coating on three different glass substrates, each at a distinct spin speed to modulate film thickness.

It can be noticed, looking at these three samples, that to get thicker layers conversely the thickness uniformity gets worse because of the reduced RPM used in spinning and the fast evaporation of the solvent. So, for each solution concentration, there is a constraint on the maximum thickness obtainable.
To get a thicker layer the $100\ mg/mL$ solution was used, always through spin coating on another substrate.
Finally to get the thickest sample and to overcome the limitation of the spin coating the final sample was prepared by drop-casting the $100\ mg/mL$ solution directly onto the substrate surface. In this way, despite having a great non-uniformity in the thickness over the whole sample, a small region with a thickness of $2\ \mu m$ has been obtained.
All the samples are then dried on an hot plate at $60°C$ for 1 hour to be sure that all the solvent is evaporated.

In the table 5.1 the information about the spinned samples are presented. The thickness were measured along a scratch made on the samples by means of an optical profilometer with a 5X objective and the surface maps can be seen in Figure 5.2.

ID	Conc. (mg/mL)	Solvent	Vol. (μL)	RPM	Acc.	Time (s)	Thickness (nm)
SP01	50	Methanol	100	1200	750	30	360
SP02	50	Methanol	100	1200	750	30	480
SP03	50	Methanol	100	800	750	30	650
SP04	100	Methanol	150	800	750	60	1000
D01	100	Methanol	150	-	-	-	2000

Table 5.1: Spin-coating (and drop-coating for **D01**) parameters and resulting thicknesses of PAZO films.

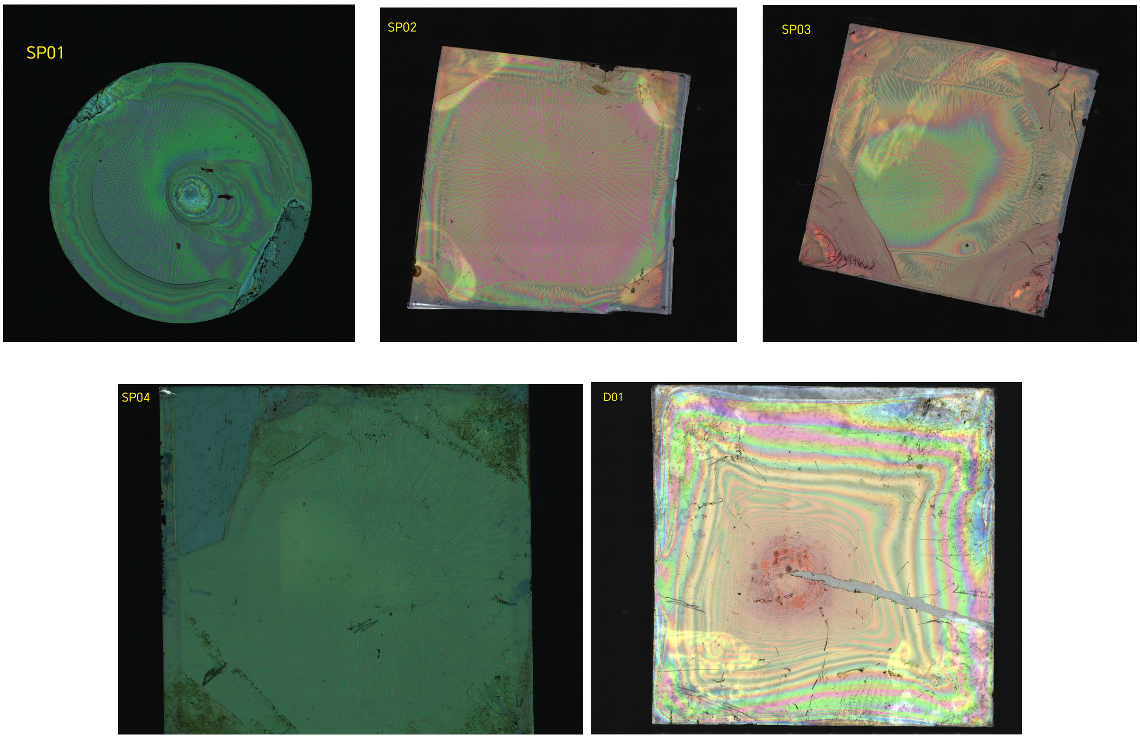

Figure 5.2: Maps of PAZO-coated samples with different thicknesses obtained through an optical profilometer with a 5X objective

5.1.2 Dynamic responses

The results from a stimulation for $200\ ms$ with a power density of x are shown in Figure 5.3.

It is clearly visible a trend for the growth rate, in fact starting from their initial intensity value (the curves have been baseline-corrected to enable a clear comparison), after the $200\ ms$ of stimulation the maximum reached amplitude increases with the thickness: The

Thickness (μm)	Maximum Intensity
0.36	1.380
0.48	1.551
0.60	1.550
1.00	2.254
2.00	5.720

Table 5.2: Maximum intensities for each sample thickness.

small differences or apparent inaccuracies in the maximum intensity values observed for samples with similar thicknesses ($< 200\ nm$) can be attributed to the sampling rate of the camera. Since the camera acquires data every $50\ ms$, it is possible that the true peak intensity was not captured, resulting in a slightly underestimated maximum.

While for thinner samples (**SP01**, **SP02**, **SP03**) the dynamics are very similar, the differences are more visible when thick samples are compared (**SP04**, **D01**).

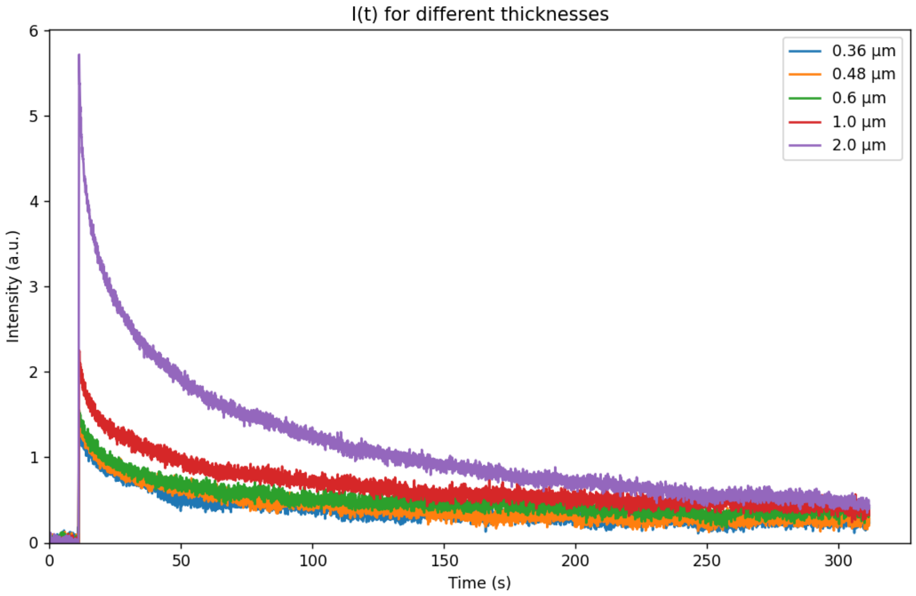

Figure 5.3: Dynamic response of the five samples with $200\ ms$ of stimulation

Summarizing, the observations from this comparison are:

- The growth rate well correlates with the thickness increase.
- The difference in potentiation between the thicker samples ($\geq\ 1\mu m$) gets bigger with respect to the thinner ones.

The hypotheses arising from these observations, which I have explored in this work, are as follows:

- If it were possible to fabricate structures with varying thicknesses on a single sample, one could potentially exploit their thickness-dependent response to extend the usable dynamic range of the material.
- Specifically, by designing a pixelated structure where two pillars of different heights coexist within the same spatial region, it would be possible to extract information from either the taller or the shorter pillar, depending on which one provides a more optimal response to the stimulus.
  - In low-power and/or short-durations, the shorter pillars may fail to respond or fall below the noise threshold, whereas the taller pillars (characterized by a faster response) could still yield meaningful information.
  - Conversely, under high-power and/or long-duration stimulation, the taller pillars may saturate due to the limitations of the recording setup, while the slower-responding shorter pillars could still provide usable signal.

5.2 Study on micro-structured PAZO

5.2.1 Fabrication and characterization

To realize PAZO samples with varying thickness on the same substrate I opted for a novel approach consisting in:

- The fabrication of the master with the *grayscale lithography*
- The transferring of the pattern negative on an elastomeric mold (**PDMS**)
- The actual molding of a PAZO layer through *soft-lithography* techniques

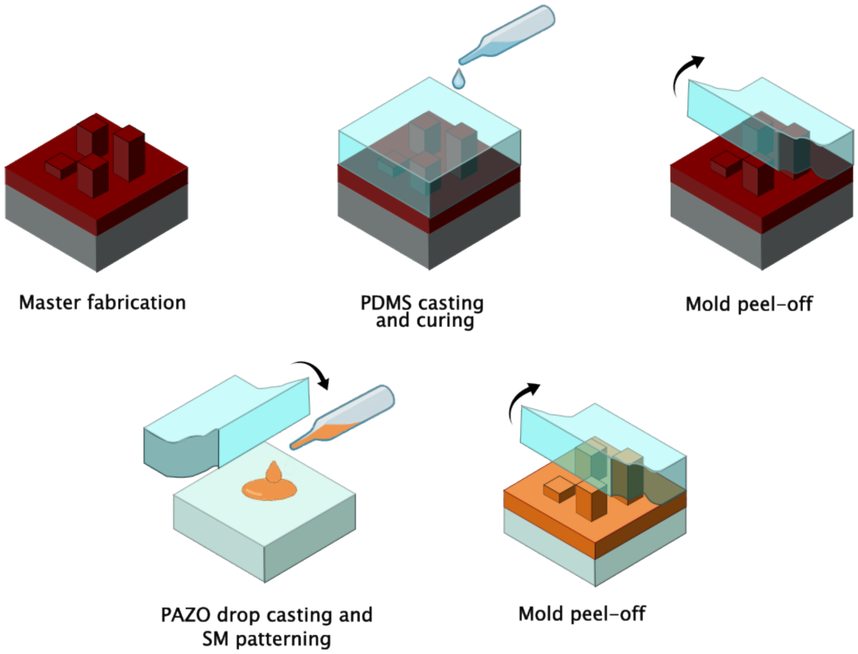

Figure 5.4: Summary illustration of the main PAZO microstructuring steps

Grayscale Lithography

As stated in section 2.1.2, the grayscale technique allows to create, on the same exposed sample, non-uniform topographies by modulating the exposure dose given to it.

For this thesis, I used the Heidelberg Instruments Micro Pattern Generator μPG 101, which enables grayscale lithography by modulating the exposure dose through an RGB color map.

Specifically, the system varies the exposure time assigned to each pixel based on its grayscale level: a pixel with RGB values set to $(0, 0, 0)$ receives 0% of the maximum exposure time, while a pixel with RGB values set to $(100, 100, 100)$ receives 100% of the maximum exposure time.

Intermediate values are interpreted linearly, so that the RGB intensity (ranging from 0 to 100) corresponds proportionally to the relative exposure time.

The minimum lateral resolution of the system is $400\,nm$ per pixel.

The pattern generator creates a virtual mask from a 2D design in which each region is assigned a specific grayscale value corresponding to a desired resist thickness. The exposure is then performed in stripes with a laser operating at constant power. The spatial variation in dose, and thus in the final resist height, is achieved by modulating only the exposure time according to the grayscale level of each pixel.

In principle this approach would enable the fabrication of resist structures with continuous and linear thickness gradients across the sample, from the maximum height of the photoresist, down to the bare silicon oxide substrate on which the resist is spin-coated (Figure 5.5).

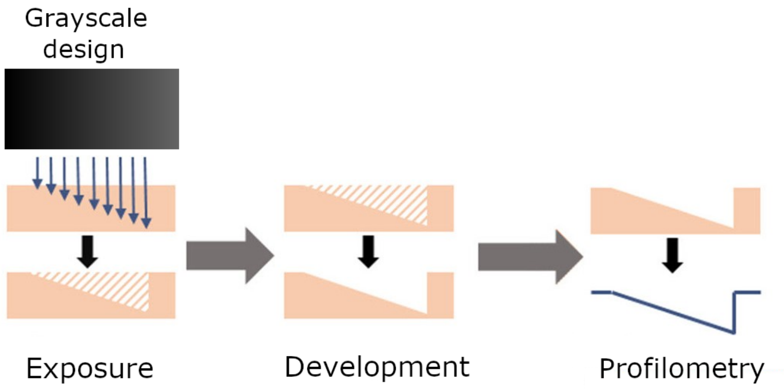

Figure 5.5: Typical grayscale lithography procedure, from the realization of the 2D design to the characterization through optical profilometry (Modified from [50]

In practice, however, achieving a perfectly linear profile with a one-to-one correspondence between RGB values and final resist thickness is not straightforward. Several factors can affect this ideal relationship:

- The photoresist response itself is inherently nonlinear: a unit change in grayscale level (e.g., a change of $\Delta\texttt{RGB} = 1$) does not necessarily produce a uniform change in the exposed thickness (Δd). This nonlinearity arises from the complex interaction between exposure dose, resist contrast, and post-exposure processing.
- It is often challenging (sometimes impossible) to define a single set of optimal exposure parameters (such as exposition power and development time conditions) that ensures a consistent mapping from grayscale level to resist height across the entire sample. As a result, different grayscale levels may not correspond reliably to distinct thicknesses, especially near the extremes of the exposure window.

In the following, I present some of the several test samples fabricated, using the protocol in table Table 5.3, with modifications on the used exposition power and development time.

Step	Description
1	Design of the grayscale CAD mask, where each region is assigned a gray level (RGB value) corresponding to the desired local resist thickness after development.
2	Cleaning of the silicon oxide substrate by sonication in acetone for 5 minutes at 40°C, followed by nitrogen drying.
3	Spin-coating of ma-P 1275 G positive resist at 3000 RPM for 30 seconds to obtain a $9.5\ \mu m$ thick layer ($\pm 0.5\ \mu m$), measured by profilometry across a scratch.
4	Soft bake on a hot plate at 100°C for 10 minutes.
5	Grayscale exposure performed with varying exposition power, where the exposure dose is modulated according to the grayscale level of the CAD design.
6	Development in mr-D 526/S developer, with development times adjusted depending on the exposure dose.

Table 5.3: Grayscale lithography processing steps using ma-P 1275 G positive resist.

To evaluate the behavior and quality of the grayscale lithography process, a test pattern was created using a 2D image editor (GIMP) (Figure 5.6), where the design was drawn in 8-bit grayscale (RGB values from 0 to 100). The layout was subdivided into four distinct regions, each targeting a specific characterization aspect of the resist response:

- **Bottom-left quadrant:** an array of square pillar structures where the grayscale level increases gradually from RGB 0 to RGB 100, both horizontally (left to right) and vertically (top to bottom). This area allows observation of thickness gradients in both directions and a correspondence one-to-one between RGB and single pillar thickness.

- **Bottom-right quadrant:** a series of grayscale ramps with a linear gradient in one direction. These ramps serve as a visual indicator to evaluate the linearity of the resist's thickness response with respect to the exposure dose (i.e. RGB value).

- **Top-right quadrant:** an array of rectangular pads with varying surface areas but fixed grayscale increments (steps of 10 RGB units).
  This section was designed to assess the resolution and uniformity of the grayscale process across different feature sizes.

- **Top-left quadrant:** a set of concave and convex lens-shaped surface profiles. These were generated using varying circular grayscale gradients to study the ability of the system to produce continuous topographies and to observe the resist's behavior in curved regions.

A series of tests were conducted on the grayscale pattern described above, with the aim of

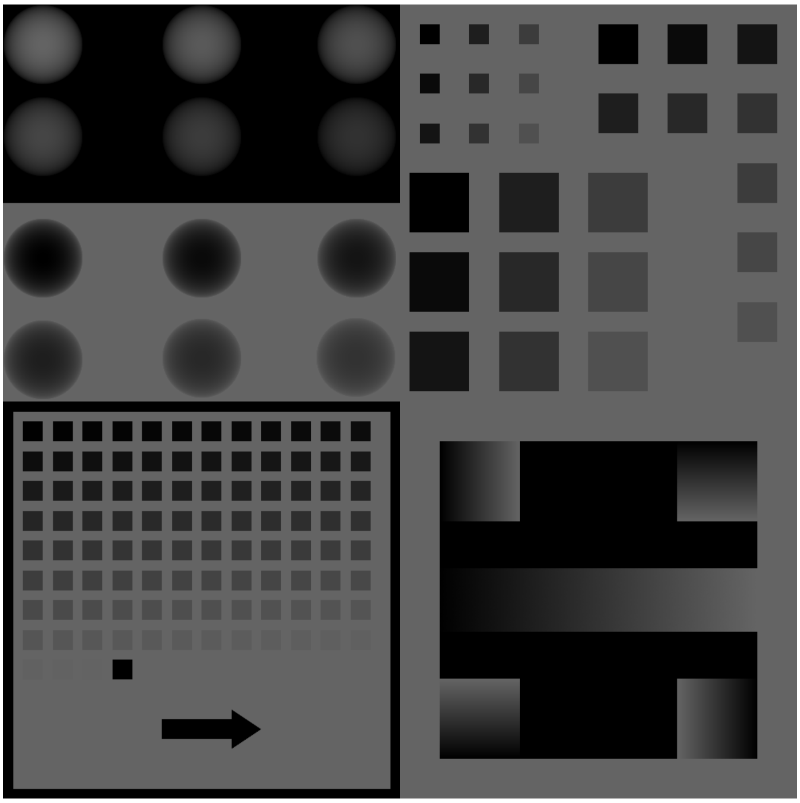

Figure 5.6: Grayscale test pattern design

identifying optimal exposure power and development time to achieve a complete grayscale range.

In the first attempt (**M01**), the sample was exposed with a power of $8\ mW$ and developed until the substrate surface became visible (i.e. until the region corresponding to RGB = 100 was fully cleared).
However, I observed that more than half of the grayscale levels were removed during development, indicating severe erosion. Only approximately 40 grayscale levels remained visible after a total development time of 5 minutes.

In the second test (**M02**), the exposure power was reduced to $4\ mW$, keeping the same development strategy.
The substrate became visible after around 5 minutes and 30 seconds of development. This time, more than 50 grayscale levels remained, confirming that a lower exposure power preserved a larger portion of the grayscale structure. However, signs of partial erosion were still present in some features, especially in the regions with lower RGB values suggesting an overdevelompent.

In the final test (**M03**), the exposure power was further reduced to **1 mW**. To fully develop the RGB = 100 region, a much longer development time (around 8 minutes and 30 seconds) was required.
Although approximately 70 grayscale levels were still visible, an analysis of the ramp pro-

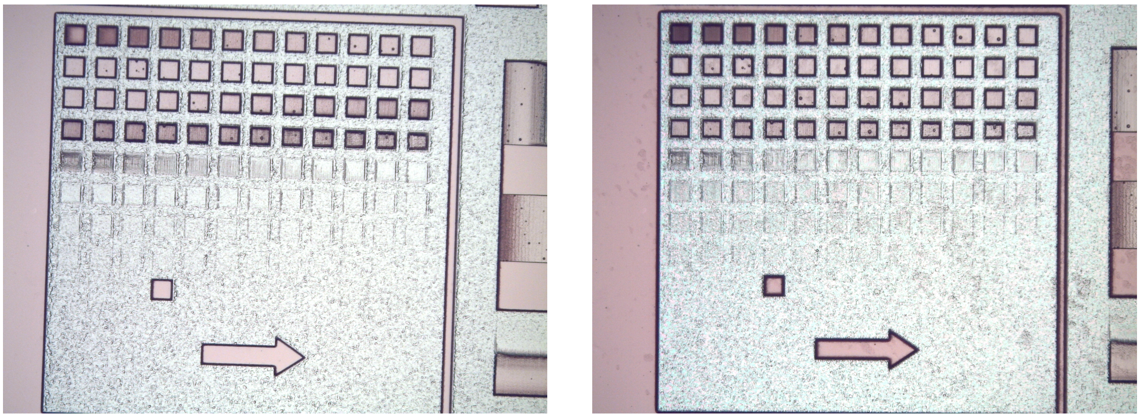

(a) After 2’ 35"

(b) After 4’

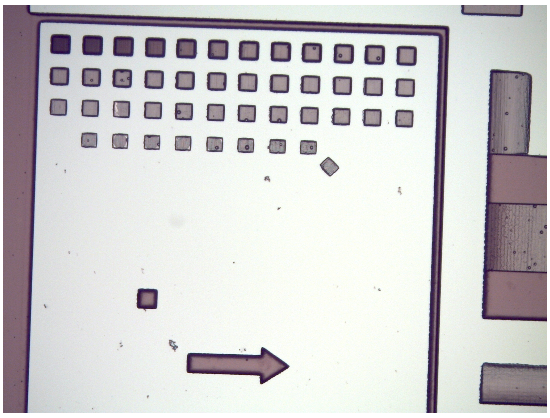

(c) After 5’

Figure 5.7: **M01** optical microscope images for increasing development time

file through the optical profilometer, revealed that the lower end of the grayscale had been significantly eroded: specifically, the unexposed areas (RGB = 0), which should have the full spin-coated thickness (approximately $9\ \mu m$), appeared to have been reduced to $8\ \mu m$ (Figure 5.8).

This corroborates the hypothesisis that the sample has been **overdeveloping**, likely due to the prolonged immersion required to clear the higher grayscale regions.

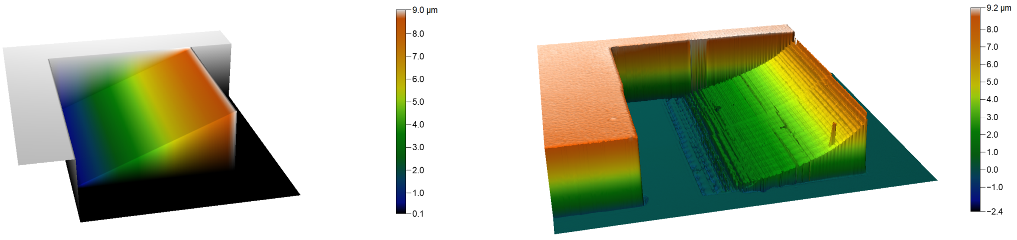

(a) Expected ramp profile

(b) **M03** ramp profile

Figure 5.8: 3D renderings of a ramp profile (via Gwyddion)

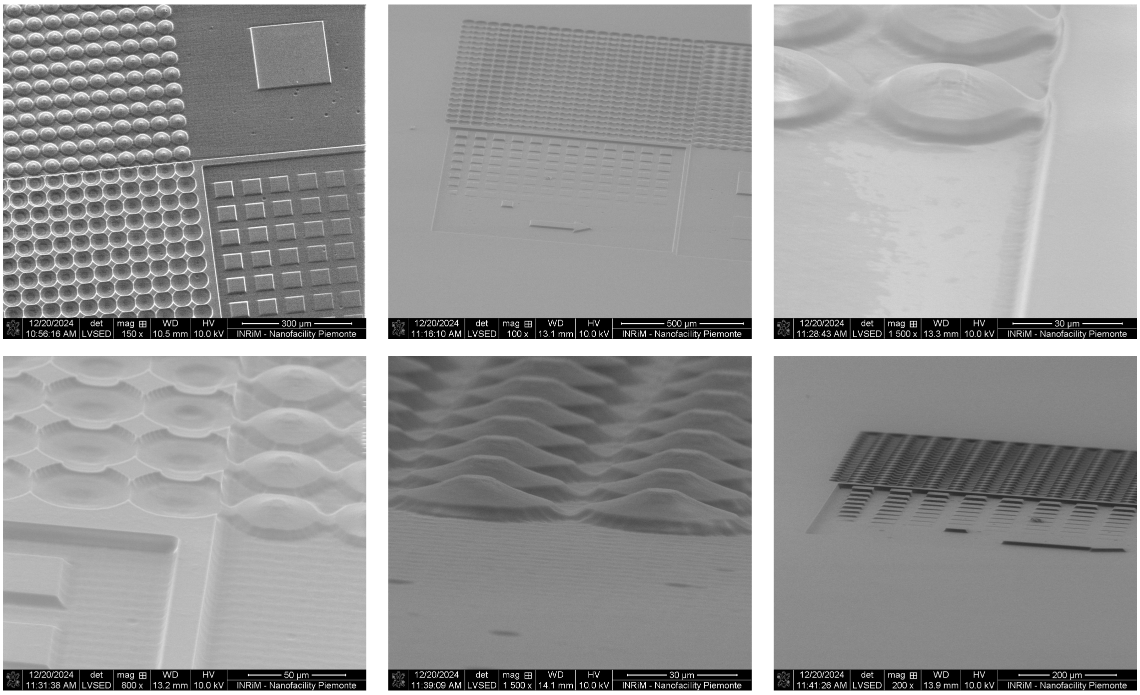

Figure 5.9: SEM images of a grayscale test sample

Based on the results obtained so far, it became clear that achieving an optimal grayscale lithography (where each RGB level corresponds to a unique and stable resist thickness) was not feasible with the photoresist used.

Specifically, in order to get any appreciable thickness for high RGB values (RGB > 50), even at low exposure powers, prolonged development times were required.

However, such long developments inevitably led to overdevelopment even to non-exposed areas. Conversely, increasing the exposure power and reducing development time to avoid overdevelopment, resulted in the complete loss of high-RGB features.

Given these limitations, and considering that the application on PAZO targets resist thicknesses $< 5\ \mu m$, a different strategy was adopted (Figure 5.10).
Instead of attempting to map the full 0-100 RGB grayscale range to absolute thickness values (i.e. ranging from the substrate surface to the whole resist thickness), the new approach focuses on a limited and more controllable RGB interval ensuring two key conditions:

1. All selected RGB values consistently yield different and distinguishable resist thicknesses.
2. The resulting structures are repeatable for each lithography under the same conditions.

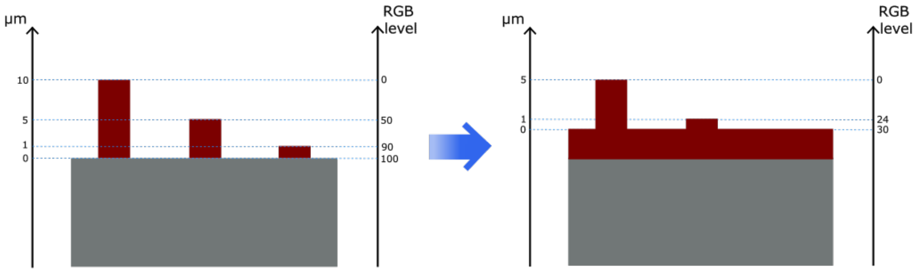

Figure 5.10: Illustration of the remaining photoresist after development with the old (left) and new (right) approach

Once the usable grayscale range satisfying the two requirements mentioned above had been identified (specifically, RGB < 35) a series of calibration samples were fabricated to fine-tune the resulting relative heights by adjusting the base RGB level.

Since the goal on PAZO was to implement a pixelated pattern in which each pixel contained two pillars of different heights, the target was to create a structure where the "tall" pillar had a height around $4\ \mu m$, and the "short" one around $1.5\ \mu m$.
This configuration was chosen to ensure a significant dynamic contrast in response while guaranteeing the thinner structures are above the noise threshold and below the limits where response times become extremely long.

From the experimental results, it was found that these two thicknesses could be obtained by setting the background level to RGB$= 33$, assigning RGB$= 0$ to the taller pillar, and RGB$= 26$ to the shorter one.

These grayscale levels were then used to generate the final design, consisting of repeating pixel units with two distinct pillar heights.
In Figure 5.12 is shown the final design, with the repeated single pixel made with a big-

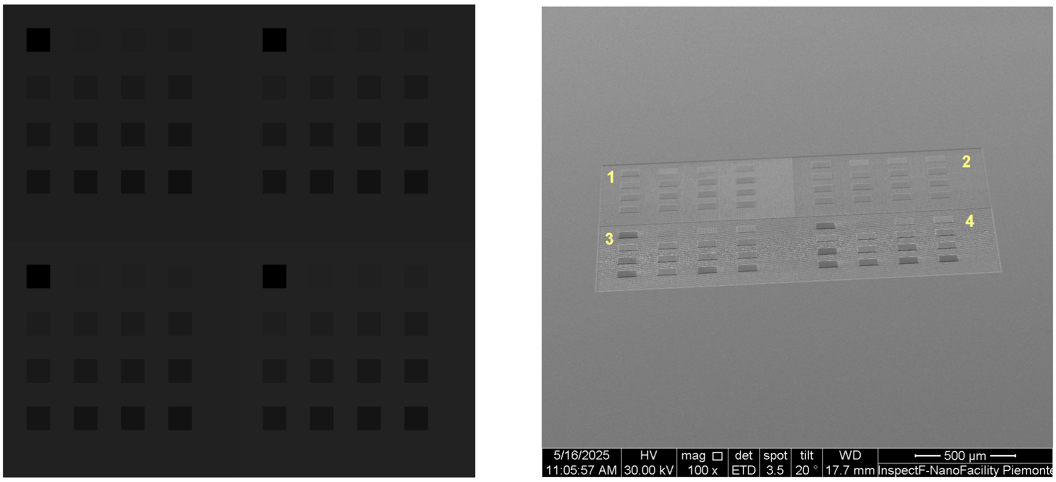

(a) Design (b) SEM sample image

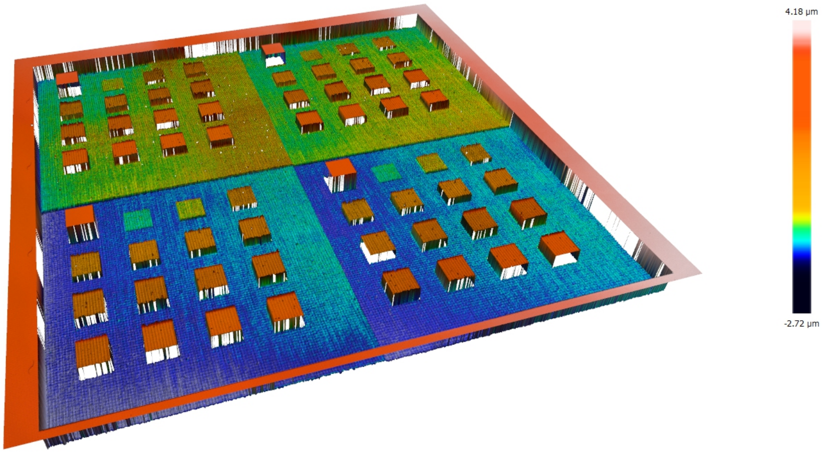

(c) Optical profilometer 3D rendering of the sample

Figure 5.11: Test sample for the fine tuning of the relative heights

ger surface (100 μm^2, above) and half the surface (50 μm^2, below) to allow dynamic measurements with different power densities.

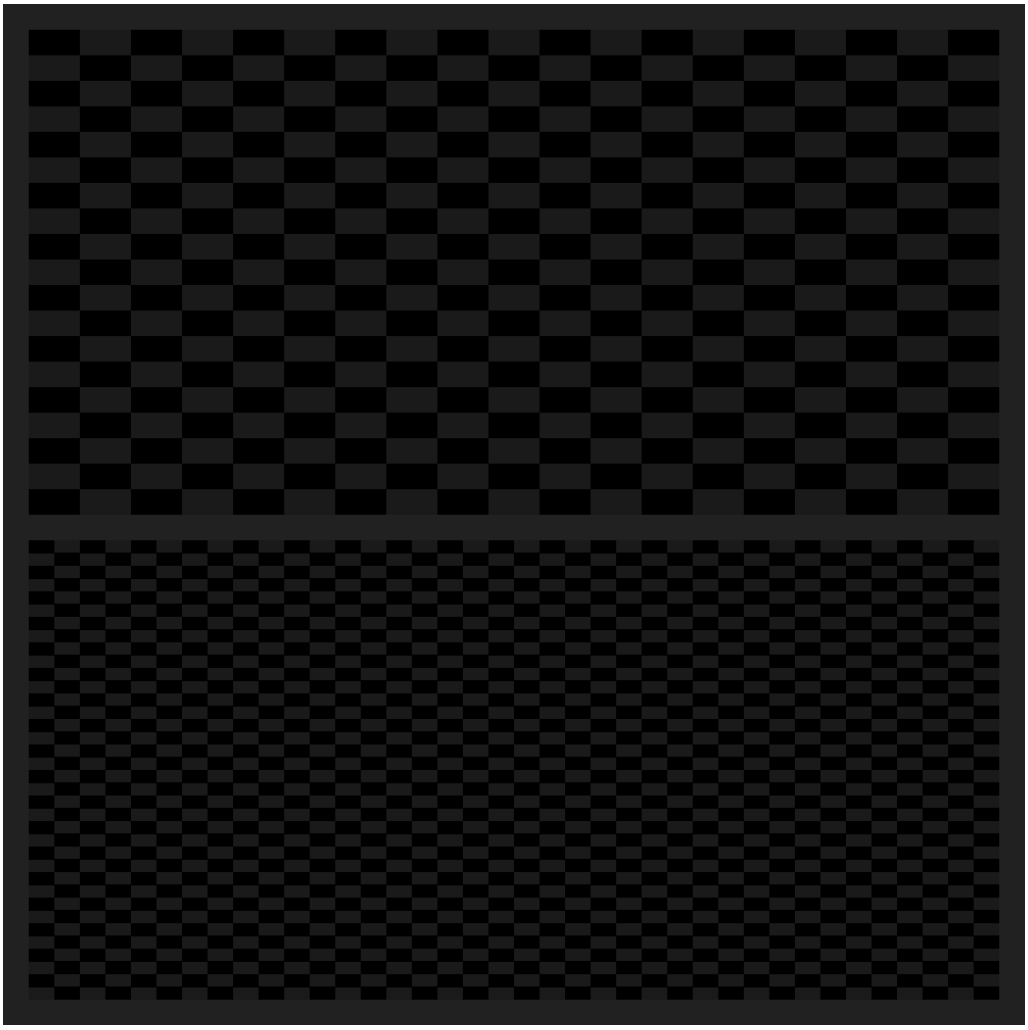

Figure 5.12: pixelated microstructures design

The resulting microstructured surface of the fabricated master was characterized using an optical profilometer, and the corresponding 2D surface rendering is presented in Figure 5.13a. The average height profile of a single pixel unit reveals two distinct levels, corresponding to approximately 4.8 μm for the taller pillar and 1.2 μm for the shorter one (Figure 5.13b).

Negative replicas fabrication

To transfer the patterns generated on the grayscale resist samples onto a polymer film, the most effective approach involves the use of a soft elastomer such as PDMS (Polydimethylsiloxane), which enables the formation of a negative replica of the original microstructures.

The steps I used to fabricate the replicas are listed in Table 5.4

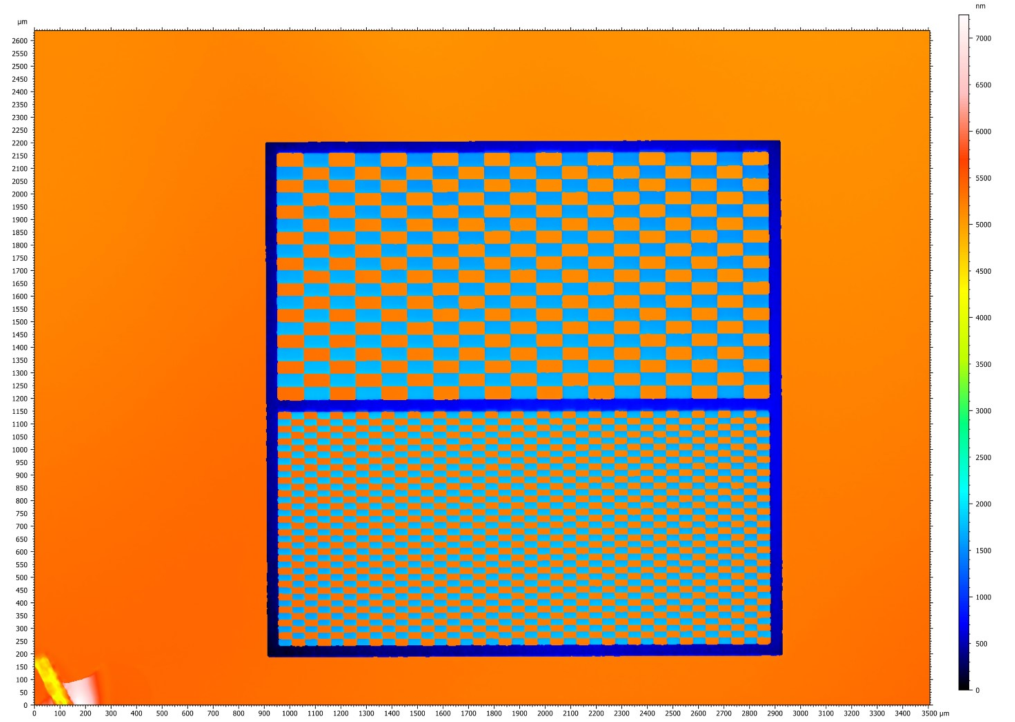

(a) 2D rendering of the pixelated master

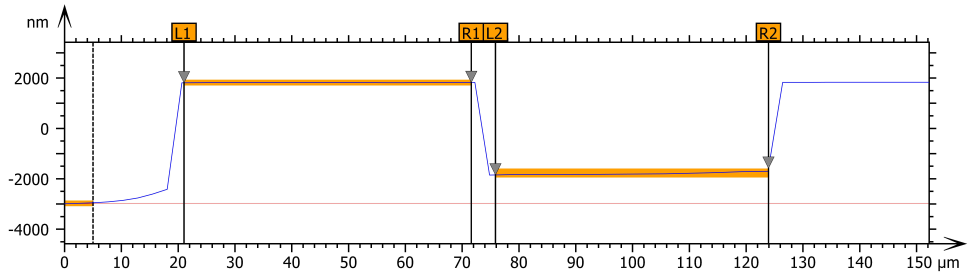

Parameters	Unit	Step 1	Step 2
Width	µm	51.6000	51.6000
Maximum height	nm	4805.08	1279.18
Mean height	nm	4801.82	1186.95

(b) Single pixel profile view

Figure 5.13: pixelated master image

Step	Description
1	Weigh the required amount of PDMS base (Sylgard 184, Dow Corning).
2	Use a micropipette to add the curing agent at a 10:1 weight ratio with respect to the base.
3	Combine the two components and mix thoroughly using a spatula until the solution is well mixed.
4	Pour the liquid PDMS onto the grayscale resist master, which is positioned with the patterned side facing upward.
5	Degas the sample in a desiccator for approximately 1 hour or until all surface bubbles disappear.
6	Cure the PDMS in an oven at $70\,C$ for 3 hours.
7	Carefully peel off the solidified PDMS mold from the master.

Table 5.4: Protocol for PDMS mold fabrication from grayscale resist masters.

The PDMS, in its liquid state, is first poured over the master where it can infiltrate the cavities of the pattern. After degassing and thermal curing, the material solidifies while retaining its high elasticity.
This allows for gentle peeling from the master without damaging the features, resulting in a faithful negative mold of the grayscale pattern.

In Figure 5.14, a comparison is shown between the final PDMS replica (Figure 5.14a) and the pixelated master (Figure 5.14a) from which it was replicated.
It can be observed that the PDMS replica is the negative of the master pattern: the high and low pillars have become cavities that are now respectively deeper or shallower relative to the surrounding frame.
In the master, this frame was the most recessed region at the end of the grayscale lithography, whereas in the replica it is now the most protruding part. During the molding process, this frame comes into contact with the glass substrate, and the PAZO solution fills the cavities by capillary action, reproducing the original pattern of the master.

PAZO molding

To pattern the PAZO film according to the master design, the negative replica of the pattern in PDMS was employed, using soft lithography techniques.
Specifically, three distinct methods were utilized for samples fabrication: Micro-transfer Molding (μ**TM**), Solvent-Assisted Microcontact Molding (**SAMIM**), and Soft-Molding (**SM**). A comprehensive description of these techniques is provided in 2.2.

Generally, these three techniques relies on the dissolution of the polymer in a solvent capable of permeating the PDMS stamp cavities.

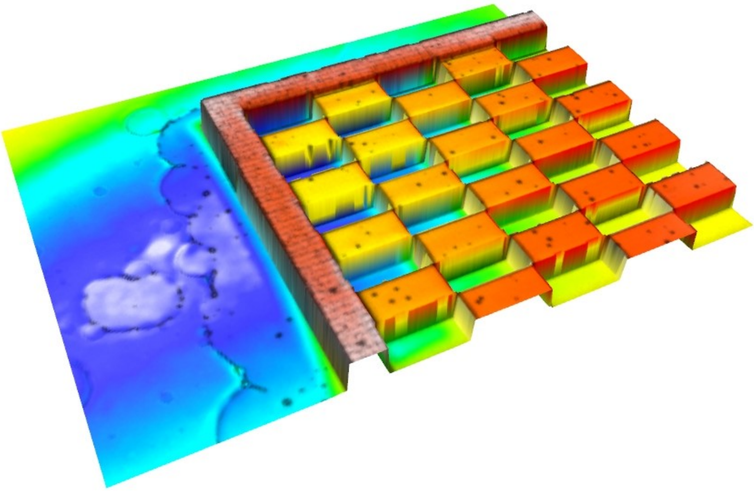

(a) PDMS replica

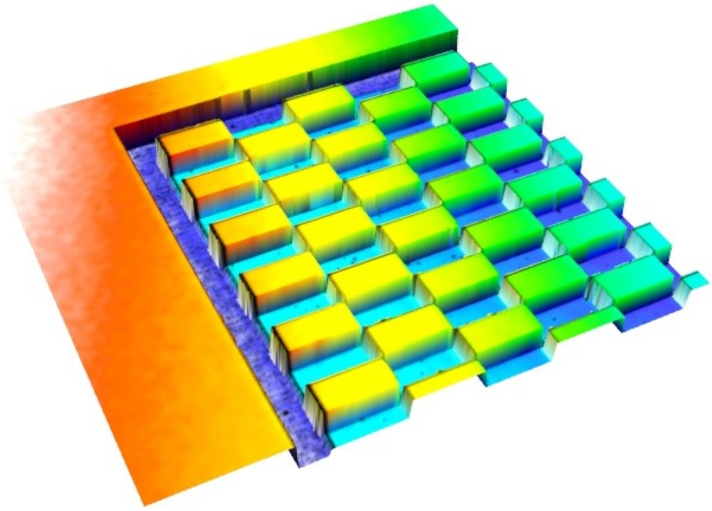

(b) Master

Figure 5.14: Comparison between the 3D optical profilometer rendering snippets of the pixelated sample for the master and the relative PDMS replica

Upon solvent evaporation, the remaining solute (in this instance PAZO) solidifies, replicating the intended pattern.
This stage constitutes the most delicate step in the PAZO sample fabrication process, as achieving high-fidelity structures is not assured and is dependent on many factors.
Consequently, isolating the precise parameters that induce defects in the final output proves to be a challenging task.
For example, parameters such as the processing temperature, the pressure exerted on the master-PDMS stack during molding, and the concentration of the solution employed can influence the outcome of all techniques. Establishing a direct cause-and-effect relationship for each parameter within each technique is difficult.

In the employing of the different molding techniques trade-offs between fidelity and repeatability have been evaluated.

The μ**TM** technique, for instance, is advantageous because it leaves only a thin residual layer of material at the base of the structures.
However, this benefit is severely undermined by its very low repeatability.
Significant uncontrolled variations in the height of pillars designed to be uniform, were consistently observed.
Plausible causes for this discrepancy include the sub-optimal removal of excess solvent from the PDMS pattern right after cavities-filling with the PAZO solution or not perfectly flat PDMS back-surface, leading to localized accumulations of liquid material and consequent non-uniform base layer.

SAMIM functions effectively in regions where the polymer film thickness, applied via spin-coating before molding, is precisely fit to fill the thickest features of the mold.
As explained before in (subsection 5.1.1), the main drawback is the difficulty in achieving this condition, which leads to low results repeatability. Obtaining uniform, sufficiently thick layers ($\sim 4\ \mu m$) is challenging.
Even when employing a solution at its solubility limit ($150\ mg/mL$) and spinning at low RPM, the target thickness was not reliably obtained.
While drop-casting could produce thicker layers, this method fails to yield a uniform thickness, resulting in significant height variations across a single sample.

Ultimately, after preparing numerous samples, it was concluded that the **SM** technique yielded the best and consistent results.
Its principal advantage is high repeatability, a critical factor for reliable sample fabrication.
This reliability, however, comes at the cost of two drawbacks.

First, a residual layer of undesired material ($\sim 1\ \mu m$) is consistently present at the base of the pattern.

Second, a general reduction in the final feature height was observed across all solution concentrations. This height reduction was more pronounced when using less concentrated solutions.

This effect is likely attributable to insufficient solute concentration, whereby the quantity of polymer remaining after solvent evaporation is unsufficient to completely fill the PDMS cavities.

Despite these issues, the repeatability of SM made it the best choice for this work.

The main advantages and limitations of each method are summarized in Table 5.5.

Technique	**Pros**	**Cons**
μTM	A thin residual layer remains at the base of the structures.	Very low repeatability and significant pillar height variation due to potential issues with excess solvent removal and stamp non-parallelism.
SAMIM	Works well where the pre-spun polymer film thickness is optimal for the feature height.	Low repeatability due to the difficulty in achieving uniform and sufficiently thick spin-coated layers for high-aspect-ratio structures.
SM	High repeatability of the results.	Presence of an undesirable residual layer and a general reduction in feature height, more pronounced at lower concentrations.

Table 5.5: Summary comparison of the employed molding techniques for PAZO

Dynamic response of a microstructured PAZO sample

Before defining the final workflow for the pixelated structure fabrication, a preliminary sample was designed to study the dynamic response as a function of the PAZO layer thickness within a single device.

The objective was to replicate the previous experiments, performed on separate samples with uniform thickness, on a single, multi-thickness structure to reduce variability and simplify comparisons.

To achieve this, I started from the grayscale design shown in Figure 5.16, which features three sets of nine pads, each with varying lateral dimensions and a grayscale step of $\Delta_{\mathrm{RGB}} = 10$ between pads.

The master was fabricated using the earlier grayscale lithography approach: the full RGB

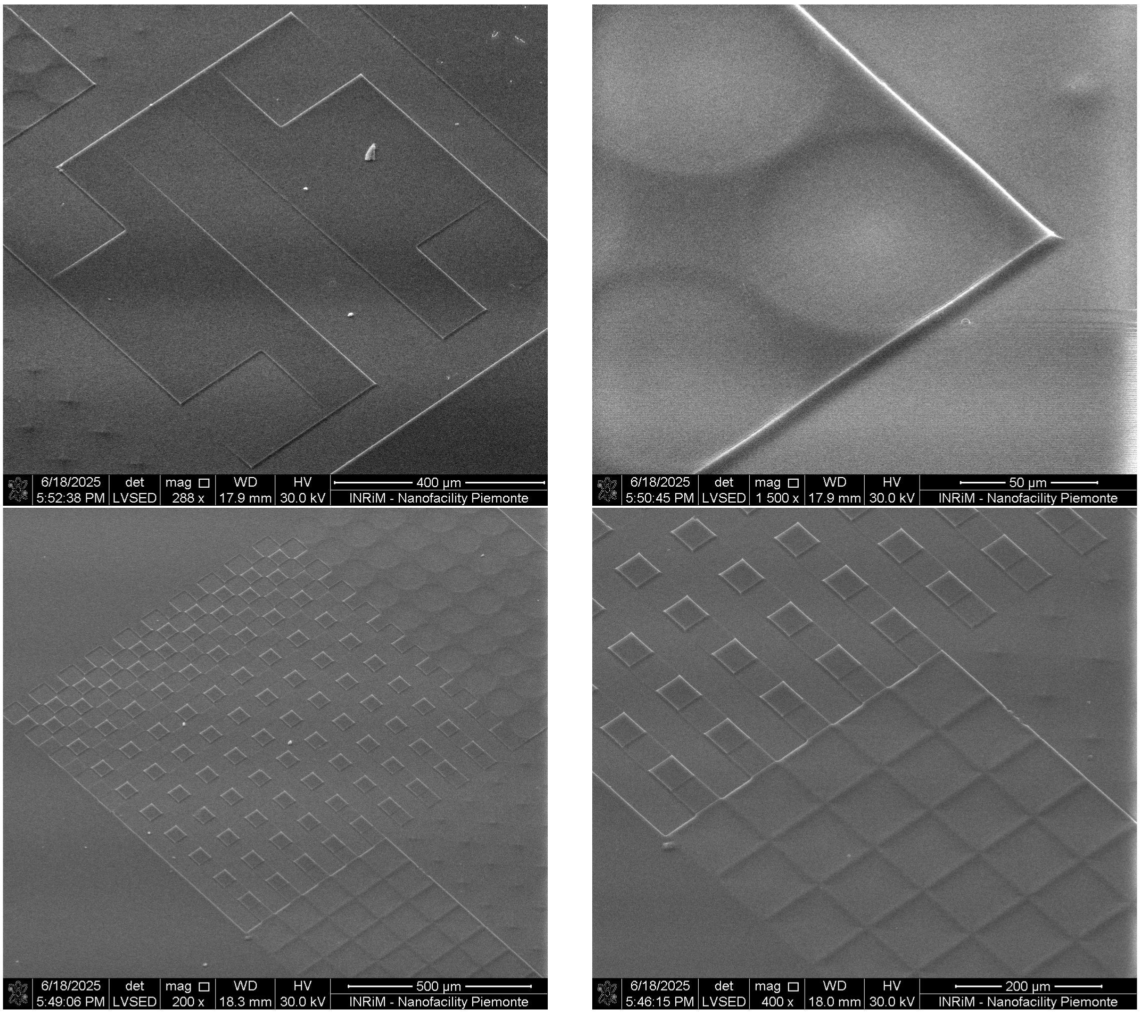

Figure 5.15: SEM images of the PAZO replica of a test design

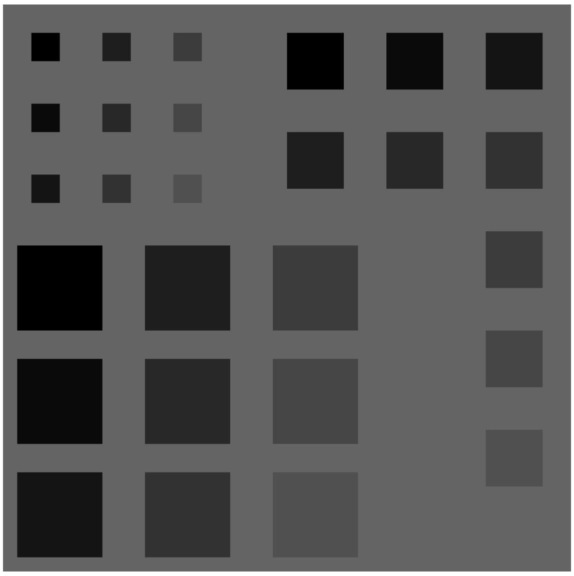

Figure 5.16: Design for the multi-thickness experiment

scale (0–100) was employed, and the development time was intentionally kept shorter than the time required to completely remove the resist in the brightest areas.
This ensured that all nine grayscale levels, and therefore all nine resulting thicknesses, were still present and distinguishable.

The negative mold was then produced in PDMS following the steps outlined in Table 5.4.
Finally, the PAZO replica was fabricated using the **SM** technique and a PAZO solution with a concentration of 50 mg/mL.
The final result can be seen in Figure 5.17. It is clearly visible that the replica was not perfect because of an unexpected void of material in a region that had to be patterned, which can be due to one of the process faults described above.
Other typical defects can be observed, like the remaining layer of material above the substrate and the shrinkage of the structure's heights.
Despite these non-ideal replica there are sufficient regions with different thickness that can be characterized. In particular, the ones depicted in Figure 5.17 had been chosen calculating the mean thickness of those regions by means of the optical profilometer.
The thickness has been calculated with respect to the glass substrate to take in consideration the unwanted base layer of material above which the pads had been formed.

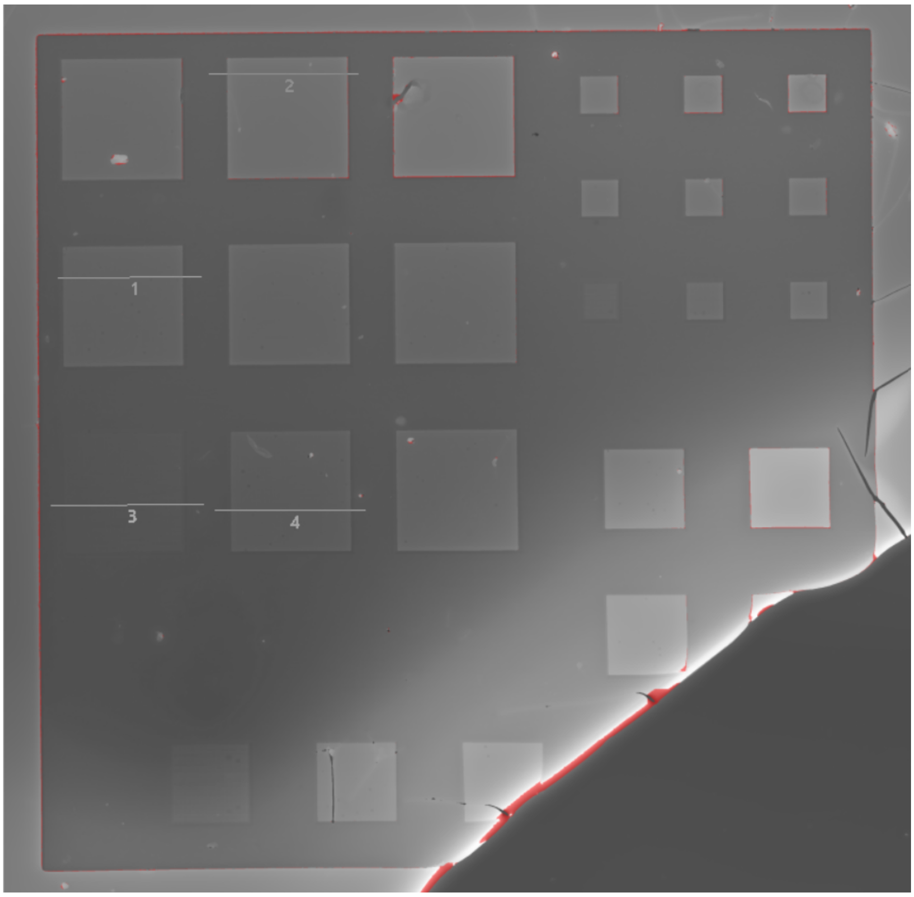

(a) Total image of the final replica with the pads profile lines

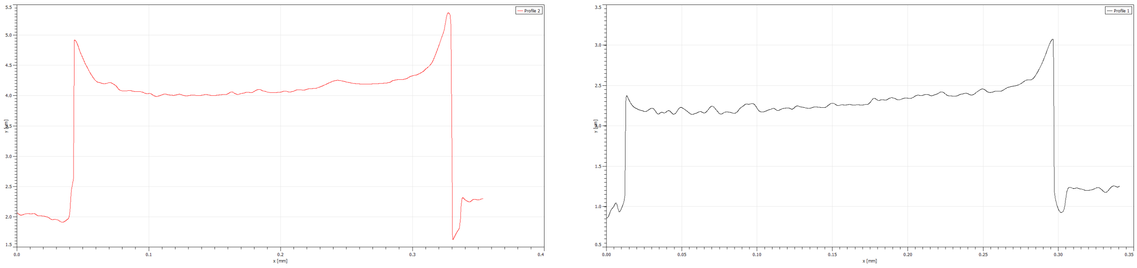

(b) 4 μm pad

(c) 2.1 μm pad

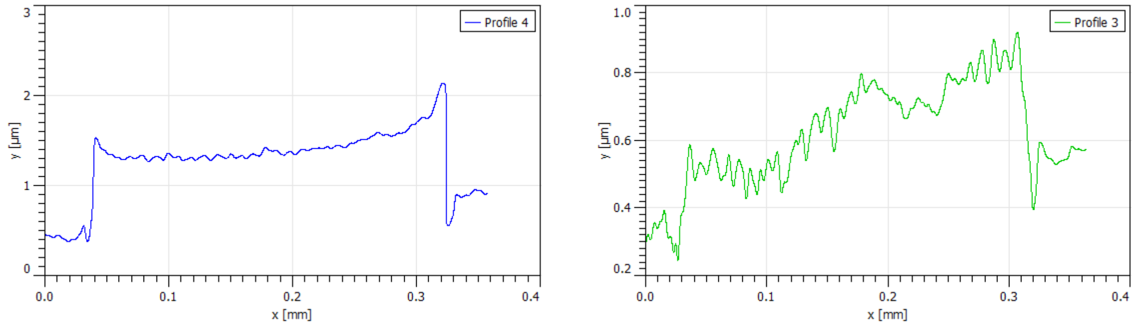

(d) 1.3 μm pad

(e) 0.6 μm pad

Figure 5.17: Profilometer images of the Figure 5.16 PAZO replica and profile views of the four thickness used in the experiment.

The dynamic response experiment was then carried out by stimulating the sample using a green laser with a 20X objective and a spot diameter $D = 47\ \mu m$ under two distinct stimulation regimes:

- **Maximum stimulation**: achieved by selecting the laser power and duration ($t_{\text{on}} = 1\ s$) just below the deformation threshold (i.e., the onset of mass migration) for the tallest pillar (d $\sim 4\ \mu m$).
- **Minimum stimulation**: determined by selecting a laser power and short duration ($t_{\text{on}} = 200\ ms$) such that the smallest pillar (d $\sim 600\ nm$) produces a clear signal of $\Delta I = 1.6\ a.u.$, well above the noise level (~ 0.6).

The final values of power and corresponding power densities used in the experiment were:

$$P_{\text{min}} = 14.2\ \mu W \qquad \rho_{\text{min}} = 8.3\ \text{nW}/\mu m^2$$
$$P_{\text{max}} = 142\ \mu W \qquad \rho_{\text{max}} = 82.7\ \text{nW}/\mu m^2$$

In Figure 5.18 are shown the responses for each stimulation condition, normalized with respect to their offset for visualization and comparison purpose.
As expected, there is a trend in the maximum intensity reached, that increases with the stimulated thickness (Figure 5.19).
The similarity in the curves for $t_{\text{on}} = 1\ s$, $P = 14.2\ \mu W$ and $t_{\text{on}} = 200\ ms$, $P = 142\ \mu W$ can be explained with a similar energy density given in these two conditions.

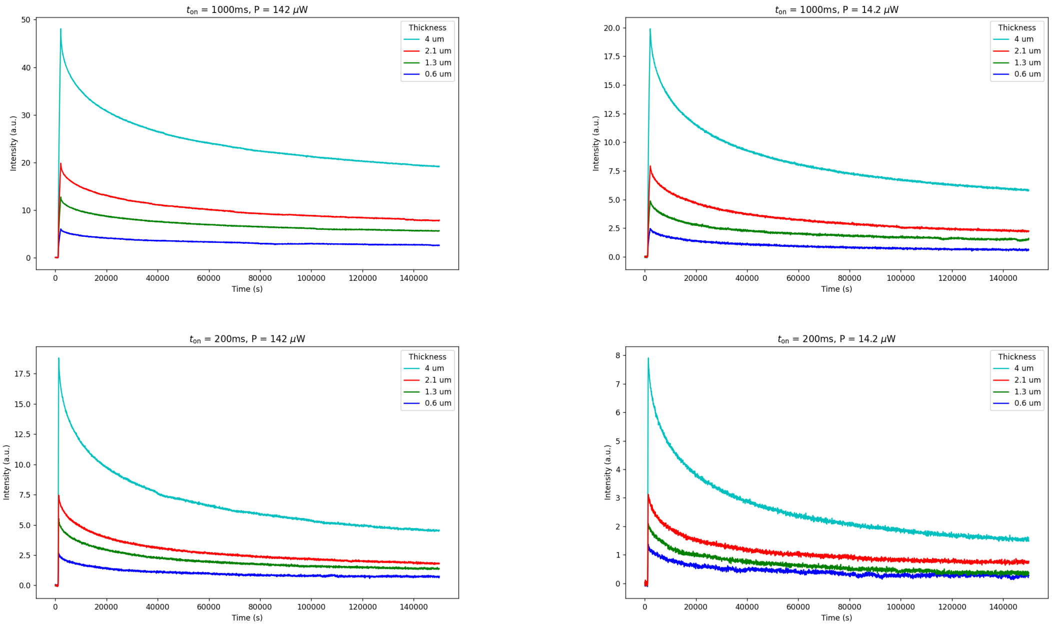

Figure 5.18: Different thicknesses dynamic response for each P-t_{on} combination

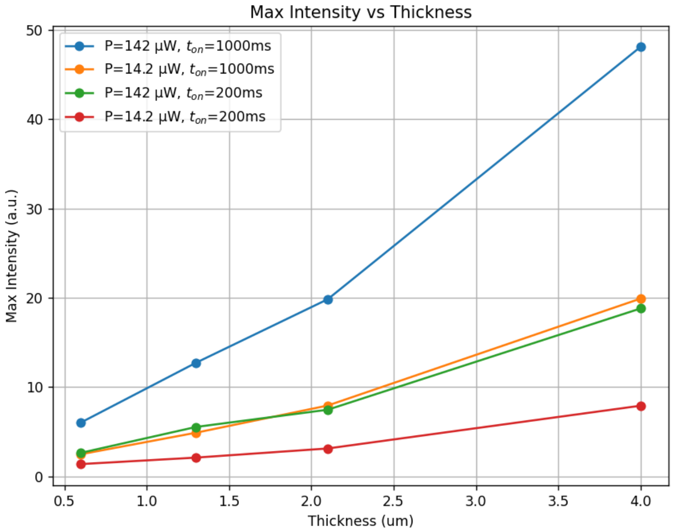

Figure 5.19: Maximum reached intensity for the four stimulation conditions

5.2.2 Microstructured PAZO sample for luminance adaptation

Finally, the sample featuring the pixelated structure illustrated in Figure 5.12 was fabricated following the complete workflow described for grayscale lithography and PDMS mold replication. The final replica was obtained using a PAZO solution with a concentration of 150 mg/mL and the **SM** technique (Figure 5.20).

As shown in Figure 5.21, the resulting pillars exhibit the typical issues already discussed during the analysis of the soft-molding replicas: the top surfaces are not perfectly flat, the overall heights are reduced compared to the expected values, and a residual layer of material approximately $1\ \mu m$ thick is consistently present at the base of the pattern.

Looking at the profile view of a single pixel in Figure 5.22a, it can be seen that the taller pillar reaches approximately $2\ \mu m$ in height, while the shorter one is about $450\ nm$: These values correspond to the height difference measured from the base level of the pixel, and appear lower than originally expected (Figure 5.13b).
However, as highlighted in Figure 5.22b, the presence of a residual material layer of approximately $1\ \mu\text{m}$ increases the absolute heights, near the intended structural dimensions. In the end the taller pillar is approximately $3\ \mu\text{m}$ in height, and the shorter one is about $1.4\ \mu\text{m}$.

Figure 5.23 and Figure 5.24 show a 3D section rendering and profile details of two representative pillars, across the entire replication chain: from the original master, to the PDMS negative replica, and finally to the microstructured PAZO layer.
The comparison highlights the inversion between the master and the PDMS stamp, where raised features become cavities, as well as the subsequent reappearance of the original

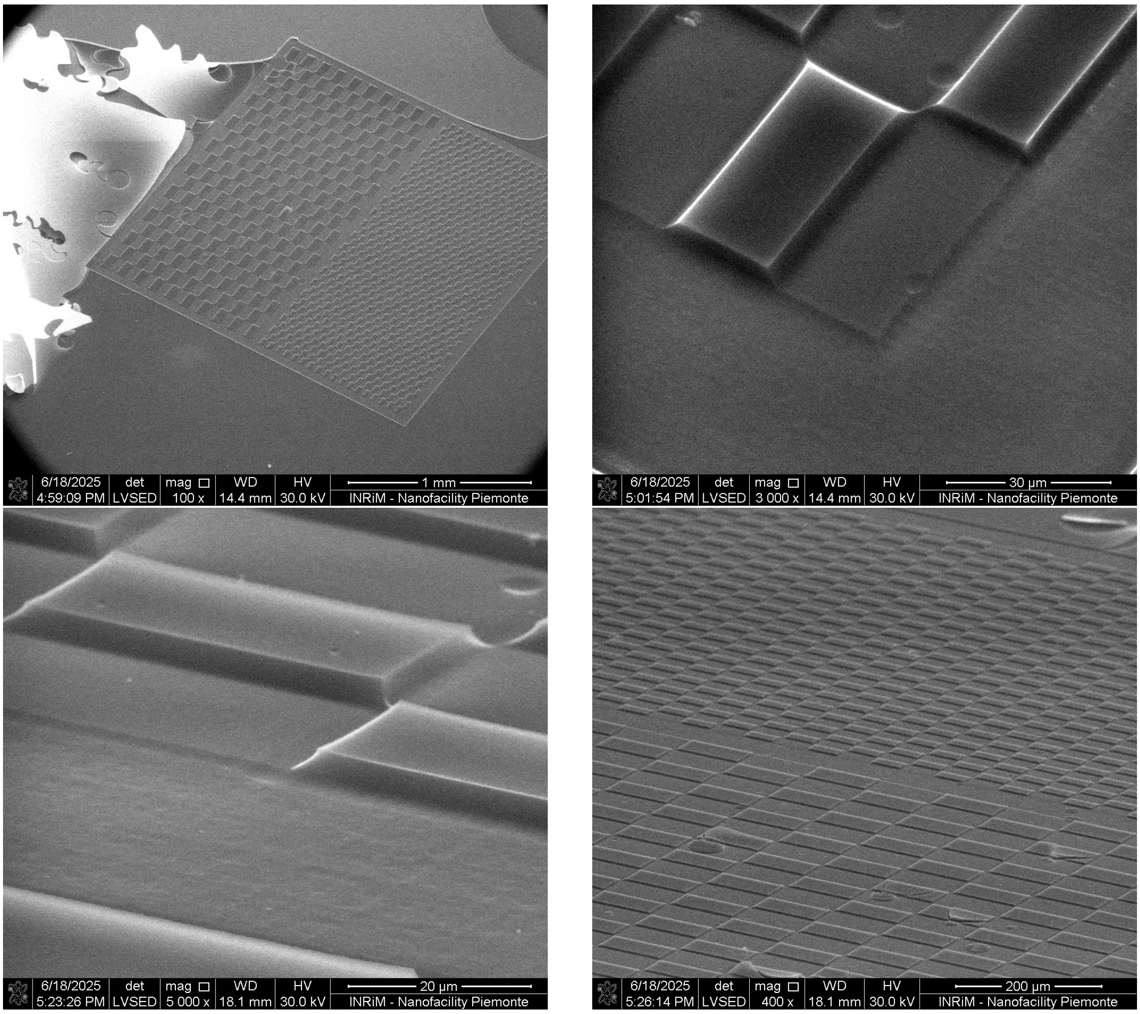

Figure 5.20: SEM images of the pixelated PAZO sample

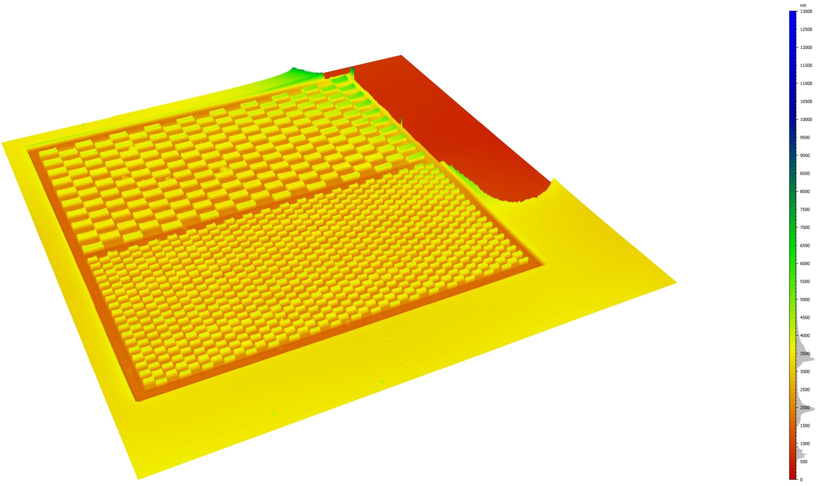

Figure 5.21: Optical profilometer 3D rendering of the pixelated PAZO sample

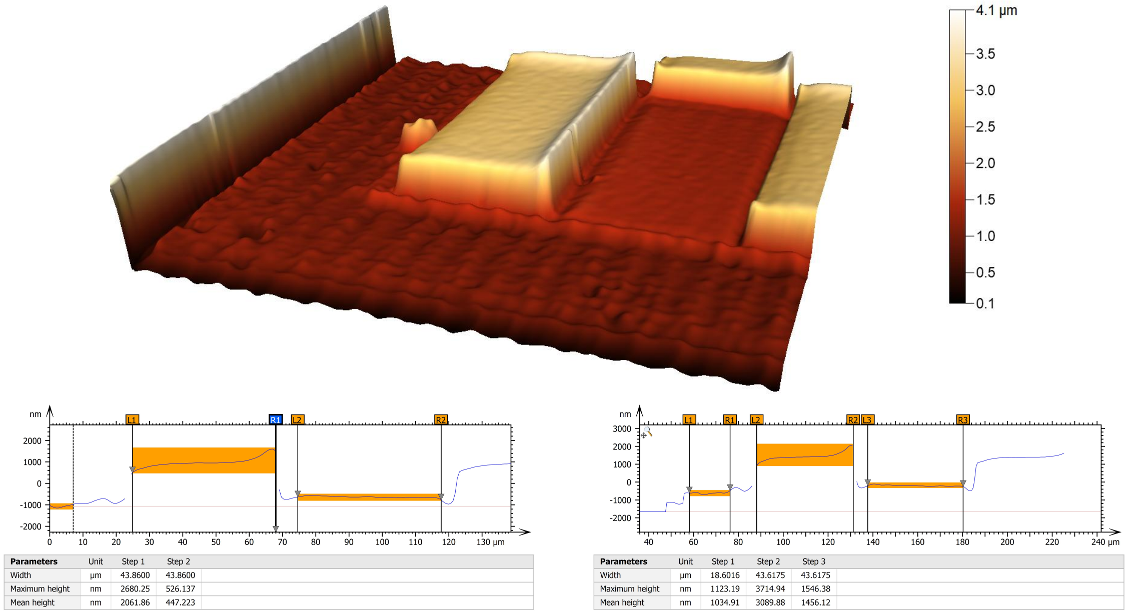

Parameters	Unit	Step 1	Step 2
Width	µm	43.8600	43.8600
Maximum height	nm	2680.25	526.137
Mean height	nm	2061.86	447.223

(a) Relative pixel profile view

Parameters	Unit	Step 1	Step 2	Step 3
Width	µm	18.6016	43.6175	43.6175
Maximum height	nm	1123.19	3714.94	1546.38
Mean height	nm	1034.91	3089.88	1456.12

(b) Absolute pixel profile view

Figure 5.22: Optical profilometer 3D rendering of a pixel and detailed profile section views

geometry in the PAZO structure through capillary-assisted replication.

As shown in Figure 5.24, a slight loss of fidelity with respect to the master can already be observed in the PDMS replica, where both pillars exhibit slightly reduced heights.
However, the most significant fidelity loss occurs during the final structuring of the PAZO layer: here, both pillars reach only about half the depth of the corresponding cavities in the PDMS stamp.
This supports the hypothesis that the main limiting factor is the maximum achievable concentration of the PAZO solution. In fact, even when using the highest possible concentration ($150\ mg/mL$), only approximately half of the expected 'solid content' is retained in the final structure.

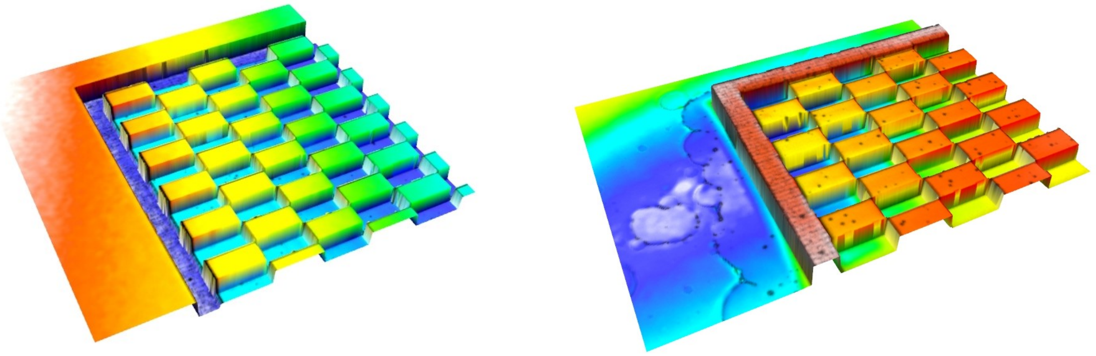

(a) Master (b) PDMS replica

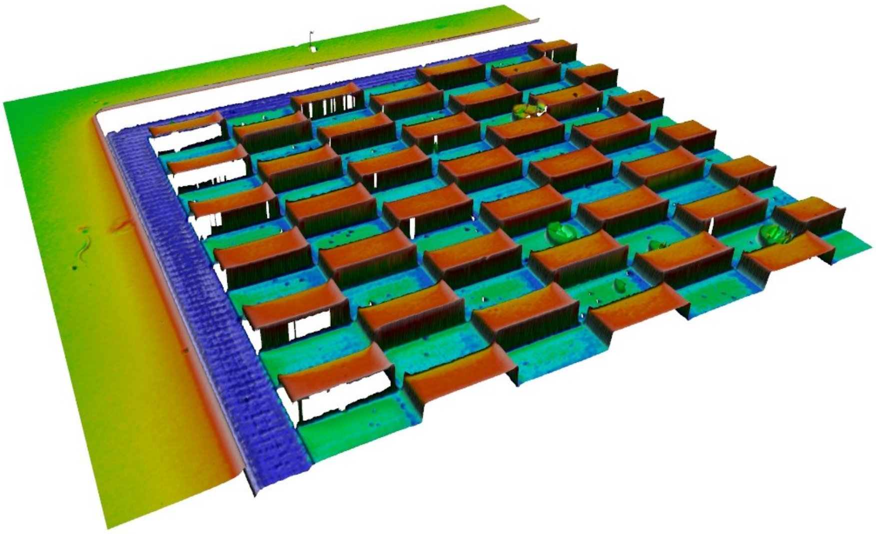

(c) PAZO sample

Figure 5.23: Summary comparison for the whole pixelated sample workflow, from the master (a), to the PDMS negative replica (b), to the microstructured PAZO (c)

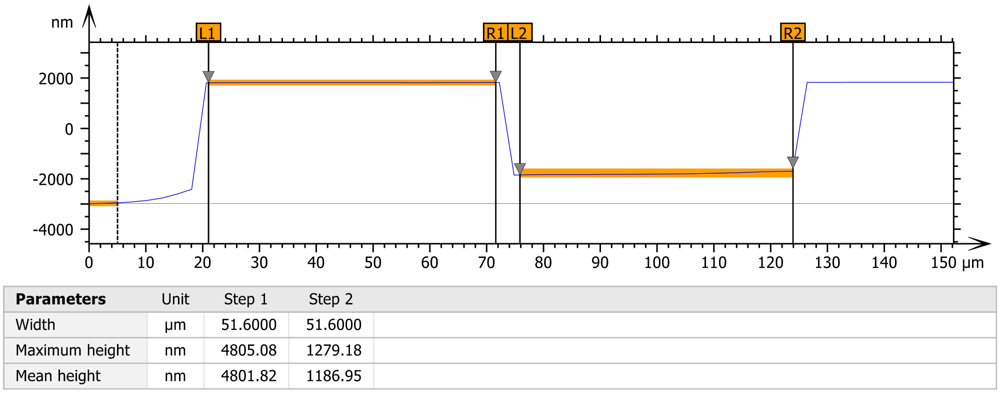

Parameters	Unit	Step 1	Step 2
Width	µm	51.6000	51.6000
Maximum height	nm	4805.08	1279.18
Mean height	nm	4801.82	1186.95

(a) Master

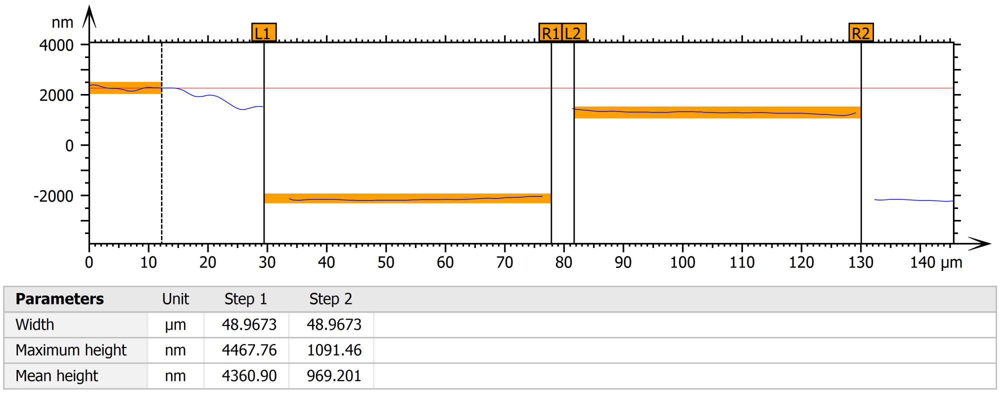

Parameters	Unit	Step 1	Step 2
Width	µm	48.9673	48.9673
Maximum height	nm	4467.76	1091.46
Mean height	nm	4360.90	969.201

(b) PDMS replica

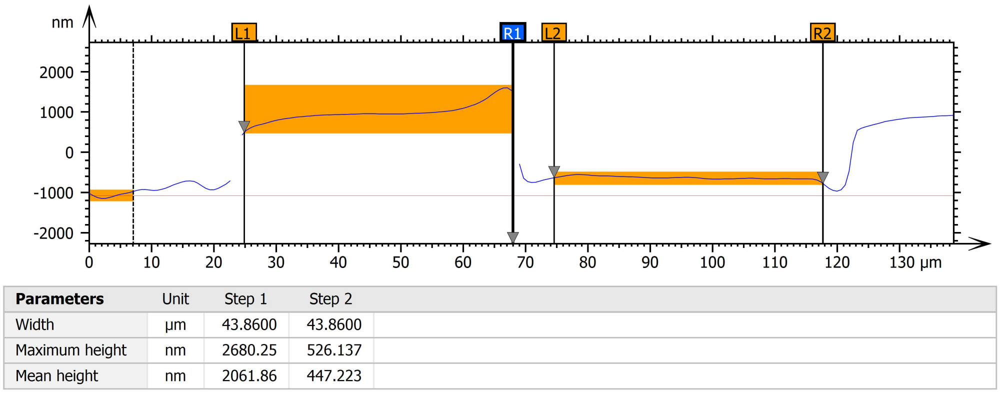

Parameters	Unit	Step 1	Step 2
Width	µm	43.8600	43.8600
Maximum height	nm	2680.25	526.137
Mean height	nm	2061.86	447.223

(c) PAZO sample

Figure 5.24: Comparison of a single pixel's profile view, from the master (a), the PDMS negative replica (b) and the microstructured PAZO (c)

These values are still sufficient to observe a clear different behavior in the dynamic response under laser stimulation, allowing for an effective performance comparison between the two pillars in the same pixel.

With the fabricated structure consisting of periodic units (pixels), each composed of two

pillars of different height, the next step was analyzing their dynamic optical response under varying stimulation conditions.
The aim was to identify the effective dynamic range, i.e. the range of stimulation power and exposure times that lead to a measurable response for the two pillar within a single stimulation.

The experimental setup used to stimulate and probe the birefringence dynamics is the same described in subsection 3.1.1.
The signal is collected using a CCD camera, which records the transmitted intensity encoded over 8 bits. Consequently, the signal can vary from 0 to 255 arbitrary units (a.u.), corresponding to the full dynamic range of the detector.

Given a fixed exposure time and camera gain, two signal constraints were identified:

- **Saturation**: occurs when the signal reaches the upper limit of 255 a.u., beyond which information is lost due to clipping.
- **Noise threshold**: occurs when the signal is too weak to be distinguished from background fluctuations.

To quantitatively determine the noise threshold, a statistical approach based on the three-sigma criterion was applied.
Transmitted intensity data from both types of pillars were acquired under steady, unstimulated conditions for a duration of 20 seconds.
From this baseline, the standard deviation σ of the signal was computed. The threshold above which a signal is considered distinguishable from noise was then set as:

$$I_{\text{noise}} = \mu_{\text{baseline}} + 3\sigma \tag{5.1}$$

where μ_{baseline} is the mean transmitted intensity under baseline conditions, and σ its standard deviation.
In practice, the baseline mean was close to zero due to normalization, and the condition for a valid signal becomes:

$$I_{\text{signal}} > 3\sigma \tag{5.2}$$

This defines the minimum intensity variation that can be reliably attributed to photoinduced effects, rather than background noise.
From the experimental measurements, the noise floor was estimated to be approximately:

$$I_{\text{noise}} \approx 0.45 \text{ a.u.} \tag{5.3}$$

This value was then used as a lower bound for the dynamic range. Any transmitted intensity below this threshold was considered indistinguishable from noise, while any signal exceeding it was deemed significant. The combination of this noise floor with the upper saturation limit of 255 a.u.. defined the usable intensity window for evaluating the dynamic optical response of the pillars under various stimulation protocols.

In order to stimulate both pillars of a single pixel simultaneously, the digital micromirror device (DMD) integrated into the optical setup was used to project a square light pattern onto the sample.
The projected square was defined to match the dimensions of one pixel on the structured sample, ensuring that a single exposure would induce a response in both the taller and shorter pillars.
To enable quantitative comparison of their birefringence dynamics, two regions of interest (**ROIs**) were defined in the acquisition software, each corresponding to the footprint of one pillar. The mean transmitted intensity within each ROI was then computed for every time frame, yielding two independent dynamic curves for each stimulation.

Experiments were conducted on pixel arrays with dimensions of $100 \times 100\ \mu\text{m}^2$. In order to cover this area with adequate resolution, a $5\times$ objective was employed in both stimulation and detection. The writing beam used in these measurements is the green mode ($532\ nm$) of the MatchBox laser.

The usable power range and current control settings for the green laser had already been characterized and are reported in Figure 4.2. However, due to optical losses introduced by the projection path, including lenses, mirrors, and the DMD itself, a new power-current (P–I) calibration was performed with the projector in place.
The resulting calibration curve, shown in Figure 5.25, represents the actual optical power reaching the sample as a function of the driving current. This curve was acquired with the projected stimulus defined as a black square (RGB = $(0, 0, 0)$), corresponding to the maximum available projected intensity.

In addition to current modulation, fine control over the stimulation power was achieved by adjusting the grayscale value of the projected pattern.
The DMD software allows the definition of stimulus patterns with arbitrary RGB levels; setting a non-zero RGB value effectively attenuates the projected power.
For instance, defining the same square region with RGB = $(25.5, 25.5, 25.5)$ (equivalent

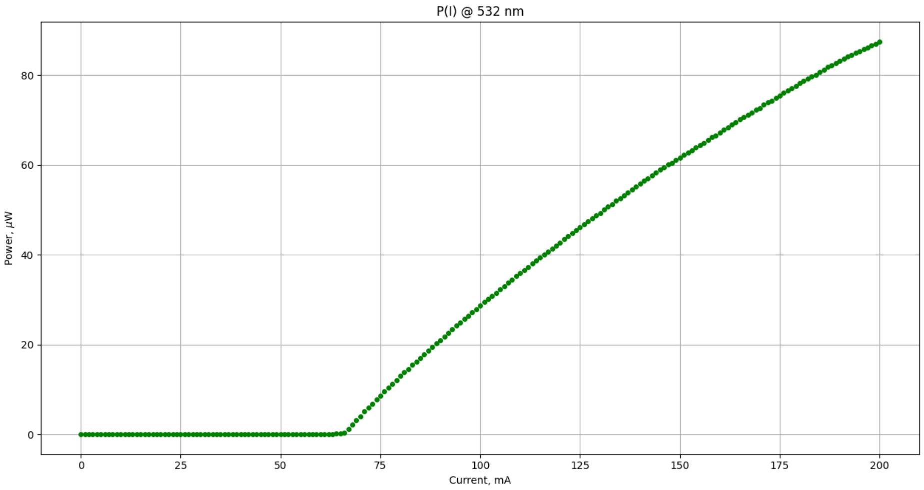

Figure 5.25: Power-Current laser calibration plot with the DMD

to RGB = 10 on a 0–100 normalized scale), reduces the optical power following the attenuation curve reported in Figure 5.26. This approach allows intermediate stimulation levels that would not be possible otherwise.

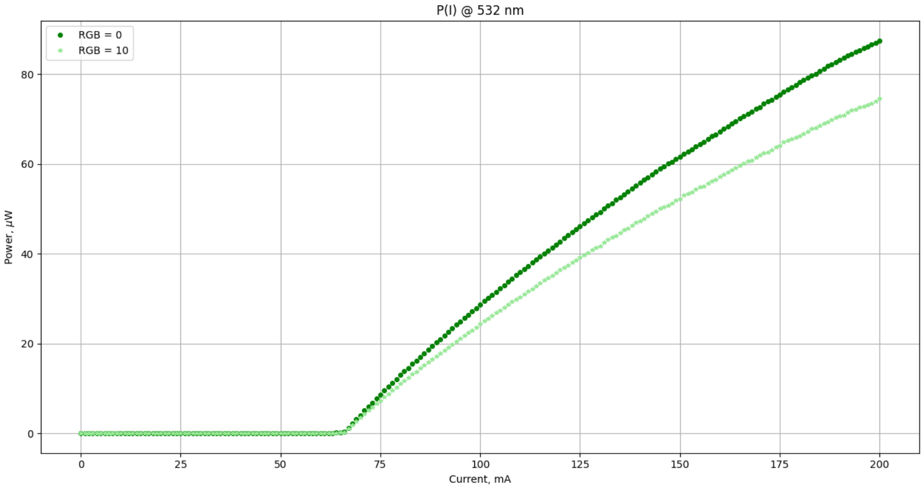

Figure 5.26: Comparison of the P-I calibration plots for RGB = 0 and RGB = 10

High-power Regime

The first experiment in high-power regime was investigated by projecting the stimulus with `RGB` $= (0, 0, 0)$, corresponding to the maximum optical power delivered with the DMD ($P = 87.5\ \mu W$).

For each acquisition, the CCD was first allowed to record baseline data for $5\ s$ without stimulation.

Current (mA)	RGB	Power (μW)	Power density (nW/μm^2)
200	0	87.5	8.7
200	10	74.6	7.4
67	60	0.49	0.049
67	70	0.38	0.038
67	75	0.32	0.032
67	80	0.27	0.027

Table 5.6: Parameter used in the experiments

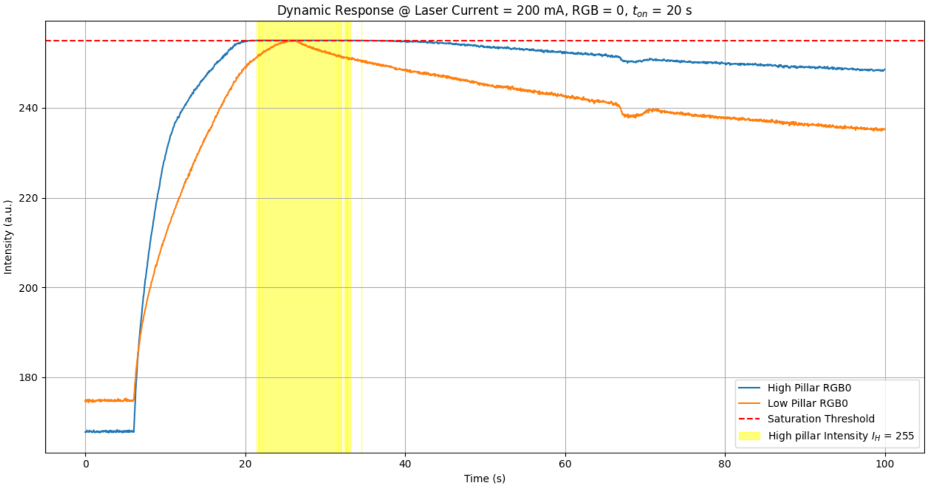

Figure 5.27: High-power regime dynamic response for RGB = 0

The writing beam was then switched on for $20\ s$, after which the sample was left to relax in the dark for $80\ s$.

The resulting dynamic responses for the mean intensity from both ROIs are reported in Figure 5.27.

A clear difference between the two structures is observed:

- **High pillar**: the transmitted-intensity signal rises rapidly and reaches the detector saturation limit ($I = 255$ a.u.) approximately $15\ s$ after the onset of stimulation. The signal remains clipped until the beam is switched off.
  Roughly $6\ s$ after stimulus removal, the intensity falls back below the saturation threshold, recovering a measurable signal.

- **Short pillar**: the corresponding curve increases throughout the $20\ \mathrm{s}$ exposure but never exceeds the saturation limit, remaining fully within the linear response range of the detector.

These observations confirm that, under maximum available power, the tall pillar rapidly exceeds the usable dynamic range of the CCD, whereas the short pillar remains readable for the entire duration of the stimulus.

A second experiment was conducted under identical stimulation current conditions, but with the projected pattern defined at `RGB` $= (25.5, 25.5, 25.5)$, corresponding to an RGB level of 10 on a 0–100 scale.
This configuration results in a reduced optical power at the sample surface, as described by the calibration curve in Figure 5.26.

The stimulation and acquisition protocol remained unchanged: a $5\ s$ baseline acquisition, followed by $20\ s$ of exposure, and a $80\ s$ relaxation period. The transmitted intensity curves from both pillars show qualitatively similar behavior to that observed in the previous case, but it can be seen how the signal from the tall pillar, still approaching the upper detection limit, stays in saturation for a narrower time window (Figure 5.28).
Moreover, it needs $\sim 1\ s$ more than the previous case to enter the saturation window, amounting to $\sim 16\ s$ from the start of the stimulation

The short pillar continues to respond within the linear regime across the entire stimulation period, confirming the reproducibility of its dynamic behavior even under slightly attenuated illumination.

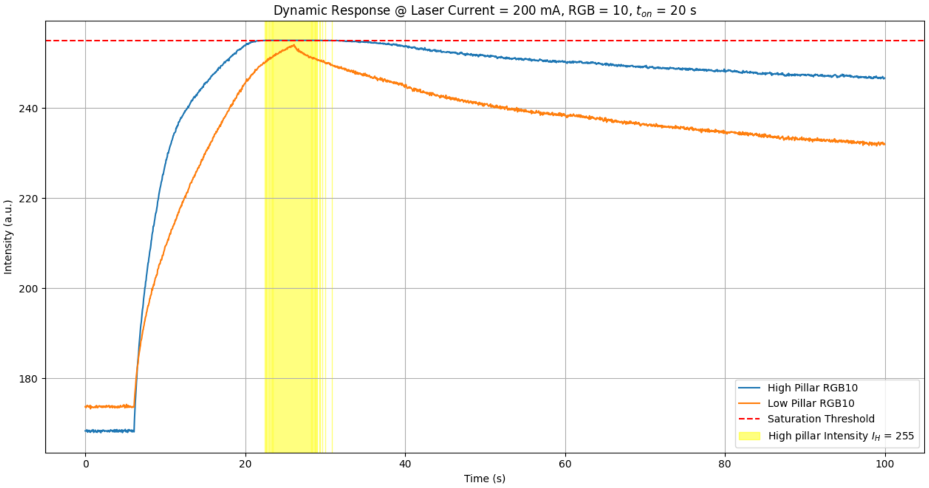

Figure 5.28: High-power regime dynamic response for RGB = 10

Low-power Regime

To investigate the limits of detectability and reliability in the low-power regime, a series of measurements were performed using the lowest laser driving current that could still produce a measurable signal $(67\ mA)$.

To modulate the delivered power more finely, four different RGB values were applied to

the projected stimulus: `RGB` = 60, 70, 75, and 80, that correspond to increasingly attenuated stimuli.
In all four experiments, a common acquisition protocol was used: $20\ s$ of baseline acquisition (no stimulation), followed by $5\ s$ of stimulation and $30\ s$ of relaxation.

The initial $20\ \mathrm{s}$ of baseline data were used to estimate the noise level of the system. The standard deviation σ of the signal was computed independently for each of the two pillar ROIs. From each standard deviation, a corresponding noise threshold was calculated using the 3-sigma criterion (Equation 5.1).
Then in order to adopt a conservative and uniform criterion for signal detectability across all plots and analyses, the effective noise threshold was then defined as:

$$I_{\text{noise}} = \max(I_{\text{noise,high}}, I_{\text{noise,low}}) \tag{5.4}$$

This threshold was used to assess whether the recorded signal at any time point could be considered significantly different from background fluctuations.

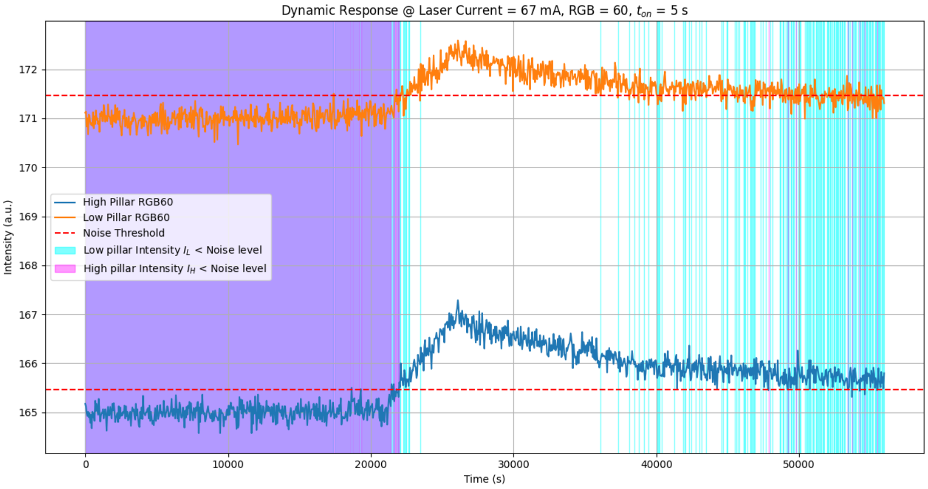

Figure 5.29: Low-power regime dynamic response for RGB = 60

The results for each RGB condition are shown in Figure 5.29, Figure 5.30, Figure 5.31, and Figure 5.32.
As expected in this low-power regime, the signals for both pillars are highly affected by noise and tend to oscillate close to the noise threshold. Occasionally, signal fluctuations drive the measured intensity below the noise level, making it difficult to define clear and consistent time windows where the signal is reliably above background.

Unlike the high-power regime, in this regime it is not possible to identify sharp detection

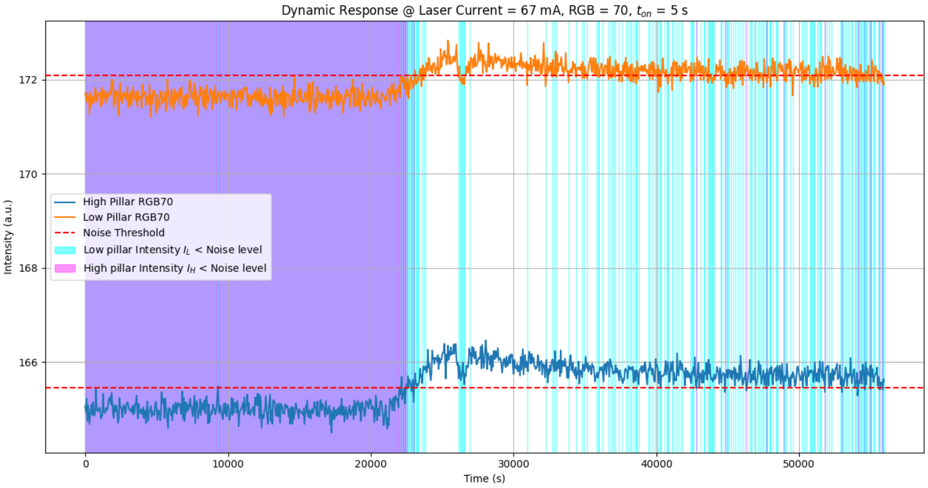

Figure 5.30: Low-power regime dynamic response for RGB = 70

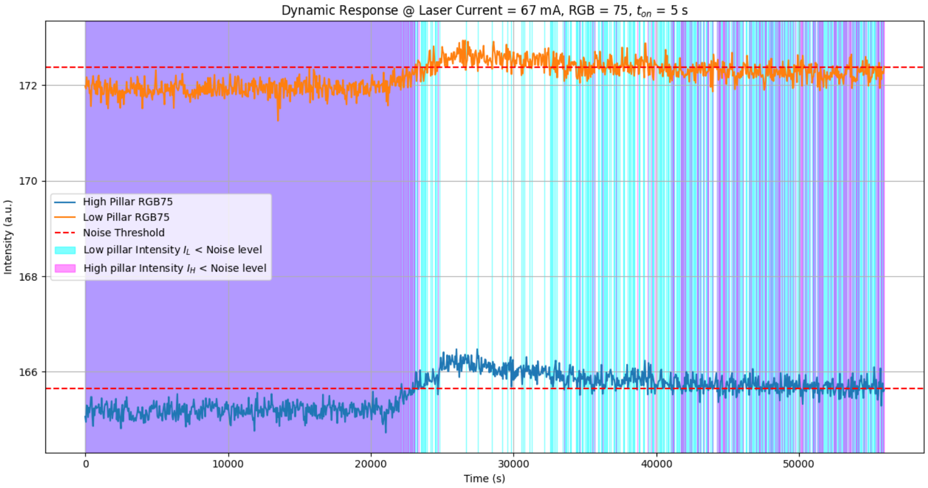

Figure 5.31: Low-power regime dynamic response for RGB = 75

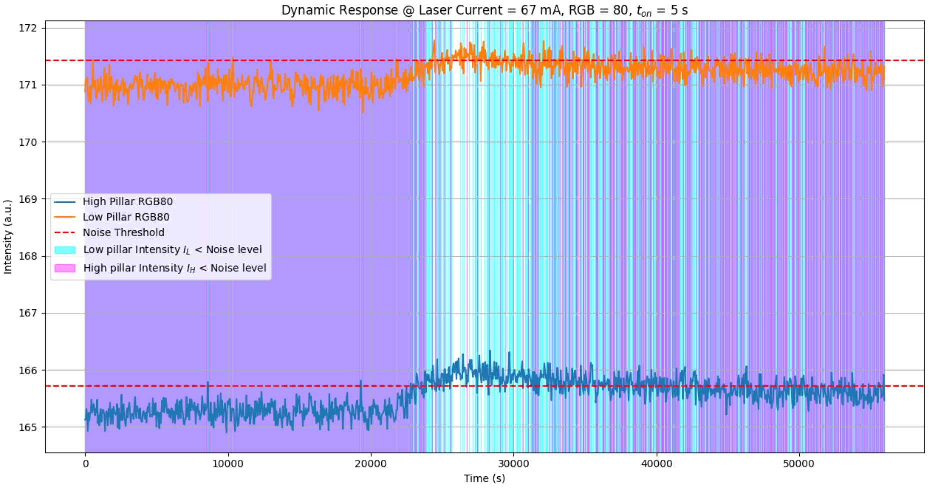

Figure 5.32: Low-power regime dynamic response for RGB = 80

windows.

However, qualitative differences in the behavior of the two pillar types are still observable. In particular, when comparing the normalized signals (after offset subtraction), shown in Figure 5.33, the maximum intensity amplitude achieved by the tall pillar exceeds that of the short pillar by at least 0.25 a.u. across all four stimulation conditions.

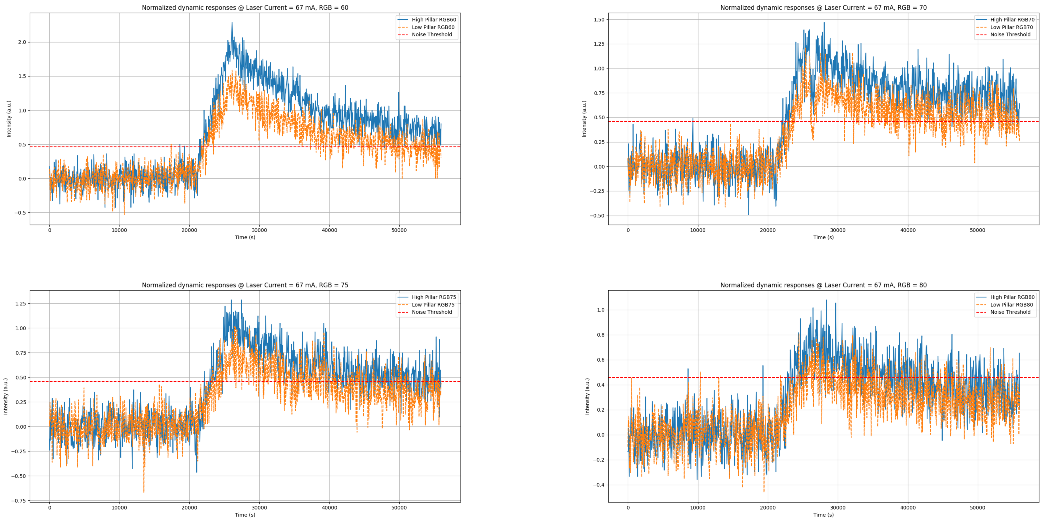

Figure 5.33: Normalized dynamic responses of the two pillar signals with different RGBs

This difference is sufficient to shift the detectability threshold in favor of the tall pillar. As the RGB value increases (i.e., as the stimulation power decreases), the signal from the tall pillar remains discernible for a longer portion of the stimulation and relaxation sequence, while the signal from the short pillar quickly becomes dominated by noise.

These observations are illustrated in Figure 5.29, Figure 5.30, Figure 5.31 and Figure 5.32, where shaded regions indicate the time intervals during which the signal remains below the noise threshold. Cyan bands correspond to the short pillar, and magenta bands to the tall pillar.
In all four cases, the onset of cyan regions precedes that of the magenta regions, confirming that the signal from the short pillar becomes unreliable sooner as the stimulation becomes weaker.

This behavior supports the conclusion that, under limited optical power, the taller structures are more robust for reliable signal detection.

The complementary behavior of the two pillar types under different stimulation regimes can be used also to enhance signal discrimination in applications such as image detection under varying illumination conditions.
The dual response of high and low pillars embedded in a localized sample region can be exploited to discriminate between different input levels (e.g. grayscale values) under both high and low intensity illumination.

To formally assess the ability to distinguish between two stimuli, the following condition was used:

$$\begin{cases} I_{\mathrm{X,RGBx}} - I_{\mathrm{X,RGBy}} > I_{\mathrm{noise}} \\ I_{\mathrm{X,RGBx}} > I_{\mathrm{X,RGBy}} \\ I_{\mathrm{noise}} < I_{\mathrm{X,RGBx}} < 255 \\ I_{\mathrm{noise}} < I_{\mathrm{X,RGBy}} < 255 \end{cases} \tag{5.5}$$

where $I_{\mathrm{X,RGBx}}$ and $I_{\mathrm{X,RGBy}}$ are the intensity values from the same type of pillar (either tall, $X = H$, or short, $X = L$), under two different RGB stimulation levels.
The inequality ensures that both signals are significantly different from one another, accounting for the noise threshold and the saturation.

As an illustrative example, if two projected patterns, stimulated with $RGB = 0$ and $RGB = 10$, are projected onto the structured sample (laser current $= 200$ mA) (Figure 5.36b), the signals from high pillars (Figure 5.34) show a window where the two intensities become indistinguishable.
In contrast, the signals from low pillars (Figure 5.35) remain distinguishable throughout most of the same temporal window, with the exception of a central point where their values briefly converge.
The contribution of both pillar types to the discrimination task is visualized in Figure 5.36a, confirming the benefit of using complementary structural responses.

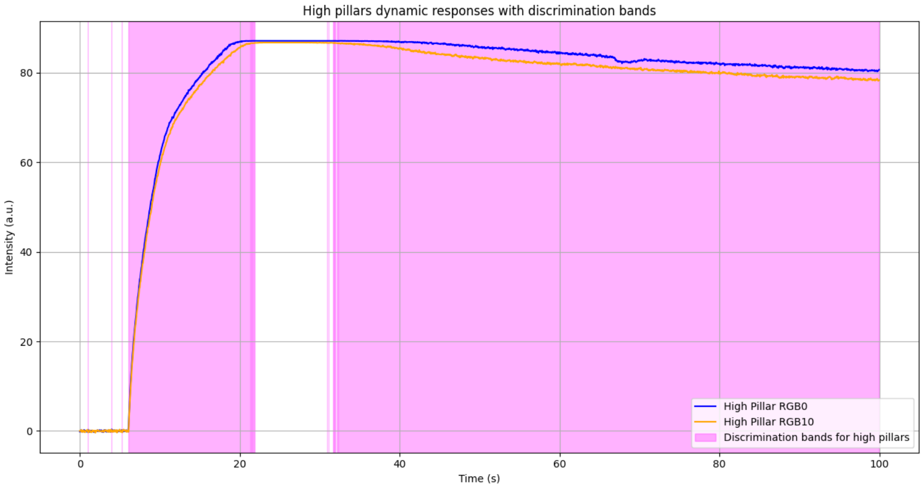

Figure 5.34: High-power regime high pillar's dynamic responses comparison at $RGB = 0$ and $RGB = 10$

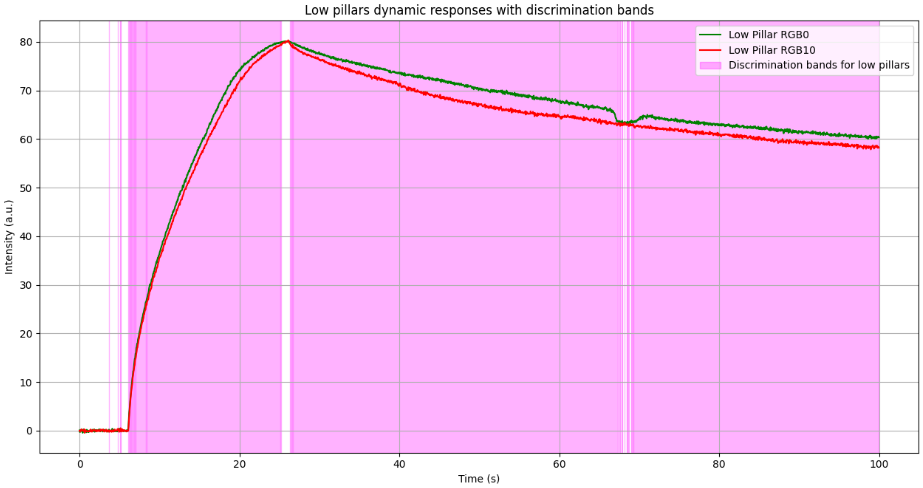

Figure 5.35: High-power regime low pillar's dynamic responses comparison at $RGB = 0$ and $RGB = 10$

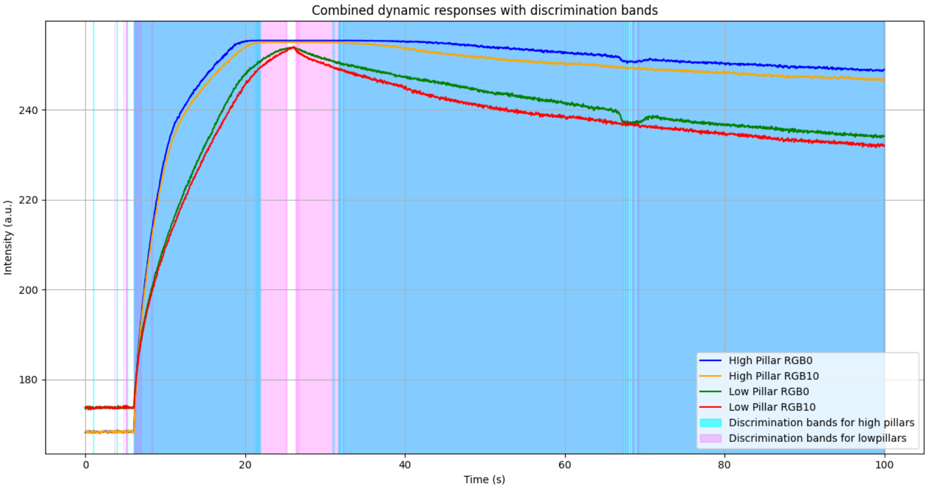

(a) High-power regime combined dynamic responses

(b) Symbolic illustration of the two illumination used for signal discrimination in high-power regime

Figure 5.36: High-power regime signal discrimination

A similar approach was applied in the low-power regime. Stimuli with $RGB = 60$ and $RGB = 75$ were compared (Figure 5.37 and Figure 5.38), and the resulting signals analyzed with the same discrimination criterion.

In this case, the short pillars yielded distinguishable signals for a shorter duration compared to the tall ones.

As shown in Figure 5.39a, beyond a certain time point the signal from the short pillar falls below the noise level or converges with the other curve, making discrimination no longer feasible. The tall pillar, instead, continues to provide usable discrimination.

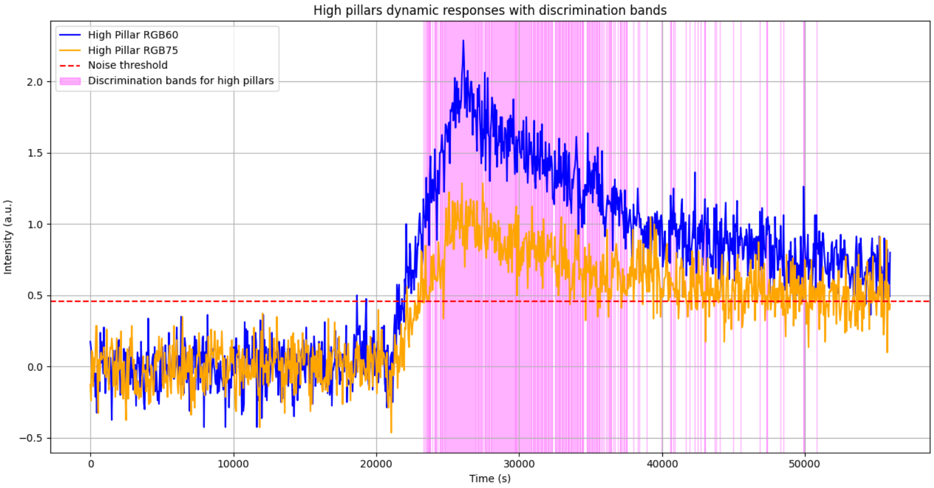

Figure 5.37: Low-power regime high pillar's dynamic responses comparison at $RGB = 60$ and $RGB = 75$

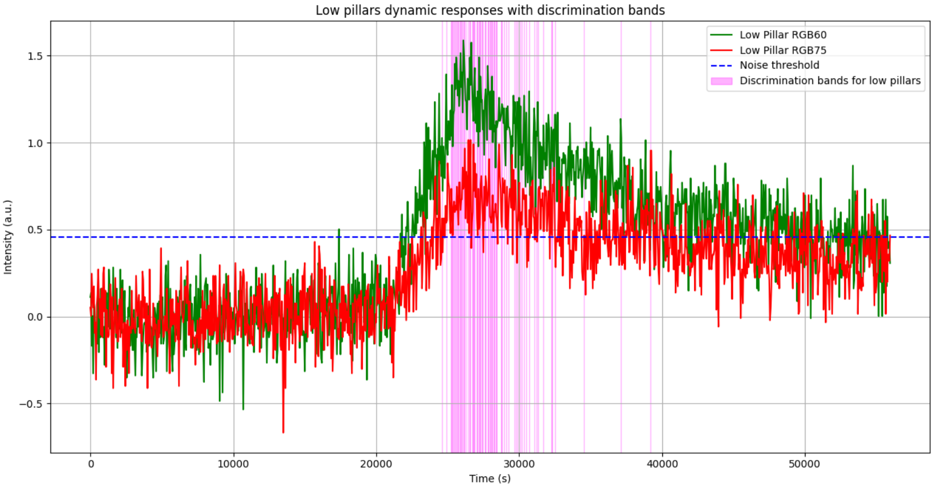

Figure 5.38: Low-power regime low pillar's dynamic responses comparison at $RGB = 60$ and $RGB = 75$

These results demonstrate that a PAZO-based surface microstructured with units of differ-

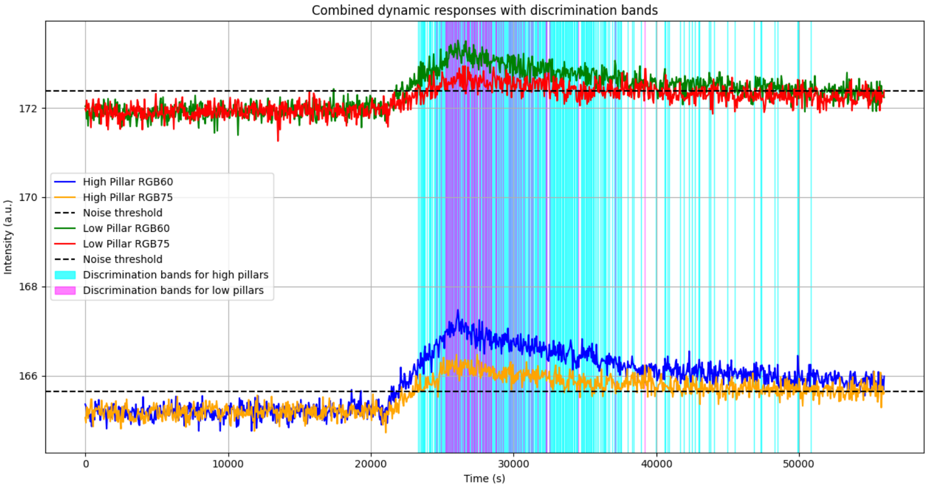

(a) Low-power regime combined dynamic responses

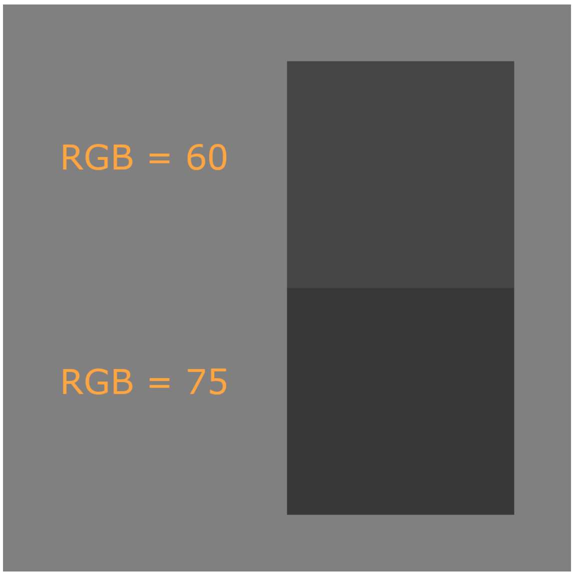

(b) Symbolic illustration of the two illumination used for signal discrimination in low-power regime

Figure 5.39: Low-power regime signal discrimination

ent thicknesses can be used to expand the operational dynamic range of the material. By extracting information from the thickness unity that delivers the most reliable signal under the given stimulation context, one can adaptively optimize performance. Moreover, this principle allows for discrimination of low-contrast inputs, especially under challenging illumination conditions.

6 | Conclusions and Future Perspectives

This work explored the potential of the azobenzene-based material PAZO to perform bio-inspired optical functions, aiming to emulate aspects of human visual processing directly at the material level. Two distinct functionalities were investigated: the emulation of adaptive vision through microstructuring and color recognition via relaxation dynamics.

The first objective addressed the challenge of extending the dynamic range of light sensitivity, taking inspiration from the dual photoreceptor system of the human retina.
By fabricating microstructured samples composed of repeating pixel units with two pillars of different heights, corresponding to distinct film thicknesses, it was possible to embed different sensitivities into spatially separated regions.
Experimental results confirmed the hypothesized behavior: thicker pillars, due to their increased absorption, generated a stronger response at low light levels, mimicking the behavior of rod cells, while thinner pillars remained measurable at higher intensities, avoiding saturation and thus acting analogously to cone cells.
This dual response profile effectively emulates the scotopic and photopic regimes of vision, offering a passive strategy to extend the operational range of light-sensitive systems through geometrical design alone.
Beyond validating the principle, the microstructured architecture was tested on a benchmark task: the classification of static images with low contrast in optical power. The coexistence of multiple thicknesses enabled effective signal separation in extreme illumination regimes, even under minimal stimulation differences.
The signal separation in the pillars' responses may also offer advantages in dynamic scenarios, where sustaining signal discriminability throughout the recording window is crucial, such as in motion tracking.

The second part of the research focused on determining whether the relaxation dynamics of birefringence in PAZO carry a spectral signature that depends on the wavelength of the stimulating light.

Using two calibrated laser sources emitting at $405\ nm$ and $520\ nm$, the material was stimulated across a controlled grid of powers and durations. The resulting relaxation curves were modeled using a bi-exponential function, from which two characteristic decay times were extracted.
While the fast component showed little spectral dependency, the slower relaxation time constant, τ_d, revealed a robust difference between the two colors under specific conditions. In particular, it was found that for exposure times longer than $1\ s$ and power densities $p \geq 54.5\ nW/\mu m^2$, τ_d for violet stimulation consistently exceeded the maximum value recorded for green. This spectral separation remained stable across the parameter space, indicating that τ_d can serve as a reliable marker to distinguish the wavelength of the stimulus.
The existence of such a spectral memory effect in the slow relaxation regime suggests the feasibility of performing color recognition using the material's intrinsic dynamics alone.

Together, these two functionalities demonstrate how PAZO can be engineered to perform complex and sensory tasks such as light adaptation and spectral discrimination without requiring electronic control, computation, or post-processing.
The ability to encode intensity-dependent and wavelength-dependent behavior directly into the structure and dynamics of the material positions PAZO as a promising candidate for in-matter optical sensing and neuromorphic computing.

In the future, we foresee the following developments, including:

- The extension of the current study to a broader spectral range for multi-wavelength discrimination
- A more detailed investigation of the molecular relaxation dynamics under different illumination wavelengths, to better understand the spectrally dependent mechanisms at a molecular level
- A systematic study on how film thickness influences the wavelength-specific response, enabling further control over wavelength-selective behavior through structural design.
- The study and integration of alternative azopolymer formulations with different absorption spectra, to extend the material's functional range and enable tunability across a broader set of wavelengths;
- The optimization of microstructural design by tailoring pillar heights, in order to identify the most effective thickness pairs that maximize the usable dynamic range of the material response.

Bibliography

[1] Dennis V Christensen, Regina Dittmann, Bernabe Linares-Barranco, Abu Sebastian, Manuel Le Gallo, Andrea Redaelli, Stefan Slesazeck, Thomas Mikolajick, Sabina Spiga, Stephan Menzel, Ilia Valov, Gianluca Milano, Carlo Ricciardi, Shi-Jun Liang, Feng Miao, Mario Lanza, Tyler J Quill, Scott T Keene, Alberto Salleo, Julie Grollier, Danijela Marković, Alice Mizrahi, Peng Yao, J Joshua Yang, Giacomo Indiveri, John Paul Strachan, Suman Datta, Elisa Vianello, Alexandre Valentian, Johannes Feldmann, Xuan Li, Wolfram H P Pernice, Harish Bhaskaran, Steve Furber, Emre Neftci, Franz Scherr, Wolfgang Maass, Srikanth Ramaswamy, Jonathan Tapson, Priyadarshini Panda, Youngeun Kim, Gouhei Tanaka, Simon Thorpe, Chiara Bartolozzi, Thomas A Cleland, Christoph Posch, ShihChii Liu, Gabriella Panuccio, Mufti Mahmud, Arnab Neelim Mazumder, Morteza Hosseini, Tinoosh Mohsenin, Elisa Donati, Silvia Tolu, Roberto Galeazzi, Martin Ejsing Christensen, Sune Holm, Daniele Ielmini, and N Pryds. 2022 roadmap on neuromorphic computing and engineering. *Neuromorphic Computing and Engineering*, **2**: 022501, 2022. DOI: `10.1088/2634-4386/ac4a83` (see pp. 1, 3)

[2] C. Kaspar, B. J. Ravoo, W. G. van der Wiel, S. V. Wegner, and W. H. P. Pernice. The rise of intelligent matter. *Nature*, **594**: 345–355, 2021. DOI: `10.1038/s41586-021-03453-y` (see pp. 1, 2)

[3] Bhavin J. Shastri, Alexander N. Tait, T. Ferreira de Lima, Wolfram H. P. Pernice, Harish Bhaskaran, C. D. Wright, and Paul R. Prucnal. Photonics for artificial intelligence and neuromorphic computing. *Nature Photonics*, **15**: 102–114, 2021. DOI: `10.1038/s41566-020-00754-y` (see p. 3)

[4] Xiaozhang Chen, Yuan Xue, Yibo Sun, Jiabin Shen, Sannian Song, Min Zhu, Zhitang Song, Zengguang Cheng, and Peng Zhou. Neuromorphic Photonic Memory Devices Using Ultrafast, Non-Volatile Phase-Change Materials. *Advanced Materials*, **35**: 2022. DOI: `10.1002/adma.202203909` (see p. 3)

[5] M. Wuttig, H. Bhaskaran, and T. Taubner. Phase-change materials for non-volatile photonic applications. *Nature Photonics*, **11**: 465–476, 2017. DOI: `10.1038/nphoton.2017.126` (see p. 3)

[6] Rui Chen, Zhuoran Fang, Forrest Miller, Hannah Rarick, Johannes E. Fröch, and Arka Majumdar. Opportunities and Challenges for Large-Scale Phase-Change Ma-

terial Integrated Electro-Photonics. *ACS Photonics*, **9**: 3181–3195, 2022. DOI: `10.1021/acsphotonics.2c00976` (see p. 3)

[7] Seunghwan Seo, Seo-Hyeon Jo, Sungho Kim, Jaewoo Shim, Seyong Oh, Jeong-Hoon Kim, Keun Heo, Jae-Woong Choi, Changhwan Choi, Saeroonter Oh, Duygu Kuzum, H.-S. Philip Wong, and Jin-Hong Park. Artificial optic-neural synapse for colored and color-mixed pattern recognition. *Nature Communications*, **9**: 2018. DOI: `10.1038/s41467-018-07572-5` (see p. 4)

[8] Hang Xu, Yue Xue, Zhenqi Liu, Qing Tang, Tianyi Wang, Xichan Gao, Yaping Qi, Yong P. Chen, Chunlan Ma, and Yucheng Jiang. Van der Waals Heterostructures for Photoelectric, Memory, and Neural Network Applications. *Small Science*, **4**: 2024. DOI: `10.1002/smsc.202300213` (see p. 4)

[9] Lian Nedelchev, Dimana Nazarova, Georgi Mateev, and Nataliya Berberova. “Birefringence induced in azopolymer (PAZO) films with different thickness” in: *18th International School on Quantum Electronics: Laser Physics and Applications*. ed. by Tanja Dreischuh, Sanka Gateva, and Alexandros Serafetinides vol. 9447 SPIE, Jan. 2015. 94471I DOI: `10.1117/12.2176158` (see pp. 5, 54)

[10] Arri Priimagi and Andriy Shevchenko. Azopolymer-based micro- and nanopatterning for photonic applications. *Journal of Polymer Science Part B: Polymer Physics*, **52**: 163–182, 2013. DOI: `10.1002/polb.23390` (see p. 6)

[11] Carla Madruga, Paulo Alliprandini Filho, Marta M. Andrade, Manuel Gonçalves, Maria Raposo, and Paulo A. Ribeiro. Birefringence dynamics of poly1-[4-(3-carboxy-4-hydroxyphenylazo)benzenesulfonamido]-1, 2-ethanediyl, sodium salt cast films. *Thin Solid Films*, **519**: 8191–8196, 2011. DOI: `10.1016/j.tsf.2011.06.102` (see pp. 5, 6, 45)

[12] Webvision, University of Utah *Rods and cones of the primate retina* `https://commons.wikimedia.org/wiki/File:Rrods_and_cones_of_the_primate_retina.jpg` Licensed under CC BY 2.5 2004 (see p. 8)

[13] Marc Madou and Chunlei Wang. In: *Photolithography*. Bharat Bhushan, ed. 2051–2060. Dordrecht: Springer Netherlands, 2012. DOI: `10.1007/978-90-481-9751-4_342` (see p. 10)

[14] Ralph R. Dammel. *Diazonaphthoquinone-based Resists*. SPIE, Feb. 1993. DOI: `10.1117/3.2265072` (see p. 12)

[15] Wayne M. Moreau. In: *Negative Photoresists*. 157–210. Boston, MA: Springer US, 1988. DOI: `10.1007/978-1-4613-0885-0_4` (see p. 12)

[16] A. Ostendorf and Karsten Koenig. In: *Tutorial laser in material nanoprocessing*. xxiii–xl. May 2015. DOI: `10.1515/9783110354324-004` (see p. 13)

[17] P.Gabella C.Weber N.Berglund. Mask Cost and Profitability in Photomask Manufacturing: An Empirical Analysis. *Semiconductor Manufacturing, IEEE Transactions on*, **19**: 465 –474, 2006. DOI: `10.1109/TSM.2006.883577` (see p. 13)

[18] Heidelberg Instruments *Fact Sheet - µMLA* Accessed: 2025-03-25 2024 (see p. 14)

[19] Svetlana N. Khonina, Nikolay L. Kazanskiy, and Muhammad A. Butt. Grayscale Lithography and a Brief Introduction to Other Widely Used Lithographic Methods: A State-of-the-Art Review. *Micromachines*, **15**: 2024. DOI: `10.3390/mi15111321` (see p. 14)

[20] Sergio Aristizabal, Giuseppe Cirino, Arlindo Montagnoli, Aparecido Sobrinho, Jose Rubert, Michel Hospital, and Ronaldo Mansano. Microlens array fabricated by a low-cost grayscale lithography maskless system. *Optical Engineering*, **52**: 125101, 2013. DOI: `10.1117/1.OE.52.12.125101` (see p. 15)

[21] Mohamed Adel, Ahmed Allam, Ashraf Sayour, Hani Ragai, Shinjiro Umezu, and Ahmed Fath El Bab. Fabrication of Spiral Low-Cost Microchannel with Trapezoidal Cross Section for Cell Separation Using a Grayscale Approach. *Micromachines*, **14**: 1370, 2023. DOI: `10.3390/mi14071340` (see p. 15)

[22] Angelos Bouchouri, Muhammad Nadeem Akram, Per Alfred Øhlckers, and Xuyuan Chen. Optimization of Grayscale Lithography for the Fabrication of Flat Diffractive Infrared Lenses on Silicon Wafers. *Micromachines*, **15**: 2024. DOI: `10.3390/mi15070866` (see p. 15)

[23] Yong Zhou, Kun Wang, Junkun Mao, Yifei Ma, Mei Wang, Suotang Jia, Xuyuan Chen, and Zhaomin Tong *Laser speckle grayscale lithography: a new tool for fabricating highly sensitive flexible capacitive pressure sensors* 2024 DOI: `10.37188/lam.2024.016` (see p. 15)

[24] Anya Grushina. Direct-write grayscale lithography. *Advanced Optical Technologies*, **8**: 163–169, 2019. DOI: `doi:10.1515/aot-2019-0024` (see p. 15)

[25] Younan Xia and George M. Whitesides. Soft Lithography. *Angewandte Chemie International Edition*, **37**: 550–575, 1998. DOI: `10.1002/(sici)1521-3773(19980316)37:5<550::aid-anie550>3.0.co;2-g` (see p. 15)

[26] Douglas B. Weibel, Willow R. DiLuzio, and George M. Whitesides. Microfabrication meets microbiology. *Nature Reviews Microbiology*, **5**: 209–218, 2007. DOI: `10.1038/nrmicro1616` (see p. 16)

[27] Aline Cerf and Christophe Vieu. Transfer printing of sub-100nm nanoparticles by soft lithography with solvent mediation. *Colloids and Surfaces A: Physicochemical and Engineering Aspects*, **342**: 136–140, 2009. DOI: `10.1016/j.colsurfa.2009.04.019` (see p. 15)

[28] Ashis Kumar Sen, Abhishek Raj, Utsab Banerjee, and Sk Rameez Iqbal. In: *Soft Lithography, Molding, and Micromachining Techniques for Polymer Micro Devices*. 13–54. Springer New York, 2018. DOI: `10.1007/978-1-4939-8964-5_2` (see pp. 17, 18)

[29] Byron D. Gates. Nanofabrication with molds amp; stamps. *Materials Today*, **8**: 44–49, 2005. DOI: `10.1016/s1369-7021(05)00701-7` (see p. 17)

[30] Enoch King, Younan Xia, Xiao-Mei Zhao, and George M. Whitesides. Solvent-assisted microcontact molding: A convenient method for fabricating three-dimensional struc-

tures on surfaces of polymers. *Advanced Materials*, **9**: 651–654, 1997. DOI: `10.1002/adma.19970090814` (see p. 19)

[31] Y. S. Kim, K. Y. Suh, and Hong H. Lee. Fabrication of three-dimensional microstructures by soft molding. *Applied Physics Letters*, **79**: 2285–2287, 2001. DOI: `10.1063/1.1407859` (see pp. 19, 20)

[32] Xufei Hu and Naixing Feng. Multicomponent Induction Logging Responses in Layered Uniaxial and Biaxial Anisotropic Media. *Pure and Applied Geophysics*, **179**: 2022. DOI: `10.1007/s00024-022-03174-x` (see p. 23)

[33] Andrea Weidlich and Alexander Wilkie. Realistic rendering of birefringency in uniaxial crystals. *ACM Trans. Graph.*, **27**: 2008. DOI: `10.1145/1330511.1330517` (see p. 24)

[34] PhD Van Kan Peter L.E. *How information is transmitted between neurons | Synaptic transmission at chemical synapses* en-US (see p. 26)

[35] Woong Huh, Donghun Lee, and Chul-Ho Lee. Memristors based on 2D materials as an artificial synapse for neuromorphic electronics. *Advanced materials*, **32**: 2002092, 2020. (see p. 26)

[36] Jun-Woo Jang, Sangsu Park, Yoon-Ha Jeong, and Hyunsang Hwang. “ReRAM-based synaptic device for neuromorphic computing” in: *2014 IEEE International Symposium on Circuits and Systems (ISCAS)*. IEEE 2014. 1054–1057 (see p. 26)

[37] Le Zhao, Hong Fang, Jie Wang, Fang Nie, Rongqi Li, Yuling Wang, and Limei Zheng. Ferroelectric artificial synapses for high-performance neuromorphic computing: Status, prospects, and challenges. *Applied Physics Letters*, **124**: 2024. DOI: `10.1063/5.0165029` (see p. 26)

[38] Robert S. Zucker and Wade G. Regehr. Short-Term Synaptic Plasticity. *Annual Review of Physiology*, **64**: 355–405, 2002. DOI: `10.1146/annurev.physiol.64.092501.114547` (see p. 27)

[39] Chao Li, Xumeng Zhang, Pei Chen, Keji Zhou, Jie Yu, Guangjian Wu, Du Xiang, Hao Jiang, Ming Wang, and Qi Liu. Short-term synaptic plasticity in emerging devices for neuromorphic computing. *iScience*, **26**: 106315, 2023. DOI: `10.1016/j.isci.2023.106315` (see p. 27)

[40] Eden Anderson and Matthew Hearing. In: *Neural Circuit Plasticity in Addiction*. 35–60. Elsevier, 2019. DOI: `10.1016/b978-0-12-812202-0.00004-x` (see p. 27)

[41] Graham L. Collingridge, Stephane Peineau, John G. Howland, and Yu Tian Wang. Long-term depression in the CNS. *Nature Reviews Neuroscience*, **11**: 459–473, 2010. DOI: `10.1038/nrn2867` (see p. 28)

[42] Ke Chen, Hang Hu, Inho Song, Habtom B. Gobeze, Won-June Lee, Ashkan Abtahi, Kirk S. Schanze, and Jianguo Mei. Organic optoelectronic synapse based on photon-modulated electrochemical doping. *Nature Photonics*, **17**: 629–637, 2023. DOI: `10.1038/s41566-023-01232-x` (see p. 28)

[43] Geonyeop Lee, Ji-Hwan Baek, Fan Ren, Stephen J. Pearton, Gwan-Hyoung Lee, and Jihyun Kim. Artificial Neuron and Synapse Devices Based on 2D Materials. *Small*, **17**: 2021. DOI: `10.1002/smll.202100640` (see p. 28)

[44] Dale Purves. *Neuroscience*. en Sunderland, MA: Sinauer Associates, 2001. (see p. 29)

[45] Valentin Dragoi *Visual Processing: Eye and Retina (Section 2, Chapter 14) Neuroscience Online: An electronic textbook for the neurosciences | Department of Neurobiology and Anatomy - The University of Texas Medical School at Houston* URL: `https://nba.uth.tmc.edu/neuroscience/m/s2/chapter14.html` (see p. 30)

[46] Ufo Themes *The visual system* en-US May 2019 (see p. 30)

[47] Brian A Wandell. *Foundations of vision*. Sinauer Associates, 1995. (see p. 30)

[48] Norianne T. Ingram, Alapakkam P. Sampath, and Gordon L. Fain. Why are rods more sensitive than cones? *The Journal of Physiology*, **594**: 5415–5426, 2016. DOI: `10.1113/jp272556` (see p. 31)

[49] Lian Nedelchev, Deyan Ivanov, Blaga Blagoeva, and Dimana Nazarova. Optical anisotropy induced at five different wavelengths in azopolymer thin films: Kinetics and spectral dependence. *Journal of Photochemistry and Photobiology A: Chemistry*, **376**: 1–6, 2019. DOI: `10.1016/j.jphotochem.2019.02.009` (see p. 54)

[50] Jan Erjawetz, Dominique Collé, Gerda Ekindorf, Peter Heyl, Daniel Ritter, Aditya Reddy, and Helmut Schift. Bend the curve – Shape optimization in laser grayscale direct write lithography using a single figure of merit. *Micro and Nano Engineering*, **15**: 100137, 2022. DOI: `10.1016/j.mne.2022.100137` (see p. 59)